



**Top-Quark Mass Determinations  
in the  $e\mu$  Dilepton Channel**

and

**Top-Quark Mass Effects in  
Higgs Boson Pair Production**

**Ludovic M. Scyboz**





# Top-Quark Mass Determinations in the $e\mu$ Dilepton Channel

and

## Top-Quark Mass Effects in Higgs Boson Pair Production

Ludovic M. Scyboz

Vollständiger Abdruck der von der Fakultät für Physik der Technischen Universität München zur Erlangung des akademischen Grades eines

Doktors der Naturwissenschaften (Dr. rer. nat.)

genehmigten Dissertation.

**Vorsitzender:**

Prof. Dr. Andreas Weiler

**Prüfende der Dissertation:**

1. Dr. Stefan Kluth
2. Prof. Dr. Wolfgang Hollik,  
Technische Universität München

Die Dissertation wurde am 18.05.2019 bei der Technischen Universität München eingereicht und durch die Fakultät für Physik angenommen.



## <sup>5</sup> Abstract

<sup>6</sup> In the Standard Model (SM) of Particle Physics, the top-quark plays the role of a centre-  
<sup>7</sup> piece. It interacts across all sectors and with all gauge fields, and has been successfully  
<sup>8</sup> used as a portal to precision measurements of the SM parameters. Top-quarks are  
<sup>9</sup> also indirectly related to other SM sectors, for example to Higgs boson production pro-  
<sup>10</sup> cesses which are induced predominantly by top-quark loops at the Large Hadron Collider  
<sup>11</sup> (LHC). During Runs I and II of the LHC, a large number of top-quark pair ( $t\bar{t}$ ) and  
<sup>12</sup> single-top events were recorded. They allowed to reduce the experimental uncertainty  
<sup>13</sup> on top-quark properties, like the top-quark mass, but also spin correlations and  $W$  bo-  
<sup>14</sup> son polarization in  $t\bar{t}$  events, the  $Wtb$  coupling, or flavour-changing neutral currents. In  
<sup>15</sup> the case of the top-quark mass, the experimental uncertainties of the latest ATLAS and  
<sup>16</sup> CMS combination are now competing with theoretical uncertainties: approximations  
<sup>17</sup> that were previously thought to be appropriate must be reevaluated.

<sup>18</sup> The narrow-width approximation (NWA) for top-quark pair production in particular,  
<sup>19</sup> which assumes the production of an on-shell top- and anti-top quark, is used in Monte-  
<sup>20</sup> Carlo (MC) predictions for most experimental analyses. Since the actual final-state  
<sup>21</sup> is composed of the top-quark pair decay products, though, an accurate description of  
<sup>22</sup> the signal should consider  $W^+W^-b\bar{b}$  final-states instead, which generate diagrams that  
<sup>23</sup> do not necessarily factorize in the top-quark decay legs, nor even contain a top-quark  
<sup>24</sup> pair to begin with. These diagrams are called non-factorizing, respectively non-doubly  
<sup>25</sup> resonant. In cases where measurements rely on phase-space regions sensitive to these  
<sup>26</sup> contributions, the extracted top-quark mass will be biased.

<sup>27</sup> In this work, we take the example of the 8 TeV ATLAS top-quark mass analysis in the  
<sup>28</sup>  $e\mu$  dilepton channel, which bases on simulated templates to extract the MC top-quark  
<sup>29</sup> mass by an unbinned likelihood fit. In a similar setup, we compare the extracted top-  
<sup>30</sup> quark masses at parton-level for different theoretical descriptions of the  $t\bar{t}$  final-state at  
<sup>31</sup> next-to-leading order (NLO) in production. In this respect, MC events are produced for  
<sup>32</sup> three different descriptions of the top-quark decay in the NWA, as well as for the full  
<sup>33</sup>  $W^+W^-b\bar{b}$  process at NLO in production. The top-quark mass  $m_t^{\text{MC}}$  extracted by the  
<sup>34</sup> template fit method is compared for each of these theoretical descriptions, and important  
<sup>35</sup> biases of up to  $\Delta m_t^{\text{MC}} \sim 1$  GeV are underlined. A more realistic assessment, where these  
<sup>36</sup> predictions are folded to detector-level, is also presented.

<sup>37</sup> As mentioned, the top-quark mass also plays an important role in other sectors of the  
<sup>38</sup> SM. With the example of di-Higgs production with non-SM values of the Higgs couplings,  
<sup>39</sup> we show that the  $m_t$ -dependence of QCD NLO corrections introduces sizeable differences  
<sup>40</sup> with respect to predictions where top-quark degrees of freedom are integrated out. A  
<sup>41</sup> full-fledged MC event generator (with the possibility of varying the Higgs self-coupling  
<sup>42</sup> and the Higgs-top Yukawa coupling) is introduced.



## <sup>43</sup> Zusammenfassung

<sup>44</sup> Im Standard-Modell (SM) der Teilchenphysik spielt der Top-Quark eine zentrale Rolle.  
<sup>45</sup> Er wechselwirkt mit Teilchen aller Sektoren sowie mit allen quantentheoretischen Eich-  
<sup>46</sup> feldern, und wurde in verschiedenen Kontexten als Eingangspunkt zu Präzisionsmessungen  
<sup>47</sup> des SM verwendet. Top-Quarks sind auch eng mit anderen Sektoren des SM verbun-  
<sup>48</sup> den: Higgs-Bosonen zum Beispiel werden am Large Hadron Collider (LHC) überwiegend  
<sup>49</sup> durch Top-Quark-Schleifen erzeugt. Während Runs I und II des LHC wurde eine mas-  
<sup>50</sup> sive Anzahl an Top-Quark-Paar ( $t\bar{t}$ ) und Einzel-Top-Events ermittelt. Diese haben es  
<sup>51</sup> ermöglicht, Messungen von Top-Quark-Eigenschaften bedeutend zu verbessern, beispiel-  
<sup>52</sup> sweise die der Top-Quark-Masse. In diesem Fall sind die von ATLAS und CMS angegebe-  
<sup>53</sup> nen experimentellen Unsicherheiten zu dem Punkt gekommen, wo sie mit den aktuellen  
<sup>54</sup> theoretischen Unsicherheiten rivalisieren: das heisst insbesondere, dass früher akzep-  
<sup>55</sup> tierte Approximationen neu abgeschätzt werden müssen.

<sup>56</sup> Die sogenannte Schmal-Breite-Approximation (NWA), bei der ein Top-Quark-Paar  
<sup>57</sup> on-shell produziert wird, wird üblicherweise in den meisten Monte-Carlo (MC) Analy-  
<sup>58</sup> sen verwendet. Weil der gemessene  $t\bar{t}$ -Endzustand aber von den Top-Zerfallsprodukten  
<sup>59</sup> gebildet wird, soll eine konsistente Beschreibung des Signals eher auf dem intermediären  
<sup>60</sup>  $W^+W^-b\bar{b}$  Zustand beruhen. Letzterer beinhaltet Feynman-Diagramme, die entweder  
<sup>61</sup> nicht in zwei faktorisierten Top-Zerfall-Kanälen kollabieren, oder überhaupt keine zwei  
<sup>62</sup> Top-Propagatoren aufweisen. Diese Diagramme heissen nicht-faktorisierend, bzw. nicht-  
<sup>63</sup> doppelt-resonant. Wenn Messungen durchgeführt werden, die sensitiv auf solche Beiträge  
<sup>64</sup> sind, kann sich ein Bias in der extrahierten Top-Quark-Masse bilden.

<sup>65</sup> Wir nehmen als Beispiel die ATLAS Top-Quark-Masse Analyse im  $e\mu$ -Dileptonkanal  
<sup>66</sup> hin, welche auf simulierten Templates basiert zum Extrahieren der Top-Quark-Masse.  
<sup>67</sup> In einem naheliegenden Setup wird die extrahierte Top-Masse verglichen, wo unter-  
<sup>68</sup> schiedliche  $t\bar{t}$ -Endzustandsbeschreibungen auf next-to-leading-order (NLO) in Produk-  
<sup>69</sup> tion eingesetzt werden. Genauer werden für drei verschiedenen Beschreibungen des Top-  
<sup>70</sup> Quark-Zerfalls, sowie für die volle NLO  $W^+W^-b\bar{b}$ -Rechnung, Verteilungen erzeugt. Die  
<sup>71</sup> mithilfe der Template-Fit-Methode extrahierte Top-Quark-Masse  $m_t^{\text{MC}}$  zeigt erhebliche  
<sup>72</sup> Bias bis zu  $\Delta m_t^{\text{MC}} \sim 1 \text{ GeV}$ . Eine realistischere Studie wird eingeführt wo Particle-  
<sup>73</sup> Level-Vorhersagen auf Detector-Level gefalten werden.

<sup>74</sup> Dagegen wirken Top-Quark-Effekte auch im Higgs-Sektor. Anhand des Beispiels von  
<sup>75</sup> Higgs-Paar-Produktion ( $hh$ ) beim LHC wird gezeigt, dass die  $m_t$ -Abhängigkeit von  
<sup>76</sup>  $hh$  Produktion auf NLO QCD Unterschiede in differentiellen Verteilungen aufweisen  
<sup>77</sup> im Vergleich zu Vorhersagen, wo die Top-Quark-Freiheitsgraden ausintegriert werden.  
<sup>78</sup> Ein vollständiges MC-Package zur Erzeugung von Higgs-Paar-Events (wo die trilineare  
<sup>79</sup> Higgs-Selbstkopplung sowie die Higgs-Top-Yukawakopplung variiert werden können) wird  
<sup>80</sup> präsentiert.



# 81 Contents

82	<b>Abstract</b>	v
83	<b>Zusammenfassung</b>	vii
84	<b>Contents</b>	ix
85	<b>1 Introduction</b>	1
86	<b>I Theoretical &amp; Experimental Setup</b>	5
87	<b>2 The Standard Model</b>	7
88	2.1 Matter content and gauge interactions . . . . .	7
89	2.2 The Higgs mechanism . . . . .	10
90	2.3 Top-Higgs interactions . . . . .	13
91	2.4 Outstanding issues with the SM . . . . .	15
92	<b>3 Higher-order perturbative calculations in hadron-hadron collisions</b>	17
93	3.1 Divergences in QFT . . . . .	17
94	3.1.1 Regularization . . . . .	17
95	3.1.2 Renormalization . . . . .	20
96	3.1.3 Perturbative expansion of QCD . . . . .	20
97	3.2 Infrared divergences . . . . .	22
98	3.3 The factorization theorem . . . . .	23
99	<b>4 Monte-Carlo event generators</b>	25
100	4.1 Matrix-element providers . . . . .	27
101	4.1.1 GoSAM: MC interfacing of one-loop amplitudes . . . . .	27
102	4.1.2 Infrared divergence cancellation . . . . .	29
103	4.2 Parton-shower models . . . . .	31
104	4.2.1 Altarelli-Parisi splitting functions . . . . .	31
105	4.2.2 The Sudakov form factor . . . . .	32
106	4.2.3 Parton-shower matching . . . . .	32
107	4.3 Hadronization . . . . .	33
108	4.3.1 Lund string model . . . . .	34
109	4.3.2 Cluster model . . . . .	34

## Contents

110	<b>5 The LHC and the ATLAS detector</b>	<b>37</b>
111	5.1 The Large Hadron Collider . . . . .	37
112	5.2 The ATLAS detector . . . . .	38
113	5.2.1 The Inner Detector . . . . .	39
114	5.2.2 The Liquid Argon (LAr) Calorimeter . . . . .	41
115	5.2.3 The Tile Calorimeter (TileCal) . . . . .	42
116	5.2.4 The Muon Spectrometer . . . . .	42
117	5.2.5 Trigger & Data acquisition . . . . .	42
118	<b>II Top-Quark Mass Determinations</b>	<b>45</b>
119	<b>6 Theoretical predictions for <math>t\bar{t}</math> final-states</b>	<b>47</b>
120	6.1 The narrow-width approximation . . . . .	48
121	6.2 $W^+W^-b\bar{b}$ production: review of existing calculations . . . . .	50
122	6.3 $W^+W^-b\bar{b}$ calculation setup at NLO QCD . . . . .	51
123	6.4 Event requirements . . . . .	53
124	6.5 Total cross-section results . . . . .	54
125	<b>7 NWA versus <math>W^+W^-b\bar{b}</math>: Top-quark mass uncertainties at parton-level</b>	<b>55</b>
126	7.1 The template fit method . . . . .	55
127	7.2 Definition of the observables . . . . .	56
128	7.3 Comparison of the different theoretical descriptions . . . . .	57
129	7.4 Template fit results . . . . .	61
130	<b>8 Experimental resolution and bin migration</b>	<b>69</b>
131	8.1 Inverse problems . . . . .	69
132	8.2 Folding setup in ATLAS . . . . .	70
133	8.3 Theoretical descriptions and MC samples . . . . .	71
134	<b>9 Determination of the top-quark mass at detector-level</b>	<b>73</b>
135	9.1 The AnalysisTop setup . . . . .	73
136	9.2 Differential results at particle- and detector-level . . . . .	74
137	9.3 Statistical and systematic cross-checks . . . . .	75
138	9.4 Folded results and template parametrization . . . . .	76
139	9.5 Numerical result for top-quark mass uncertainties . . . . .	77
140	<b>III Top-Quark Mass Effects in Higgs Pair Production</b>	<b>79</b>
141	<b>10 Top-mass dependence in Higgs pair production at NLO</b>	<b>81</b>
142	10.1 Theoretical descriptions of $hh$ production . . . . .	82
143	10.1.1 Approximations in the heavy-top limit ( $m_t \rightarrow \infty$ ) . . . . .	83
144	10.1.2 Two-loop contribution in the SM . . . . .	84
145	10.2 The Electroweak Chiral Lagrangian . . . . .	84

146	10.3 Total cross-sections for BSM benchmark points . . . . .	86
147	10.4 Differential cross-sections and HTL approximations . . . . .	92
148	<b>11 Variations of the triple Higgs-coupling and parton-shower effects</b>	<b>97</b>
149	11.1 The POWHEG-BOX framework . . . . .	97
150	11.2 Interfacing two-loop contributions . . . . .	98
151	11.3 Total and differential cross-sections at fixed-order . . . . .	99
152	11.4 Parton-shower matched predictions at NLO . . . . .	101
153	<b>12 Conclusion &amp; Outlook</b>	<b>105</b>
154	<b>Bibliography</b>	<b>107</b>
155	<b>A Template fit results</b>	<b>121</b>
156	<b>B Color-flow comparisons for Sherpa</b>	<b>125</b>
157	<b>C BSM benchmark points in <math>hh</math> production</b>	<b>126</b>
158	<b>D Hardness definitions in Powheg to Pythia matching</b>	<b>129</b>



# <sup>159</sup> 1 Introduction

<sup>160</sup> The Standard Model (SM) of Particle Physics is one of the most successful physical  
<sup>161</sup> theories to date. While it still begs some unanswered questions that are outlined in  
<sup>162</sup> Chapter 2, the precision to which its predictions were tested by high-energy colliders,  
<sup>163</sup> but also in low-energy experiments, large-scale universe phenomena, neutrino and other  
<sup>164</sup> experiments is extremely convincing. In particular, the SM bases on mathematical  
<sup>165</sup> concepts that allow for a significant predictive power. Considering that physicists tend to  
<sup>166</sup> like a theory that contains the least amount of free parameters and a maximal predictive  
<sup>167</sup> power, the SM fares rather well: it contains only 19 parameters, namely the angles of the  
<sup>168</sup> Cabibbo-Kobayashi-Maskawa mixing matrix and its CP-violating phase (3+1), the gauge  
<sup>169</sup> couplings corresponding to the model's underlying symmetries (3), the lepton and quark  
<sup>170</sup> masses (9), the QCD vacuum angle (1), and the Higgs mass and vacuum expectation  
<sup>171</sup> value (2). Since most of these parameters have been measured to an excellent precision,  
<sup>172</sup> efforts have largely concentrated on the less well-measured parameters, one of these being  
<sup>173</sup> the top-quark mass.

<sup>174</sup> Because the top-quark is the heaviest known elementary particle, with a mass from  
<sup>175</sup> the world combination measured at  $m_t = 173.0 \pm 0.4$  GeV [1], physicists had to wait  
<sup>176</sup> until 1995 for its discovery by the CDF [2] and DØ [3] experiments at Fermilab, 23  
<sup>177</sup> years after it was predicted. Only then did the last missing piece of the three quark  
<sup>178</sup> generations fall into place. Nowadays, abundant production of top-quarks with the  
<sup>179</sup> Large Hadron Collider (LHC) at CERN allows for a variety of accurate measurements  
<sup>180</sup> of its properties. Of particular interest, the precise determination of its mass is a key  
<sup>181</sup> to a deeper understanding of modern quantum-field theory (QFT). Most notably, the  
<sup>182</sup> top-quark mass enters global electroweak fits which are important for consistency testing  
<sup>183</sup> of the SM; it also strongly affects corrections to the Higgs quartic coupling, thus having  
<sup>184</sup> a large impact on the stability of the SM vacuum. Finally, being the only quark with a  
<sup>185</sup> lifetime surpassing the hadronization scale, it is the only *bare* colored particle produced  
<sup>186</sup> in SM processes. In general, one has to choose an appropriate mass definition, be it a  
<sup>187</sup> QFT-consistent definition like the pole mass (on-shell renormalized) and the  $\overline{\text{MS}}$  mass  
<sup>188</sup> (renormalized after the short-distance  $\overline{\text{MS}}$  scheme), or the so-called Monte-Carlo (MC)  
<sup>189</sup> mass.

<sup>190</sup> Recently, the ATLAS and CMS experiments, using innovative approaches and analysis  
<sup>191</sup> techniques, have been able to reduce the uncertainty of the measured MC top-quark  
<sup>192</sup> mass to about  $\Delta m_t \approx 0.5$  GeV in their respective combinations [5, 6] (see Fig. 1.1  
<sup>193</sup> for measurements at LHC). Achieving a more precise determination of  $m_t$  constitutes  
<sup>194</sup> a significant challenge for both the experimental and theoretical communities. While  
<sup>195</sup> on the one hand, experimentalists have to find new ideas to drive down the mostly  
<sup>196</sup> systematics-dominated uncertainties, theorists need to improve precision calculations by

## 1 Introduction

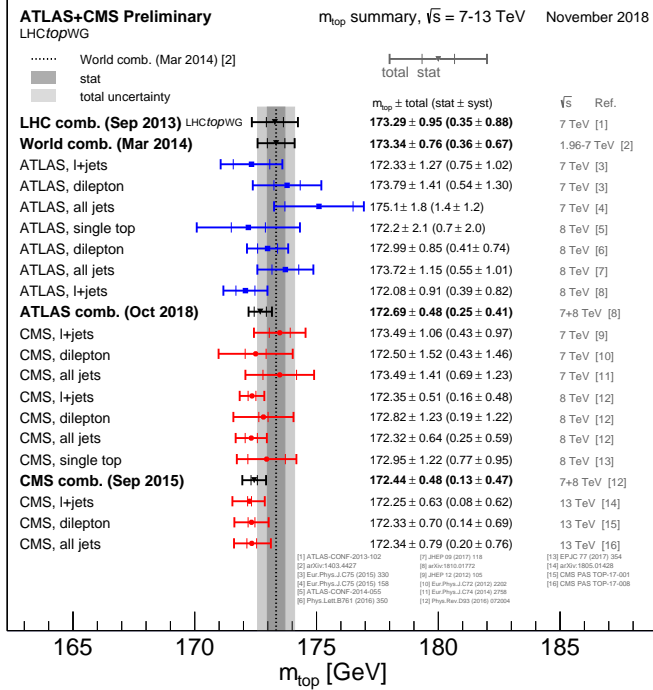


**Figure 1.1:** ATLAS and CMS combination of  $\sqrt{s} = 7, 8, 13$  TeV data for measurements of the top-quark mass  $m_t$ . Figure taken from Ref. [4].

going to higher-order predictions and beyond formerly accepted approximations. The computation of higher-order corrections for on-shell top-quark pair ( $t\bar{t}$ ) production has been a major success during the LHC era. The production of a pair of on-shell top-quarks is referred to as the narrow-width approximation (NWA). Because the corrections to NWA calculations are expected to be small, of order  $\mathcal{O}(\Gamma_t/m_t) < 1\%$  for inclusive cross-sections, most fixed-order predictions aim at computing higher-order QCD and EW corrections to top-quark pair production in this approximation.

The experimentalists, though, reconstruct the top-quark pair from their decay products, so either from the dilepton, lepton+jets or all-hadronic final-states, depending on the decay channel of the top and antitop-quarks. The fixed-order prediction of a fully-decayed  $t\bar{t}$  final-state is computationally demanding: instead of a  $2 \rightarrow 2$  process, the final-state phase space becomes that of a  $2 \rightarrow 4$  (for  $pp \rightarrow W^+W^-b\bar{b}$ ) or a  $2 \rightarrow 6$  process (including  $W$ -boson decay products). A computation of the full final-state prediction at next-to-leading order (NLO) comprises Feynman diagrams that are not present in the NWA: some do not contain double-resonant top-quarks, and others include internal lines between the top-quark decay legs, i.e. the latter do not factorize. In fact, the additional interference terms can be of importance to distributions that are sensitive to higher-order and off-shell effects, for example in phase-space regions populated first at higher-order in QCD.

216     Concerning the theoretical definition of the top-quark mass, relations between different  
217 renormalization schemes are known at 4-loop order [7]. This relation suffers from an IR  
218 so-called renormalon singularity, which is associated to an intrinsically non-perturbative  
219 ambiguity in the definition of the top-quark pole mass. This inherent uncertainty was  
220 estimated to be of the order  $\mathcal{O}(250 \text{ MeV})$  [8–11]. Moreover, analyses that rely on sim-  
221 lated distributions (like the template fit method studied in the next Chapters) measure  
222 the MC top-quark mass, not the pole mass. Although the discussion on the exact rela-  
223 tion of the MC to the pole top-quark mass is still ongoing, the difference between both  
224 values is expected to be of the order  $\mathcal{O}(300 - 500 \text{ MeV})$  [12, 13].

225     In this work, we first briefly present the foundations of the SM including the Higgs  
226 mechanism and the relation between the Higgs sector and the top-quark in Chapter 2. In  
227 Chapter 3, the basics of higher-order calculations are summarized: the appearance of UV  
228 and IR divergences in loop corrections and the way to deal with them (regularization and  
229 renormalization), the perturbative expansion for QCD at high energies from the running  
230 of the strong coupling  $\alpha_s$ , and the factorization theorem for hadron-hadron collisions are  
231 laid out in some detail. Finally, we concentrate on MC event generators in Chapter 4  
232 and explain the ingredients needed for particle-level event generation. Switching to  
233 the experimental side, the LHC and in particular the ATLAS detector are presented  
234 in Chapter 5. At that point, the different theoretical descriptions of top-quark pair  
235 production are discussed in Chapter 6. With the example of top-quark pair predictions  
236 in the  $e\mu$  dilepton channel, we show how higher-order and off-shell effects can have a  
237 sizeable impact on an experimental MC top-quark mass extraction in Chapter 7. There,  
238 four different theoretical descriptions are compared with respect to an experimentally  
239 realistic top-quark mass extraction for  $pp \rightarrow W^+(\rightarrow e^+\nu_e)W^-(\rightarrow \mu^-\bar{\nu}_\mu)b\bar{b}$ . In the  
240 NWA, we produce top-quark pairs at NLO QCD, and describe the top-decay at different  
241 accuracies: LO, respectively NLO QCD, as well as operated by a parton-shower. We  
242 compare the NWA results to a full  $W^+W^-b\bar{b}$  computation at NLO QCD. Taking into  
243 account detector reconstruction efficiencies and bin migration effects, which is the subject  
244 of Chapter 8, we then quantify the shift in the extracted top-quark mass in an exact  
245 ATLAS framework in Chapter 9, where distributions are folded up to detector-level.

246     Looking at another sector entirely, we emphasize that top-quarks also play an impor-  
247 tant role in calculations for the production of one or several Higgs bosons at the LHC.  
248 Because the top-quark is the heaviest SM particle and since the Higgs boson’s coupling  
249 to fermions is proportional to their mass, higher-order corrections to Higgs processes  
250 mainly happen through top-quark loops. For instance, single Higgs production at the  
251 LHC is dominated by gluon-fusion with a top-quark loop intermediate state (so-called  
252 loop-induced production), i.e. higher-order corrections to  $gg \rightarrow h$  start at two-loop  
253 level already. The same holds for the production of a pair of Higgs bosons: this pro-  
254 cess is of particular interest, since di-Higgs production is the main channel for probing  
255 the trilinear Higgs self-coupling. Although the Higgs couplings to heavy fermions and  
256 gauge bosons are currently nicely constrained, as shown in Fig. 1.2, the best limit set  
257 on the Higgs self-coupling’s ratio  $\kappa_\lambda$  to the SM-predicted value is given by ATLAS at  
258  $-5.0 \leq \kappa_\lambda \leq 12.1$  [16]. In general, the Higgs sector is one of the more poorly explored  
259 experimentally, and it is important to have precise (at best model-independent) theoret-

## 1 Introduction

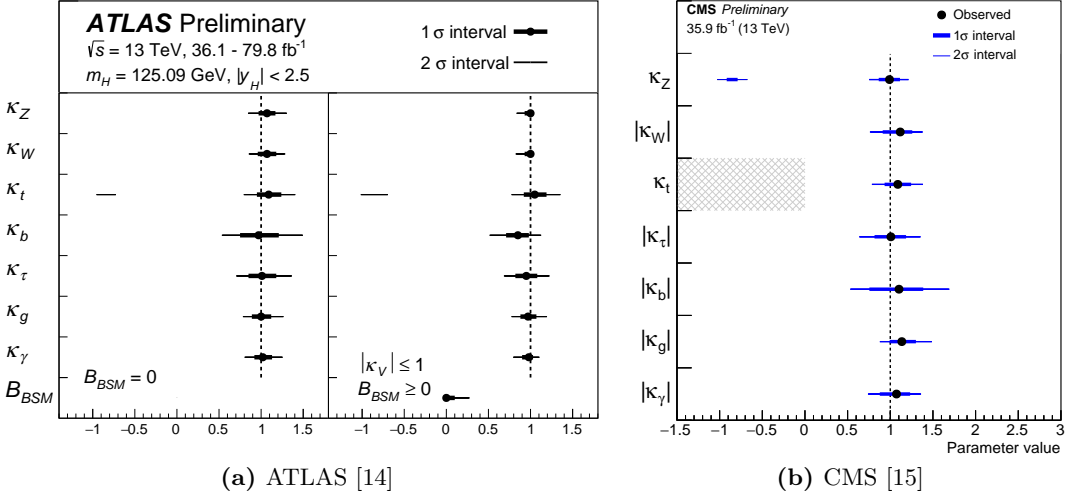


**Figure 1.2:** Fit values of the Higgs coupling modifiers with respect to the SM-predicted coupling strength (in the  $\kappa$ -framework).

ical predictions for the case where the Higgs couplings are not SM-like. We show, within a non-linear Effective Field Theory (EFT) framework allowing to vary the Higgs couplings, that the full  $m_t$ -dependence of di-Higgs production at NLO QCD has important effects, especially on differential cross-section predictions. In Chapter 10, the electroweak chiral Lagrangian (EWChL) is introduced. The results for NLO di-Higgs cross-sections and differential distributions with variations of the Higgs couplings are presented at 14 TeV for several benchmark points. Finally, the implementation of the full  $m_t$ -dependent NLO corrections for di-Higgs production into the Powheg-BOX-V2 [17–19] event generator is the subject of Chapter 11. In this package, variations of the trilinear Higgs self-coupling and the top-Higgs Yukawa coupling are now possible. We show studies comparing differential distributions for fixed-order NLO to parton-shower matched predictions, and discuss parton-shower related uncertainties. Finally, we summarize the current state of the SM and outline future, potentially interesting developments in both top-quark and Higgs physics.

274

## Part I

275

# Theoretical & Experimental Setup



## <sup>276</sup> 2 The Standard Model

<sup>277</sup> The SM was developed and supplemented over five decades, and describes all elementary  
<sup>278</sup> particles and their interactions via three of the four fundamental forces in a quantum-field  
<sup>279</sup> theoretical framework: the electromagnetic, weak and strong interactions. Although it  
<sup>280</sup> is known that the SM suffers from some theoretical shortfalls that are briefly described  
<sup>281</sup> at the end of this Chapter (like measured non-zero neutrino masses), there is, to date,  
<sup>282</sup> no experimental evidence that directly contradicts it.

<sup>283</sup> At the core, the discovery by Glashow, Salam and Weinberg [20–22] that the elec-  
<sup>284</sup> tronagnetic and weak interactions could be embedded in a unified theory constitutes  
<sup>285</sup> the first stone of the SM edifice. What if all known forces and particles could be de-  
<sup>286</sup> scribed by the same, unique theory? Since that time, the electroweak (EW) theory of  
<sup>287</sup> interactions gradually incorporated the quantum chromodynamics (QCD) sector, which  
<sup>288</sup> describes the strong interaction. The addition of the Higgs mechanism, that generates  
<sup>289</sup> mass terms for the fermions and gauge bosons, culminated in what is known today as the  
<sup>290</sup> SM Lagrangian. The SM is one of the most successful theories up-to-date, and has been  
<sup>291</sup> extensively tested against experimental data. A comprehensive comparison of computed  
<sup>292</sup> cross-sections for SM processes to values measured by ATLAS, shown in Fig. 2.1, makes  
<sup>293</sup> for a compelling argument in favor of the SM’s predictive power.

### <sup>294</sup> 2.1 Matter content and gauge interactions

<sup>295</sup> The SM is a quantum-field gauge theory: the known elementary particles are interpreted  
<sup>296</sup> as the excitations of quantized fields, and their interactions are described by the exchange  
<sup>297</sup> of gauge bosons. Both matter and gauge fields obey certain rules under the corresponding  
<sup>298</sup> gauge transformations: that is, they transform according to different representations of  
<sup>299</sup> the underlying gauge group. The SM builds on the

$$SU(3)_C \times SU(2)_L \times U(1)_Y$$

<sup>300</sup> gauge group. It is the product group of the QCD group  $SU(3)_C$ , and its corresponding  
<sup>301</sup> color quantum number  $C$ , and the electroweak group  $SU(2)_L \times U(1)_Y$ , that distinguishes  
<sup>302</sup> left- from right-handed particles as doublets, respectively singlets under the group trans-  
<sup>303</sup> formation. The  $U(1)_Y$  group’s quantum number is the so-called hypercharge  $Y$ . The  
<sup>304</sup> fermionic matter fields are classified into left-handed leptons and quarks, both transform-  
<sup>305</sup> ing as doublets under the  $SU(2)_L$  group, and their singlet right-handed counterparts.  
<sup>306</sup> There are furthermore three distinct copies, called generations, or families:

2 The Standard Model

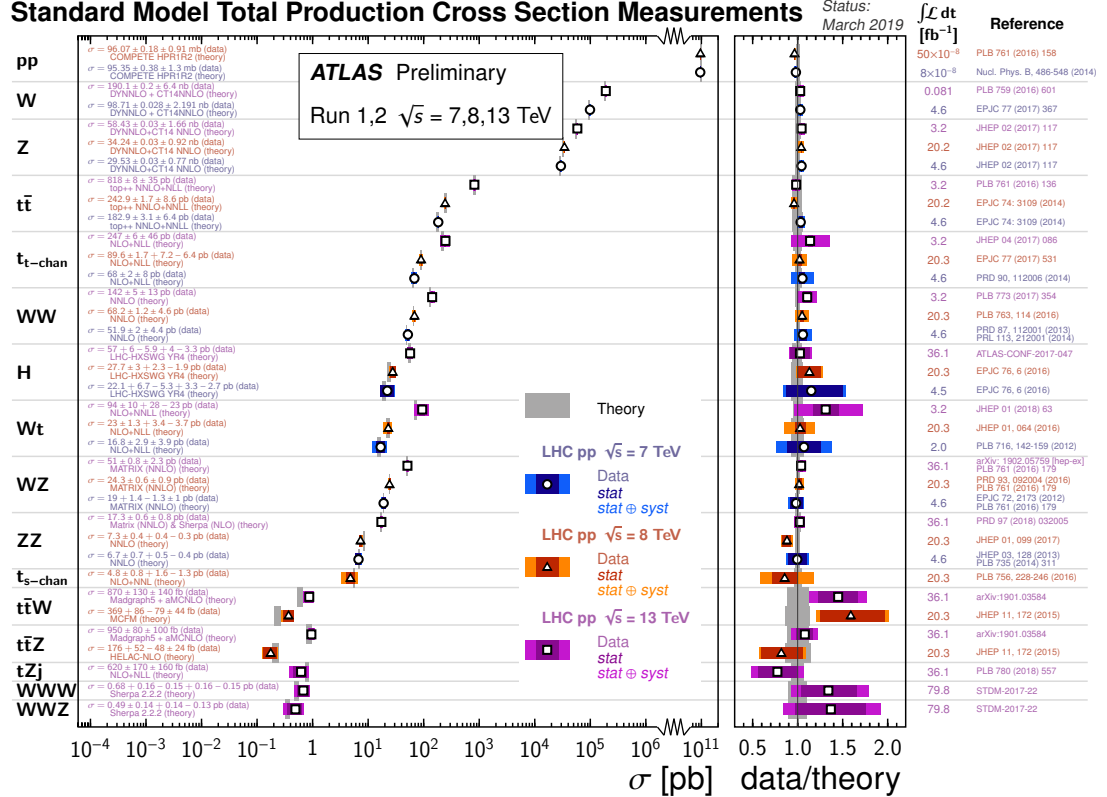


**Figure 2.1:** The predicted cross-sections (in gray, where bands represent the theoretical uncertainty) for SM production processes at LHC center-of-mass energies of  $\sqrt{s} = 7, 8, 13$  TeV are compared to their measured values at the ATLAS experiment (in color) [23]. The ratio of data to theory is shown to be compatible with 1.

$$\begin{pmatrix} \nu_e \\ e^- \end{pmatrix}_L, \quad \begin{pmatrix} u \\ d' \end{pmatrix}_L \quad \quad \quad \begin{pmatrix} \nu_\mu \\ \mu^- \end{pmatrix}_L, \quad \begin{pmatrix} c \\ s' \end{pmatrix}_L \quad \quad \quad \begin{pmatrix} \nu_\tau \\ \tau^- \end{pmatrix}_L, \quad \begin{pmatrix} t \\ b' \end{pmatrix}_L$$

$$e_R^-, \quad u_R, \quad d'_R \qquad \qquad \mu_R^-, \quad c_R, \quad s'_R \qquad \qquad \tau_R^-, \quad t_R, \quad b'_R$$

and their corresponding antiparticles. The down-type quark weak eigenstates mix via the unitary Cabibbo-Kobayashi-Maskawa (CKM) matrix to give the physical mass eigenstates:

$$\begin{pmatrix} d' \\ s' \\ b' \end{pmatrix} = \begin{pmatrix} V_{ud} & V_{us} & V_{ub} \\ V_{cd} & V_{cs} & V_{cb} \\ V_{td} & V_{ts} & V_{tb} \end{pmatrix} \begin{pmatrix} d \\ s \\ b \end{pmatrix}.$$

The quarks are the only matter fields carrying color charge, and live in the triplet (**3**), respectively anti-triplet ( **$\bar{3}$** ) representations of the  $SU(3)_C$  group. The color quantum

## 2.1 Matter content and gauge interactions

312 numbers are defined as red, blue and green, respectively anti-red, anti-blue and anti-  
313 green. That is, for the up- and down-quark:

$$\begin{pmatrix} u_r \\ u_b \\ u_g \end{pmatrix}, \quad \begin{pmatrix} d_r \\ d_b \\ d_g \end{pmatrix} \in SU(3)_C.$$

314 Governing the interactions, the gauge bosons corresponding to each subgroup couple  
315 with a separate strength to the matter fields:

- 316 • three  $W_\mu^a$ ,  $a = (1, 2, 3)$ , bosons belonging to  $SU(2)_L$ , coupling with strength  $\propto g$ ,
- 317 • one  $B_\mu$  boson belonging to  $U(1)_Y$ , coupling with strength  $\propto g'$ ,
- 318 • eight gluon fields  $G_\mu^a$ ,  $a = (1, \dots, 8)$ , belonging to  $SU(3)_C$ , with coupling  $\propto g_s$ .

319 By the principle of gauge covariance, the interaction terms between gauge bosons and  
320 the rest of the particle fields are given by promoting the 4-derivatives in the kinetic terms  
321 of the corresponding sector to covariant derivatives:

$$\partial_\mu \rightarrow D_\mu = \left[ \partial_\mu + ig \frac{\sigma_a}{2} W_\mu^a + ig' \frac{Y}{2} B_\mu \right] \quad (\text{EW}), \quad (2.1)$$

322

$$\partial_\mu \rightarrow D_\mu = [\partial_\mu + ig_s T_a G_\mu^a] \quad (\text{QCD}), \quad (2.2)$$

323 where  $\sigma_a$  are the three Pauli matrices (the generators of the Lie algebra of  $SU(2)_L$ ),  
324 and  $T_a$  are the eight generators of the Lie algebra of  $SU(3)_C$ . The replacement by a  
325 covariant derivative also induces gauge boson self-coupling interactions

326 Finally, analogously to the quarks, the electroweak gauge bosons mix to give rise to  
327 the physical charged- and neutral-current interaction bosons:

$$W^\pm = \frac{1}{\sqrt{2}} (W^1 \mp iW^2), \quad (2.3)$$

$$\begin{pmatrix} \gamma \\ Z \end{pmatrix} = \begin{pmatrix} \cos(\theta_W) & \sin(\theta_W) \\ -\sin(\theta_W) & \cos(\theta_W) \end{pmatrix} \begin{pmatrix} B \\ W^3 \end{pmatrix}, \quad (2.4)$$

328 where  $\theta_W$  is the Weinberg angle.

## 329 2.2 The Higgs mechanism

330 If one writes down the most general, renormalizable Lagrangian for the model above,  
 331 two problems appear:

- 332 • the usual Dirac mass terms appearing in the fermionic sector are not invariant  
 333 under  $SU(2)_L$ ,
- 334 • mass terms for the  $W^\pm$ ,  $Z$  bosons are not gauge-invariant.

335 So, in order to generate masses for the aforementioned particles, an external contrap-  
 336 tion is needed. The Brout-Englert-Higgs [24–26] mechanism proposed in 1964 introduces  
 337 a new spin-0 fundamental  $SU(2)_L$  doublet, called the Higgs field:

$$\phi(x) = \begin{pmatrix} \phi^+(x) \\ \phi^0(x) \end{pmatrix}. \quad (2.5)$$

338 It is colorless, and is charged under the electroweak  $U(1)_Y$  symmetry. The  $SU(3)_C \times$   
 339  $SU(2)_L \times U(1)_Y$  Lagrangian gets completed by a (gauged) Higgs sector, where the  
 340 covariant derivative  $D_\mu$  is given by Eq. (2.1):

$$\mathcal{L}_h = (D_\mu \phi)^\dagger (D^\mu \phi) + V(\phi) \quad (2.6)$$

$$= (D_\mu \phi)^\dagger (D^\mu \phi) + \mu^2 \phi^\dagger \phi - \lambda (\phi^\dagger \phi)^2, \quad \lambda > 0. \quad (2.7)$$

341 Similarly to the case of superconductivity [27], the underlying  $SU(2)_L \times U(1)_Y$  sym-  
 342 metry can be spontaneously broken if the Higgs potential  $V(\phi)$  has a non-zero ground  
 343 state. This is the case for the *Mexican-hat* potential given above, which is pictured in  
 344 Fig. 2.2. When the Higgs field assumes one of the degenerate ground states with a vac-  
 345 uum expectation value at the minimum of the potential around  $v = \mu/\sqrt{\lambda} \sim 246$  GeV,  
 346 it spontaneously breaks the  $SU(2)_L \times U(1)_Y$  symmetry of the Lagrangian.

347 Expanding the Higgs field from Eq. (2.5) around the vacuum and taking the EW  
 348 covariant derivative from Eq. (2.1),

$$\phi(x) = \frac{1}{\sqrt{2}} \begin{pmatrix} 0 \\ v + h(x) \end{pmatrix}, \quad (2.8)$$

$$D_\mu \phi(x) = \frac{1}{\sqrt{2}} \begin{pmatrix} -\frac{ig}{2} (W_\mu^1 - iW_\mu^2) (v + h(x)) \\ \partial_\mu h(x) - \frac{i}{2} (g'B_\mu - gW_\mu^3) (v + h(x)) \end{pmatrix}, \quad (2.9)$$

349 the Higgs field naturally couples to the gauge bosons. Then, computing the squared  
 350 gauged kinematic term of the spontaneously broken Higgs field from Eq. (2.7), and  
 351 replacing the gauge fields with their physical rotated states from Eqs. (2.3), (2.4) gives:

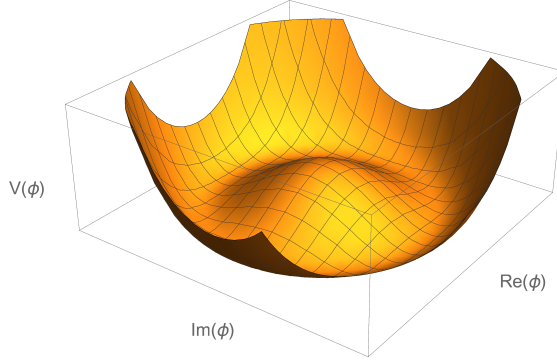


**Figure 2.2:** The  $SU(2) \times U(1)$  symmetric Higgs Mexican-hat potential has a degenerate non-zero ground state at  $v^2 = \langle \phi_0^\dagger \phi_0 \rangle \sim (246 \text{ GeV})^2$ .

$$\begin{aligned} \mathcal{L} \supset & \frac{1}{2} (\partial_\mu h)(\partial^\mu h) + \underbrace{\frac{g^2 v^2}{4}}_{m_W^2} W_\mu^+ W^{-\mu} + \frac{1}{2} \underbrace{\left( \frac{(g^2 + g'^2)v^2}{4} \right)}_{m_Z^2} Z_\mu Z^\mu \\ & + \underbrace{\frac{1}{2} (2\lambda v^2)}_{m_h^2} h^2 + \lambda v h^3 + \frac{\lambda}{8} h^4. \end{aligned} \quad (2.10)$$

352 So, the dynamic EW spontaneous symmetry breaking (EWSB) of the Higgs potential  
 353 generates masses for the  $W^\pm$ ,  $Z$  gauge bosons and identifying the mass terms in the  
 354 Lagrangian leads to following leading-order boson mass relations<sup>1</sup>:

$$\begin{aligned} m_H &= \sqrt{2\lambda}v, \\ m_W &= \frac{gv}{2}, & \cos(\theta_W) &= \frac{g}{\sqrt{g^2 + g'^2}}, \\ m_Z &= \frac{\sqrt{g^2 + g'^2}v}{2}, & \sin(\theta_W) &= \frac{g'}{\sqrt{g^2 + g'^2}}. \\ m_\gamma &= 0, \end{aligned}$$

356 The  $W$  and  $Z$  boson masses are related (at tree-level):

$$m_W = m_Z \cos(\theta_W),$$

357 with the experimentally measured values  $m_W = 80.385 \text{ GeV}$ ,  $m_Z = 91.1876 \text{ GeV}$  and  
 358 the Weinberg angle  $\theta_W = 0.2223$ . Finally, considering the last two terms in Eq. (2.10),  
 359 the Higgs couples to itself to produce the Feynman diagrams shown in Fig. 2.3.

---

<sup>1</sup>The introduction of the Higgs mechanism also allows for a fermionic gauge-invariant mass term, e.g. by the Yukawa coupling of fermions to the Higgs boson  $\mathcal{L} \supset \frac{m_f}{2v} \bar{\psi}_f \psi_f h \xrightarrow{(h \rightarrow v)} \frac{1}{2} m_f \bar{\psi}_f \psi_f$ .

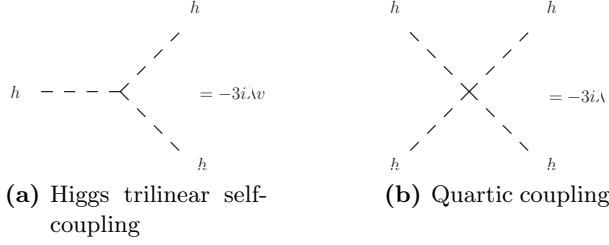


**Figure 2.3:** The physical Higgs field couples to itself after EWSB. The Feynman rules are given for (a) the triple vertex and (b) the quartic vertex.

360 As a side note, expressing Eq. (2.5) with all available degrees of freedom would give,  
361 in polar coordinates,

$$\phi(x) = \frac{v + h(x)}{\sqrt{2}} e^{\frac{i}{v} \chi_a(x) \sigma^a} \begin{pmatrix} 0 \\ 1 \end{pmatrix}, \quad (2.11)$$

362 where the three fields  $\chi_a$  are the massless Goldstone bosons associated with the EWSB  
363 of  $SU(2) \times U(1)$ . Because they will anyhow disappear from the theory (their respective  
364 degrees of freedom are sacrificed to the  $W$ - and  $Z$ -bosons' longitudinal polarizations),  
365 we do not explicitly consider them in the following. Combining the matter and gauge  
366 terms with the Higgs sector yields the final form of the SM Lagrangian:

$$\begin{aligned} \mathcal{L}_{\text{SM}} = & -\frac{1}{2} \langle G_{\mu\nu} G^{\mu\nu} \rangle - \frac{1}{2} \langle W_{\mu\nu} W^{\mu\nu} \rangle - \frac{1}{4} B_{\mu\nu} B^{\mu\nu} \\ & + \sum_{\psi=q_L,l_L,q_R,l_R} \bar{\psi} i \not{D} \psi + \text{h.c.} \\ & + Y_l \bar{\psi}_L \phi \psi_R + Y_d \bar{q}_L \phi d_R + Y_u \bar{q}_L \phi u_R + \text{h.c.} \\ & + (D_\mu \phi)^\dagger (D^\mu \phi) + \mu^2 \phi^\dagger \phi - \lambda (\phi^\dagger \phi)^2, \end{aligned} \quad (2.12)$$

367 where  $\langle \cdot \rangle$  represents the trace. The first line contains the field-strength tensors of  
368 the corresponding gauge bosons, e.g. for a gauge group with structure functions  $f^{abc}$   
369 defined by the generators  $[T_a, T_b] =: i f^{abc} T_c$  of the corresponding Lie algebra, and general  
370 coupling strength  $\tilde{g}$ :

$$F_{\mu\nu}^a = \partial_\mu A_\nu^a - \partial_\nu A_\mu^a + \tilde{g} f^{abc} A_\mu^b A_\nu^c.$$

<sup>371</sup> For the three SM subgroups:

- $SU(3)_C$ 
  - $A_\mu^a := G_\mu^a$  the gluon field in the adjoint representation
  - $\tilde{g} := g_s$  the strong coupling constant
  - $[T_a, T_b] =: if^{abc}T_c$  with the generators given in Eq. (2.2).
- $SU(2)_L$ 
  - $A_\mu^a := W_\mu^a$  the gauge field defined in Eq. (2.1)
  - $\tilde{g} := g$  the  $SU(2)_L$  coupling constant
  - $[\sigma_a, \sigma_b] =: if^{abc}\sigma_c$  with the Pauli matrices  $\sigma_i$ .
- $U(1)_Y$ 
  - $A_\mu^a := B_\mu$  the last gauge field appearing in Eq. (2.1)
  - $\tilde{g} := g'$  the  $U(1)_Y$  coupling constant
  - $f^{abc} = 0$  since the group is Abelian.

<sup>374</sup> The second line of the SM Lagrangian contains the kinetic and interaction terms for  
<sup>375</sup> the fermion fields, where  $D = \gamma^\mu \partial_\mu$ . The third line contains the Yukawa interaction of  
<sup>376</sup> all fermions with the Higgs boson for mass generation, and the last line is the unbroken  
<sup>377</sup> SM Higgs boson sector.

## <sup>378</sup> 2.3 Top-Higgs interactions

<sup>379</sup> Intrinsically, the top-quark is tightly linked to the Higgs boson properties and has gen-  
<sup>380</sup> erally strong phenomenological implications for the Higgs sector. Because it is the  
<sup>381</sup> heaviest SM elementary particle, and since the Yukawa coupling of the Higgs boson  
<sup>382</sup> to fermions is proportional to their masses, the Higgs couples strongest to the top-quark  
<sup>383</sup> (in comparison, bottom-quark effects in inclusive Higgs observables are of the order of  
<sup>384</sup>  $m_b/m_t = 2.8\%$ ). It is especially important for Higgs production at the LHC: the pre-  
<sup>385</sup> dominant production mechanism is gluon-fusion via a triangle top-quark loop, as shown  
<sup>386</sup> in Fig. 2.4. In comparison, other associated production modes have cross-sections that  
<sup>387</sup> are more than one order of magnitude smaller. The Feynman diagrams for the main  
<sup>388</sup> production channels at LHC are also depicted in Fig. 2.5.

<sup>389</sup> In relation to both the measurement of the Higgs triple self-coupling and the impor-  
<sup>390</sup> tance of top-mass effects in Higgs production, the reader is referred to the extensive  
<sup>391</sup> discussion laid out in Chapter 10. Not only do top-quarks influence Higgs processes  
<sup>392</sup> cross-sections at collider experiments, but they also have a deeper connection to the  
<sup>393</sup> Higgs potential. Indeed, the  $\beta$ -function of the Higgs quartic coupling (which governs the  
<sup>394</sup> evolution of the coupling's value at different resolution scales, see Chapter 3) is sensitive  
<sup>395</sup> to renormalization counterterms stemming from top-quark loops. Eq. (2.13) gives the  
<sup>396</sup> one-loop  $\beta$ -function for the Higgs quartic coupling [29]:

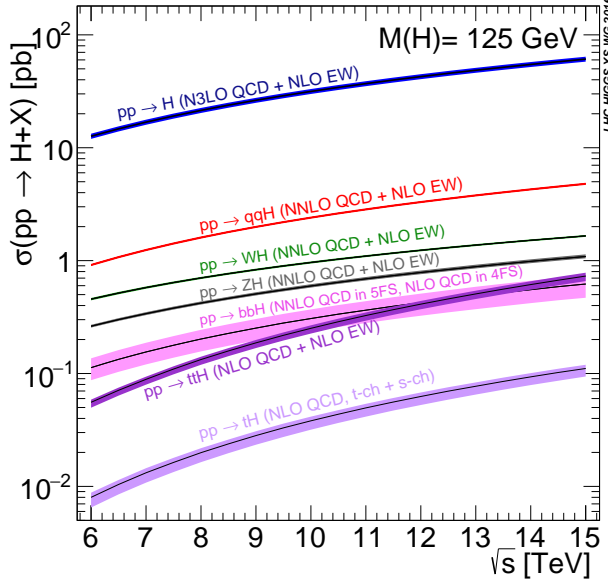


**Figure 2.4:** Theory prediction for  $pp \rightarrow h + X$  production cross-sections as a function of the center-of-mass energy  $\sqrt{s}$ . Single Higgs production at the LHC is dominated by gluon fusion mediated by a top-quark loop. Figure taken from Ref. [28].

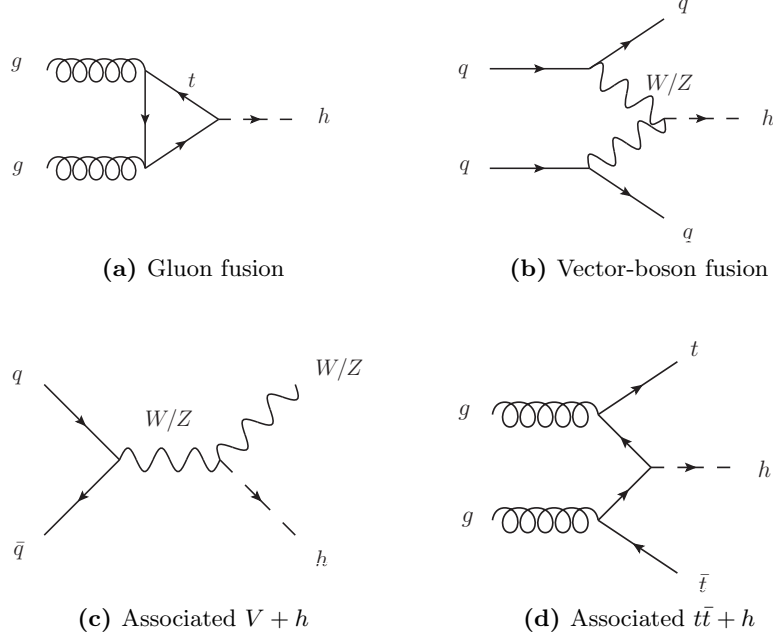


**Figure 2.5:** Leading-order diagrams for Higgs production by (a) gluon fusion, (b) vector-boson fusion, (c) associated vector production and (d) associated  $t\bar{t}$  production.

$$\mu^2 \frac{d\lambda}{d\mu^2} = \beta_\lambda(\lambda, y_t, g_s, \dots) = \frac{1}{16\pi^2} (12\lambda^2 + 6\lambda y_t^2 - 3y_t^4), \quad y_t = \sqrt{2} \frac{m_t}{v} \sim 1 \quad (2.13)$$

397 where  $y_t$  is the top-Yukawa coupling and is proportional to the top-quark mass  $m_t$ .  
 398 Because the top-Yukawa coupling is of order  $\mathcal{O}(1)$ , small variations in the value of  
 399 the top-quark mass modify the evolution of the Higgs quartic coupling  $\lambda$  in a non-  
 400 trivial way. If  $\lambda(\mu)$  was to become negative at scales much below the Planck scale,  
 401  $M_P \sim 10^{18} - 10^{19}$  GeV (see Fig. 2.6a), the Higgs field could tunnel from the current false  
 402 vacuum state to the true, absolutely stable vacuum ground state. Current measurements  
 403 seem to support the fact that the SM is in a metastable state, as shown in Fig. 2.6b. For  
 404 the existentially anxious reader, a state-of-the art calculation of the EW vacuum decay  
 405 rate can be found in Ref. [30].

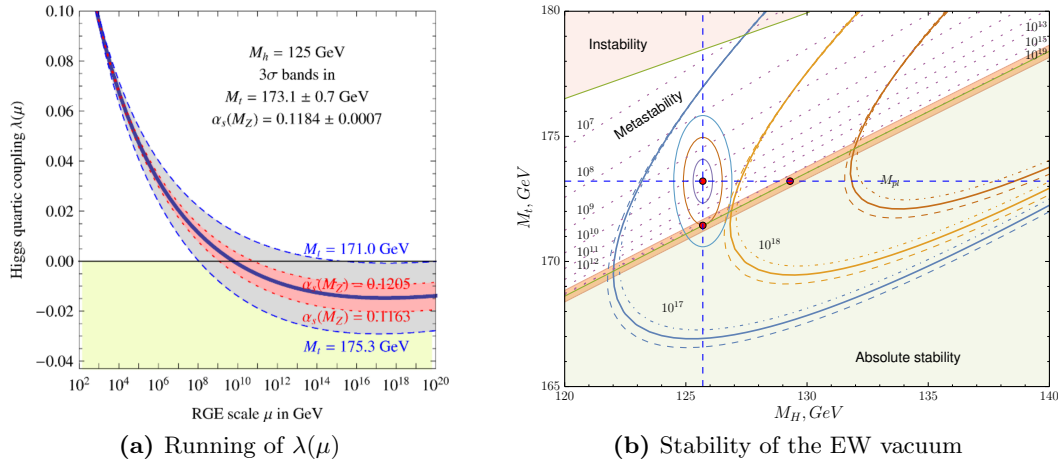


**Figure 2.6:** (a) The RGE evolution of the Higgs quartic coupling  $\lambda$  can lead to negative values at high energy scales (below the Planck scale  $M_P$ ). This in turn makes the EW vacuum potentially unstable. The running is highly dependent on the top-quark mass and  $\alpha_s$  values [31]. (b) The SM point, in red, is plotted in the  $(m_h, m_t)$  phase-space with  $1-, 2-$  and  $3\sigma$  uncertainties. The pink dotted lines indicate contours where  $\lambda(\mu) = 0$  for the indicated values of  $\mu$ , and the parabolic curves where the beta-function  $\beta_\lambda(\mu) = 0$  for chosen values of  $\mu$ . The measured Higgs and top-quark masses point to a SM universe close to the metastable region [32].

## 406 2.4 Outstanding issues with the SM

407 For all its successes, the SM is known to have some theoretical flaws. Below is a list of  
 408 familiar shortcomings:

- 409 • **Massless neutrinos:** In the SM, neutrinos are naturally massless. Experi-  
 410 ments [33] have shown that neutrinos can oscillate between the different families,

## 2 The Standard Model

411 and this requires a mixing of flavor states with mass eigenstates, similarly to the  
412 CKM mixing. Different mechanisms were introduced to generate neutrino masses:  
413 a right-handed (so-called *sterile*) neutrino could exist, and not interact with matter  
414 (no right-handed neutrino was ever observed), or neutrinos could acquire a Major-  
415 rana mass. Some R-parity violating supersymmetric (SUSY) models also produce  
416 neutrino masses [34, 35].

- 417 • **Gravity:** General relativity has yet to be quantized and incorporated into the SM  
418 under its current form, and a unified theory of all four interactions is still missing.  
419 As a first attempt, an exchange gravitational gauge boson can be introduced under  
420 the form of a spin-2 particle, called the graviton. The addition of corresponding  
421 terms to the SM Lagrangian spawns the apparition of UV divergences that cannot  
422 be handled by a finite number of counterterms, though, and the theory is not  
423 perturbatively renormalizable.
- 424 • **Dark matter:** The presence of dark matter in the Universe has been suggested  
425 from multiple cosmological observations. Yet, the SM does not contain a good  
426 dark matter candidate particle. Some extensions of the SM, in particular SUSY,  
427 provide a heavy non-decaying particle (the lightest in the SUSY spectrum, called  
428 light supersymmetric particle (LSP)) that turns out to be a good candidate.
- 429 • **Baryon asymmetry:** The SM predicts that matter and antimatter should have  
430 been produced almost symmetrically at the Big Bang. Yet baryons are observed  
431 to be in overwhelming excess over antibaryons in our part of the Universe.
- 432 • **Hierarchy problem:** There is a manifest imbalance between the three unified  
433 forces of the SM and gravity, or between their respective mass scales. In particular,  
434 it is not clear why the Higgs boson mass is so small with respect to the Planck scale:  
435 basically, radiative corrections to the Higgs self-energy should blow up its mass, and  
436 the observed value of  $m_h = 125$  GeV requires an incredible amount of fine-tuning to  
437 cancel radiative corrections. Again, SUSY models solve this problem by requiring  
438 every SM particle to have a supersymmetric partner which has the opposite spin-  
439 statistics: their contributions to the Higgs mass then cancel naturally.

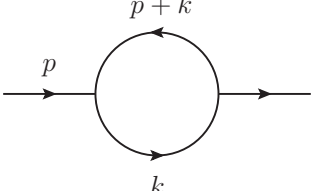
440 Although all model extensions of the SM have respective advantages over the current  
441 theory, none of the particles predicted by them has been observed at the LHC or any  
442 other experiment yet.

# 443 3 Higher-order perturbative calculations in 444 hadron-hadron collisions

445 The SM Lagrangian presented in the last Chapter provides the Feynman rules to com-  
 446 pute theoretical cross-sections. As will be explained in Section 3.1.3, the scattering  
 447 amplitudes (at high-energies, for QCD) can be expanded to a perturbative series in the  
 448 coupling constant: the interactions are represented by Feynman diagrams, and higher-  
 449 order corrections generate loop diagrams that are most of the time divergent. Since  
 450 the first successes of QFT in predicting basic energy spectrum properties and leading-  
 451 order (LO) scattering amplitudes, there has always been a need for a more consistent  
 452 framework in which higher-order corrections could be worked out. In this Chapter, we  
 453 summarize the important ingredients used in most theoretical computations nowadays,  
 454 in particular in the context of high-energy hadron-hadron collisions.

## 455 3.1 Divergences in QFT

456 Going beyond Feynman tree diagrams in the computation of scattering matrix-elements,  
 457 one encounters two classes of divergences. Consider a one-loop scalar massless two-point  
 458 function, where the internal loop-momentum is integrated over:

459 

$$I_2(p^2; 0, 0) = \int_{-\infty}^{\infty} \frac{d^4 k}{(2\pi)^4} \frac{1}{(k^2 + i\delta)((p+k)^2 + i\delta)} . \quad (3.1)$$

460 In the limit  $|k| \rightarrow \infty$ , the integral behaves as  $I \propto \int \frac{dk k^3}{k^2 \cdot k^2} = \int \frac{dk}{k}$  which is logarithmically  
 461 divergent. The integral is also divergent when taking the limit  $k \rightarrow 0$ . These are  
 462 called *ultraviolet*, respectively *infrared* divergences.

463 As a solution to the infinities conundrum, the above integral has to be treated by the  
 464 introduction of a UV cutoff of some kind – this is a method called *regularization*, and  
 465 by absorbing the regularized infinities in a consistent way through the *renormalization*  
 466 of the Lagrangian bare couplings and masses.

### 467 3.1.1 Regularization

468 A first attempt at controlling UV divergences consists in the introduction of a high-  
 469 momentum regulator  $k^2 < \Lambda^2$ . Then, the loop integral given in Eq. (3.1) behaves as

$$I_2(p^2; 0, 0) \propto \int_{\epsilon}^{\Lambda} \frac{dk}{k} \sim \log(\Lambda) , \quad (3.2)$$

and the integral diverges logarithmically in the cutoff  $\Lambda$ . This is typical of renormalizable theories. Now, obviously, any physical observable should not depend on the value of the arbitrary cutoff, and in practice it does not.<sup>1</sup> As a theoretical downside, the introduction of the cutoff breaks gauge-invariance. It also breaks translational invariance and makes it difficult to use Feynman parameters and the corresponding variable replacements  $p \rightarrow p + k$ .

A possible gauge-invariant regularization method is the so-called Pauli-Villars regularization: a much more massive particle is introduced and its contribution subtracted from the ordinary propagator, that is:

$$\int \frac{d^4k}{(2\pi)^4} \frac{1}{k^2 + i\delta} \rightarrow \int \frac{d^4k}{(2\pi)^4} \left( \frac{1}{k^2 + i\delta} - \frac{1}{k^2 - M^2 + i\delta} \right) . \quad (3.3)$$

The Pauli-Villars technique cannot be applied to QCD because it is not gauge-covariant, though. On the same stance, it introduces an unphysical field that violates the spin-statistics theorem (it amounts to a spurious scalar field with Fermi statistics). One of the preferred regularization methods nowadays is dimensional regularization. It was refined by 't Hooft and Veltman [38] to regularize any integral, is gauge-invariant and works for non-Abelian theories as well. The governing idea is that quantum-field theories in a smaller number of dimensions have a lesser superficial degree of divergence. The four dimensions of space-time are therefore analytically continued to  $d = 4 - 2\epsilon$  dimensions, and the integral in Eq. (3.1) can be cast into the following form:

$$I_2(p^2; 0, 0) = \mu^{2\epsilon} \int \frac{d^d k}{(2\pi)^d} \frac{1}{(k^2 + i\delta)((p+k)^2 + i\delta)} , \quad (3.4)$$

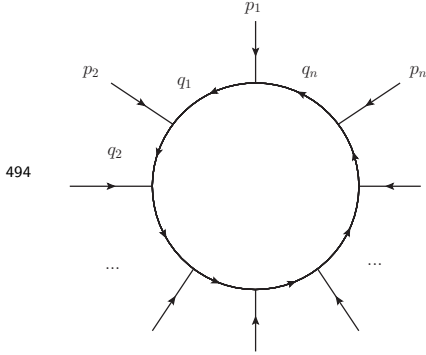
where the renormalization scale  $\mu$  is a dimensionful parameter needed to keep the integral dimensionless. Then the integral can be worked out by introducing Feynman parameters and Wick-rotating to give the analytical result

$$I_2(p^2; 0, 0) = \frac{1}{\epsilon} + \ln \frac{\mu^2}{-p^2 - i\delta} + 2 + \mathcal{O}(\epsilon) , \quad (3.5)$$

where the UV divergences now appear as (at most double, at one-loop) poles in the dimensional regulator  $\epsilon$ . A general dimensionally-regularized one-loop scalar integral with  $n$  external legs has the form:

---

<sup>1</sup>For a fun exercise of trying out different forms of cutoff (Gaussian, Dirac-delta,...), see Ref. [36] for the case of the vacuum polarization in the Casimir effect [37].



$$I = \mu^{n-d/2} \int \frac{d^d k}{(2\pi)^d} \prod_{j=1}^n \frac{1}{(q_j^2 - m_j^2 + i\delta)}, \quad (3.6)$$

495 where the internal momenta  $q_j = k + \sum_{i=1}^j p_i$  are expressed as a linear combination of  
 496 the loop momentum  $k$  and the external momenta  $p_i$ . Systematic Feynman parameters  
 497 can be found for the integral above, and generally it can be recast into the form

$$I = \Gamma(n - d/2) \prod_{i=1}^n \int_{0 \leq x_i \leq 1} dx_i \delta \left( 1 - \sum_{j=1}^n x_j \right) \frac{\mathcal{U}^{n-d}(\vec{x})}{\mathcal{F}^{n-d/2}(\vec{x}, p_i \cdot p_j, m_i^2)}. \quad (3.7)$$

498 The  $x_1, \dots, x_n$  are the Feynman parameters, and  $\mathcal{U}, \mathcal{F}$  are the first, respectively second  
 499 Symanzik polynomials.<sup>2</sup> Then, one needs only perform the integration over the Feynman  
 500 parameters. Most importantly, all one-loop integrals can be reduced to a linear com-  
 501 bination of a set of *master integrals* that are at most box-diagrams: a one-loop master  
 502 integral basis is thus composed of at most tadpoles, bubbles, triangles and boxes, which  
 503 are all known analytically and implemented in integral libraries. Finally, for tensor in-  
 504 tegrals where the numerator of Eq. (3.6) contains Lorentz indices, there exist methods  
 505 for their reduction to a set of scalar integrals, like the systematic Passarino-Veltman  
 506 method [39] which uses a form factor expansion to factorize the indices. For the inter-  
 507 ested reader, Refs. [40–43] supply a comprehensive examination of various techniques  
 508 for reducing and evaluating Feynman integrals.

509 Dimensional regularization has lots of benefits, and the algebra is quite straightfor-  
 510 ward. Its major disadvantage is that the Dirac algebra for fermions has to be analytically  
 511 extended to  $d = 4 - 2\epsilon$  space-time dimensions as well, which is not trivial. The Dirac  
 512 matrices obey an analytically continued Clifford algebra

$$\{\gamma^\mu, \gamma^\nu\} = 2g^{\mu\nu} \quad (3.8)$$

513 with a  $d$ -dimensional metric,  $g^{\mu\nu}g_{\mu\nu} = d$ , where it is but unclear what happens to the  
 514 last Dirac matrix  $\gamma_5 = i\gamma_0\gamma_1\gamma_2\gamma_3$ . The different ways of treating  $\gamma_5$  and the helicities of  
 515 external and internal particle fields lead to different regularization schemes. Note that  
 516 physical observables do not depend on the chosen scheme. In the dimensional reduction  
 517 scheme (DRED) which we use for the predictions given in Chapters 6–11, the Dirac  
 518 algebra is left to  $d = 4$  dimensions, and the same holds for all external momenta and  
 519 helicities. Only the internal momenta are analytically continued to  $d$ -dimensions.

---

<sup>2</sup>Eq. (3.7) can also be generalized to a Feynman integral for  $l$  loops,  $n$  external and  $m$  internal momenta

520 **3.1.2 Renormalization**

521 As a way to treat the infinities arising from the UV region of integration, the bare param-  
 522 eters of the Lagrangian are redefined to absorb the divergent contributions. Although  
 523 this seems mathematically shaky, it is remarkable that the redefinition of a finite number  
 524 of parameters allows for the treatment of divergences order-by-order and for all Feynman  
 525 diagrams contributing to the amplitude of a renormalizable theory. In practice, renor-  
 526 malization of the Lagrangian is achieved by rewriting the bare masses and couplings  $m_0$   
 527 and  $g_0$ , as well as the fields themselves  $\psi_0$ , as a physical (measurable) parameter and a  
 528 counterterm

$$\begin{aligned} m_0 &= Z_m m = m + \delta m \\ g_0 &= Z_g g = g + \delta g \\ \psi_0 &= \sqrt{Z} \psi . \end{aligned} \tag{3.9}$$

529 The only requirement is that diagrams corresponding to the counterterms should can-  
 530 cel UV divergences stemming from the bare Lagrangian. In principle, the procedure does  
 531 not define how to handle the finite terms accompanying these diagrams: depending on  
 532 the additional criteria, several renormalization schemes can be chosen (on-shell, MS, MS,  
 533 or others). Here as well, the physical observables should be independent of the choice  
 534 of scheme (the top-quark mass is a fringe example and will be discussed summarily in  
 535 Chapter 6).

536 The physical parameters entering the Lagrangian, e.g. the masses and couplings  $m, g$ ,  
 537 have to be determined by experiment. By definition, they are measured at a given energy  
 538 scale. Colloquially, a renormalization starting point is chosen: the couplings/masses are  
 539 then said to *run* with the scale at which they are defined. Notably, the renormalized  
 540 field theory runs according to the Callan-Symanzik [44–46] equation, which governs the  
 541 dependence of the  $n$ -point correlation functions on the model's parameters by asking  
 542 that the bare Green's functions  $G_0^{(n)}(x_1, \dots, x_n; m_0, g_0)$  do not depend on the variations  
 543 given in Eq. (3.9):

$$\left( m \frac{\partial}{\partial m} + \beta(g) \frac{\partial}{\partial g} + n\gamma \right) G^{(n)}(x_1, \dots, x_n; m, g) = 0 , \tag{3.10}$$

544 where the  $\beta$ -function of the theory is defined as  $\beta(g) = \frac{m}{\delta m} \delta g$ , and the anomalous  
 545 dimension is given by  $\gamma = \frac{m}{\delta m} \frac{\delta \sqrt{Z}}{\sqrt{Z}}$ . Eq. (3.10) is an example of a broad class of evolution  
 546 equations called renormalization group equations (RGE).

547 **3.1.3 Perturbative expansion of QCD**

548 From the running of the strong coupling constant given by the QCD  $\beta$ -function,

$$\mu_R^2 \frac{\partial \alpha_s}{\partial \mu_R^2} = \beta(\alpha_s) = - (b_0 \alpha_s^2 + b_1 \alpha_s^3 + \dots) , \tag{3.11}$$

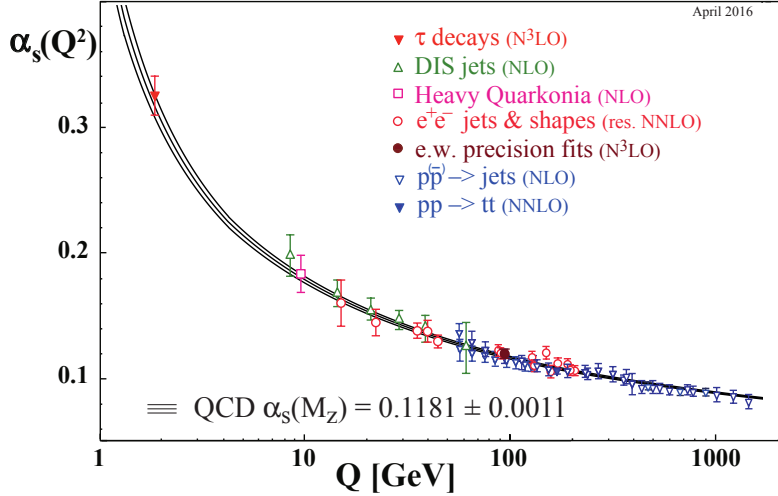


**Figure 3.1:** Various measurements of the strong coupling  $\alpha_s(Q^2)$  at different energy scales  $Q$  show the running behavior typical of QCD, with a coupling strength that becomes smaller at higher energies, and a Landau pole at the hadronization scale  $Q = \Lambda \sim 1$  GeV. Figure taken from Ref. [1].

one sees that because of the negative sign in Eq. (3.11), the strong coupling  $\alpha_s(\mu_R^2)$  becomes smaller at higher scales  $\mu_R^2$ . This running is manifest in Fig. 3.1, which shows measurements of the strong coupling  $\alpha_s$  at different energy scales  $Q$ , in agreement with the QCD theory prediction. Thus, with the measured value of the strong coupling at intermediate scales  $\alpha_s(M_Z) \approx 0.118$ , the interactions at high-energy hadron colliders can be treated perturbatively in  $\alpha_s$ . For any process cross-section  $\sigma_{ab \rightarrow X}$ , where  $a$ ,  $b$ , and  $X$  are freely propagating initial-, respectively final-states, one can expand the matrix-element in a Taylor series,

$$\hat{\sigma}_{ab \rightarrow X} = \alpha_s^k(\mu_R^2) (\hat{\sigma}_{\text{LO}}(p_i, p_f; \mu_R^2) + \alpha_s(\mu_R^2) \hat{\sigma}_{\text{NLO}}(p_i, p_f; \mu_R^2) + \mathcal{O}(\alpha_s^2(\mu_R^2)) + \dots) \quad (3.12)$$

At each order in the strong coupling  $\alpha_s$ , the cross-section can be computed and will depend on the choice of the renormalization scale. Usually it is chosen close to the expected momentum exchange  $Q^2$ . The systematic uncertainty related to the arbitrary choice of the scale is then estimated by varying the renormalization scale by factors of  $\frac{1}{2}$  and 2.

The accuracy of a computation is given by the truncation order of the perturbative series in Eq. (3.12). In certain regions of phase-space, though, large prefactors can be introduced at all orders, when two far-away scales  $Q$  and  $q$  are involved. This usually spawns the appearance of large logarithms of the form  $\ln^n(Q^2/q^2)$ , which have to be

566 resummed to a given *logarithmic* accuracy across all orders. Some details will be given  
 567 in Section 4.2.

568 **3.2 Infrared divergences**

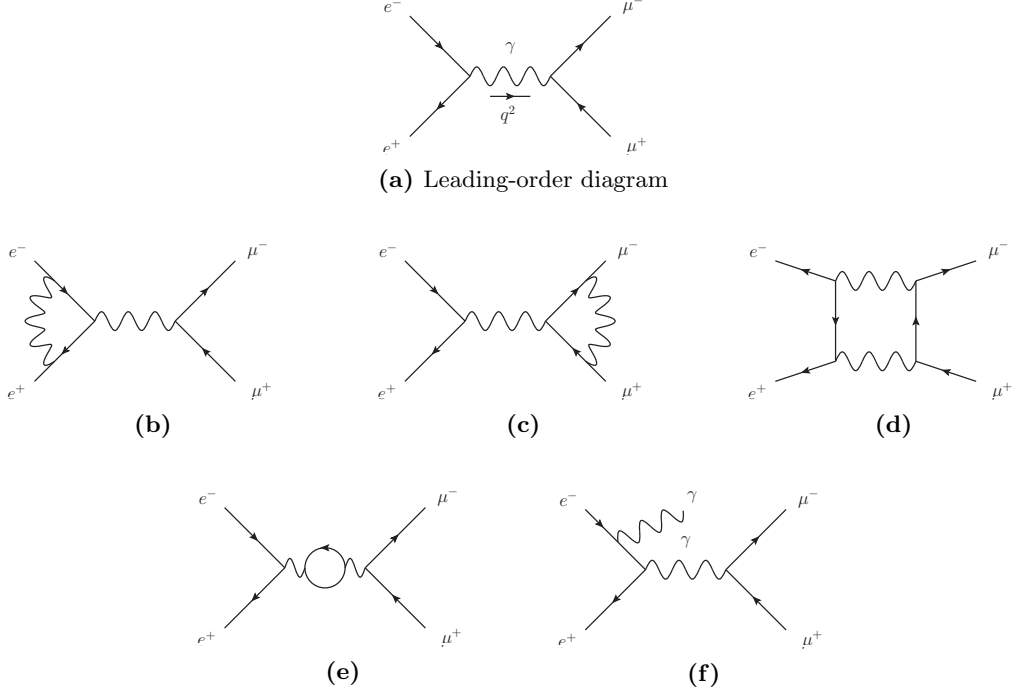


**Figure 3.2:** Feynman diagrams for  $e^+e^- \rightarrow \mu^+\mu^-$ . (a) The only leading-order diagram, with a photon in the  $s$ -channel (b-e) Virtual one-loop corrections. (f) Real-emission diagram

569 Starting from an example, let us consider the case of QED higher-order corrections to  
 570  $e^+e^- \rightarrow \mu^+\mu^-$  annihilation. Feynman diagrams up to  $\mathcal{O}(\alpha^3)$  are shown in Fig. 3.2. At  
 571 leading-order, the cross-section is given by

$$\sigma_{\text{LO}} = \int_{\Phi} d\Phi |\mathcal{M}_0|^2 = \frac{4\pi\alpha^2}{3q^2}, \quad (3.13)$$

572 where the squared amplitude  $|\mathcal{M}_0|^2$  has to be integrated over the phase-space  $\Phi$ , and  
 573  $q^2$  is the momentum carried by the exchanged photon. Let us assume the UV divergences  
 574 have been handled by the introduction of appropriate counterterms. That is, the UV  
 575 divergences stemming from the loop momentum integration from diagrams (b) and (c)  
 576 in Fig. 3.2 have been taken care of by renormalizing the electron charge and the muon  
 577 charge, respectively. Diagram (e) is also UV divergent but is nothing else than vacuum  
 578 polarization in QED (thus, it has no impact on any observable), while diagram (d) has

no UV divergence. Computing the amplitude, one realizes there is also an IR divergence coming from the massless photon propagator in the loops.

First, the IR divergence needs regularizing. The simplest way to do that is to give the photon a small, non-zero mass,  $m_\gamma > 0$ , and to take the limit  $m_\gamma \rightarrow 0$  at the end of the calculation. Computing the virtual contribution,  $\sigma_V \propto (\mathcal{M}_V^\dagger \mathcal{M}_0 + \text{h.c.})$ , one arrives at the result

$$\sigma_V = \frac{2}{3} \pi^2 \frac{\alpha^3}{q^2} \left( \frac{\pi^2}{5} - \frac{7}{2} - \ln^2 \left( \frac{m_\gamma^2}{q^2} \right) - 3 \ln \left( \frac{m_\gamma^2}{q^2} \right) \right). \quad (3.14)$$

The IR divergence is still present but it is explicit in  $\ln(m_\gamma)$ .<sup>3</sup> For the perturbative expansion to be consistent, we have to include real-emission diagrams of  $\mathcal{O}(\alpha^3)$ , that is diagrams of the sort pictured in Fig. 3.2f, where a photon is radiated either from the initial- or the final-state. Doing so, one gets a contribution of the form  $\sigma_R \propto |\mathcal{M}_R|^2$ :

$$\sigma_R = \frac{2}{3} \pi^2 \frac{\alpha^3}{q^2} \left( -\frac{\pi^2}{5} + 5 + \ln^2 \left( \frac{m_\gamma^2}{q^2} \right) + 3 \ln \left( \frac{m_\gamma^2}{q^2} \right) \right). \quad (3.15)$$

Combining the different contributions to the cross-section, the IR divergences cancel between the virtual one-loop and the real-emission matrix-elements to give a finite correction to the leading-order cross-section:

$$\sigma_{\text{NLO}} = \sigma_{\text{LO}} + \sigma_V + \sigma_R = \sigma_{\text{LO}} \left( 1 + \frac{3}{4\pi} \alpha \right). \quad (3.16)$$

This behavior is symptomatic of IR divergences and falls under the purview of the Kinoshita–Lee–Nauenberg (KLN) theorem, which states that sufficiently inclusive observables are always IR-finite.

Although the cancellation of IR divergences is ensured by the KLN theorem, it is non-trivial to realize it numerically (for example in the context of a Monte-Carlo event generator). Section 4.1.2 will briefly develop this point.

### 3.3 The factorization theorem

The collision of composite states like the protons used at LHC implies interactions of highly non-perturbative objects. It is not clear at first how to handle these theoretically: color confinement does not allow for free quarks or gluons to be observed, thus the initial-state in hadron colliders cannot a priori be defined perturbatively. At high-energy, though, we can make use of the fact that the interaction with the highest momentum exchange takes place over time scales that are far smaller than the typical time scale at which the proton's constituents interact among themselves. The description of such a collision can therefore be *factorized* in long- and short-distance (or short- and long-time

---

<sup>3</sup>The divergent terms are called Sudakov double logarithms and are systemic of collinear/soft emission (see Chapter 4).

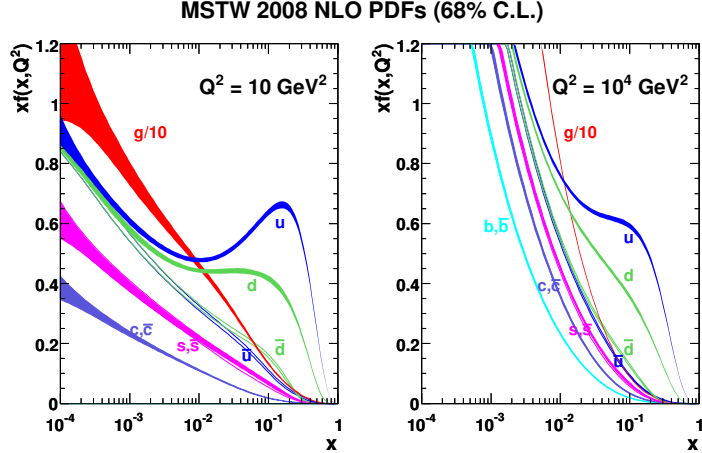


**Figure 3.3:** The MSTW 2008 NLO proton PDFs [47] as a function of the parent proton’s momentum fraction  $x$  at resolution scales  $Q^2 = 10 \text{ GeV}^2$  (left),  $Q^2 = 10^4 \text{ GeV}^2$  (right).

scale) physics: a hard collision of two freely propagating partons, respectively non-perturbative interactions within hadrons. Mathematically, the cross-section  $\sigma_{pp \rightarrow X}$  for the production of a state  $X$  from the collision of two protons can be written as

$$\sigma_{pp \rightarrow X} = \sum_{ab} \int dx_a f_{a/p}(x_a, \mu_F^2) \int dx_b f_{b/p}(x_b, \mu_F^2) \cdot \hat{\sigma}_{ab \rightarrow X}(x_a p_1, x_b p_2; \mu_F^2), \quad (3.17)$$

where  $a$  and  $b$  are possible constituents of the parent protons (sea or valence quarks and gluons),  $f_{a/p}$ ,  $f_{b/p}$  are encoding the non-perturbative origin of the partons in the parent protons, and  $\hat{\sigma}_{ab \rightarrow X}$  is the cross-section for the production of the final-state  $X$  from the collision of the free partons  $a$  and  $b$ , the latter of which can now be computed perturbatively in QCD. Eq. (3.17) is called the *factorization theorem* of Quantum Chromodynamics, and sets the basis for all cross-section predictions at LHC. The functions  $f_{a/p}$ ,  $f_{b/p}$ , which are called *parton distribution functions* (PDF), depend on the momentum fraction  $\xi_a$ ,  $\xi_b$  carried away by the parton from the parent proton, and on the resolution scale  $Q^2$ . Crudely said, the partonic content of the protons depends on the scale at which they are resolved.<sup>4</sup> The PDFs by definition cannot be computed perturbatively in QCD, but they can be measured from experimental data. As a matter of fact, a precise measurement of the proton’s PDF is crucial, and constitutes one of the main sources of uncertainty in theoretical predictions at the LHC. Fig. 3.3 depicts the measurement of the proton PDFs by the MSTW collaboration from a global fit of hard-scattering data [47].

---

<sup>4</sup>The PDFs also obey an evolution equation similar to the RGE called DGLAP equation: this evolution runs from a central scale choice, namely the *factorization scale*  $\mu_F$ .

## 625 4 Monte-Carlo event generators

626 To be able to compare a theory prediction for hadron colliders to an experimental mea-  
627 surement released by e.g. the ATLAS experiment, theorists and experimentalists meet  
628 on a common ground: the event rate  $\sigma$ . The event rate can be an inclusive cross-section,  
629 like the total rate of events after applying cuts and correcting for the detector accep-  
630 tance, or it can be a differential cross-section with respect to some kinematic variable  
631  $d\sigma/d\mathcal{O}$ , where  $\mathcal{O} = n_{\text{jets}}, m_{t\bar{t}}, \dots$  is any event observable. On one side, the theorists  
632 need to compute a cross-section from a QFT starting point, namely the Lagrangian: at  
633 the most basic level, this means implementing Fermi's golden rule (Eq. (4.1)). On the  
634 other side, experimentalists have to count events and correct for detector acceptance  
635 and resolution (Eq. (4.2)):

$$\sigma = \frac{1}{4E_a E_b v} \int \prod_f \left( \frac{d^3 p_f}{(2\pi)^3} \frac{1}{2E_f} \right) |\mathcal{M}_{fi}|^2 (2\pi)^4 \delta^4(p_a + p_b - \sum_f p_f), \quad (4.1)$$

$$\sigma = \frac{N_{\text{events}}}{\epsilon \cdot \mathcal{L}_{\text{int}}}, \quad (4.2)$$

636 where  $E_a$  and  $E_b$  are the energies of the incoming particles  $a$  and  $b$ , the flux per unit  
637 volume  $v = |\vec{v}_a - \vec{v}_b|$  is given by the relative 3-velocities of the particles and  $p_f, E_f$  are  
638 the 3-momenta and energies of all final states. As a matter of fact, the infinitesimal  
639 volume element above is relativistically invariant. Ultimately, the relativistic matrix-  
640 element squared  $|\mathcal{M}_{fi}|^2$  has to be integrated over the whole phase-space while enforcing  
641 4-momentum conservation. Experimentally, in Eq. (4.2), the cross-section is equal to  
642 the event count, corrected for phase-space acceptance, detector resolution and normal-  
643 ized by the integrated luminosity  $\mathcal{L}_{\text{int}}$ . For the case of differential distributions, the  
644 formula becomes more complicated, as binned events migrate depending on the detector  
645 resolution. The discussion of this case is postponed to Chapter 8.

646 There are two issues with the picture at hand. First, the matrix-element for a given  
647 process can typically be computed only up to  $\mathcal{O}(\text{few})$  external legs. Because the mul-  
648 tiplicity of final-state particles in a collider experiment like the LHC is of the order  
649  $\mathcal{O}(10^2 - 10^3)$ , it is virtually impossible to calculate such amplitudes. Second, the per-  
650 turbative expansion presented in Chapter 3 breaks down when colored particles are  
651 produced with small energies. In particular, around energy scales where free final-state  
652 partons fall in the realm of non-perturbative interactions, they hadronize to form the  
653 observable colorless bound states demanded by color confinement. Therefore, the struc-  
654 ture of the whole collision has to be broken down into pieces across the several scales  
655 involved, and the theoretical treatment of each piece is valid only in these subdomains  
656 and subjected to different levels of approximation. The theory community developed

## 4 Monte-Carlo event generators

the necessary ingredients to improve the description of each stage and assembled them into mostly-automated programs called *Monte-Carlo (MC) event generators*.

MC event generators basically simulate the particle collisions as they would happen at the interaction points of an experiment like ATLAS or CMS. A typical MC event is pictured in Fig. 4.1.

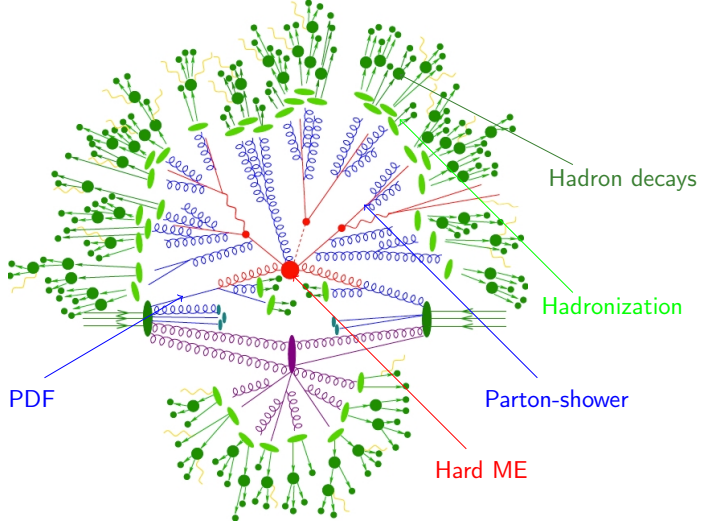


**Figure 4.1:** A Monte-Carlo event generator matches multi-scale physics to simulate a collision, taking into account non-perturbative (PDF and quark fragmentation, hadron decay, underlying event, proton beam remnants) as well as perturbative (matrix-element and parton-shower matching) phenomena.

Under the hood of any Monte-Carlo program, the ingredients are essentially the same:

- **Monte-Carlo integrator:** The phase-space is sampled, usually with the help of an adaptive Monte-Carlo integration algorithm, to numerically perform the integral given in Eq. (4.1). As a notable example, the `Cuba` library [48] implements four multi-dimensional integration algorithms: `Vegas` [49], `Divonne` [50], `Suave` [48, 51] and `Cuhre` [52].
- **PDFs:** There is an extensive amount of PDF measurements varying in the used datasets, theoretical precision, combination strategy, handling of  $\alpha_s$ , or flavour thresholds. The `LHAPDF 6` package [53] interpolates PDF values from discrete measurement points in the  $(x, Q^2)$  phase-space and can be interfaced to the MC generator.

- **Hard matrix-element:** The core of the calculation is the computation of the matrix-element  $\mathcal{M}_{fi}$ . It determines the theoretical accuracy of the prediction to a given order in  $\alpha_s$ . More details are given in Sec. 4.1.
- **Parton shower:** As stated above, the high-multiplicity endstate is evolved from the few-parton hard matrix-element through subsequent radiative emission by a parton-shower algorithm. These routines base on first-principles QCD (and QED), but contain inherent approximations and parametric degrees of freedom that generate an uncertainty associated with the choice of algorithm. Section 4.2 will expand on the topic.
- **Hadronization and hadron decay:** Once the shower evolution is brought down to energies of the order of the hadronization scale (of order  $\mathcal{O}(1 \text{ GeV})$ ), the free partons bind to form colorless states. This is handled by a model on the only assumption that it should describe data to the best possible extent. Commonly, these models have a certain number of free parameters that are *tuned* to data. In Sec. 4.3, the Lund string and the cluster model are briefly detailed.
- **Multiple partonic interaction and underlying event:** Especially at small momentum fractions, it is possible that more than one parton from the same parent proton contribute to the interaction. The description of this phenomenon is also mostly based on MC modeling and has to be tuned to experimental data.

## 4.1 Matrix-element providers

The first programs for generating the matrix-element  $\mathcal{M}_{fi}$  needed in Eq. (4.1) were highly specialized. They would handle one specific process and would be mostly analytically hard-coded. At some point, authors from the theory community started to make their code available and the corresponding libraries would be assembled into multi-processes packages. This is the example of the NLOJet++ [54] and MCFM [55] packages. Nowadays, after a paradigm shift, the computation of the hard process matrix-element is decidedly automatized at one-loop level: programs like MADGRAPH [56], OPENLOOPS [57, 58] and GoSAM [59, 60] can be interfaced directly to most MC generators and provide the amplitude given any phase-space point, while other programs focus on specific processes, as for example NJET [61], which calculates multijet amplitudes at NLO in massless QCD, VBFNLO [62–64] for vector-boson fusion in a number of processes, or HJETS++ [65] for Higgs boson production in association with one or more jets. We use GoSAM-2.0 in all subsequent NLO computations, thus the mode of operation of the program is detailed in the next Section.

### 4.1.1 GoSam: MC interfacing of one-loop amplitudes

GoSAM is a general-purpose package that computes one-loop amplitudes automatically and interfaces to any MC generator, provided it supports the Binoth-Les Houches Accord (BLHA1 [66] or BLHA2 [67]) format. The working flow of GoSAM is shown in Fig. 4.2.

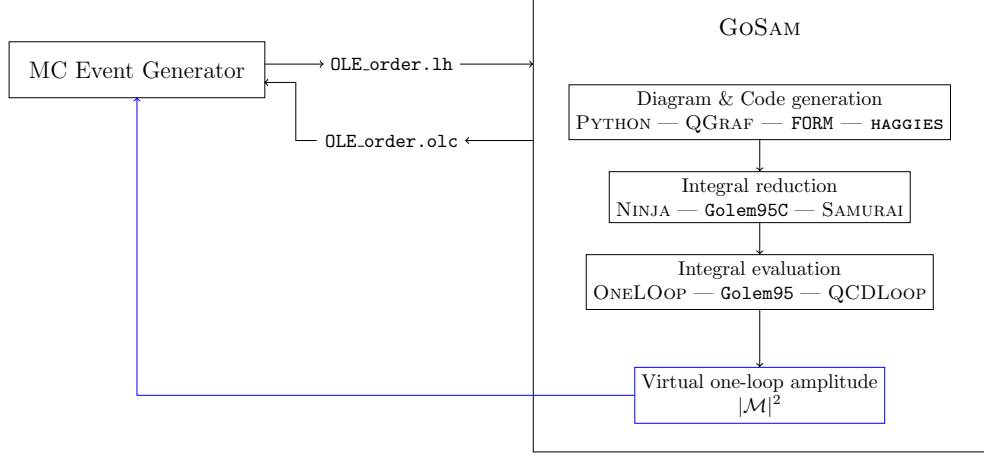


**Figure 4.2:** GoSAM relies on external packages to compute virtual one-loop amplitudes. Feynman diagrams are generated (and drawn) by QGRAF, and fortran code containing the terms relevant to each diagram is automatically written out in FORM. The various integral families are then reduced by either NINJA, Golem95C or SAMURAI libraries. Finally, the basis integrals are evaluated using either the ONELOOP, Golem95C or QCDLOOP packages.

711 Any process can be defined in the GoSAM input card, where only incoming and  
 712 outgoing particles as well as the desired order in  $\alpha, \alpha_s$  for the generation of the Feynman  
 713 diagrams have to be given. The PYTHON `gosam.py` executable is then called and a series  
 714 of external packages handle the different steps of the computation: QGRAF [68] generates  
 715 the Feynman diagrams, and filters for vertices or propagators can be applied, as well as  
 716 manual removal of diagrams. Then, FORM [69] code containing the relevant expressions is  
 717 generated automatically for all diagrams and helicities. Integral reduction is operated by  
 718 any of three programs, namely NINJA [70], Golem95C [71, 72] or SAMURAI [73]. Finally,  
 719 the evaluation of the set of basis integrals is checked out in one of the three external  
 720 integral repositories QCDLOOP [74], ONELOOP [75] or Golem95C.

721 On a higher level, in compliance with BLHA, the MC generator produces a contract  
 722 file `OLE_order.1h` containing the subprocesses to be computed by GoSAM. The latter is  
 723 called and generates routines for all subprocesses. After checking the order file, GoSAM  
 724 validates the contract and returns a control file `OLE_order.olc`. The generated libraries  
 725 for all helicities are linked, and common functions are written in a `matrix.f90` file to be  
 726 called by the MC generator. The physics parameters, like particles masses and couplings,  
 727 can be set by an external call to the `OLP_Option` function. Then, for a set of 4-momenta  
 728  $(p_i)_{i=1,\dots,n}$ , the matrix-element is provided by calling the `OLP_EvalSubProcess({p_i})`  
 729 function, which returns the full 1-loop amplitude coefficients  $c_{-2}, c_{-1}$  and  $c_0$  (double,  
 730 single pole and finite terms) as given in the Laurent series

$$|\mathcal{M}|^2 = \frac{\alpha_s}{2\pi} \frac{(4\pi)^\epsilon}{\Gamma(1-\epsilon)} \left( \frac{c_{-2}}{\epsilon^2} + \frac{c_{-1}}{\epsilon} + c_0 + \mathcal{O}(\epsilon) \right) . \quad (4.3)$$

731 GoSAM is a very flexible package, and allows high-level control over the various sub-  
732 tleties of higher-order computations (e.g. choice of regularization scheme, renormaliza-  
733 tion counterterms, and so on). A rescue system for phase-space points that are numer-  
734 ically badly behaved can be activated, and the amplitude for these is recomputed in  
735 quadruple precision.

### 736 4.1.2 Infrared divergence cancellation

737 Having acquired the virtual contribution to the amplitude, one has to combine the Born,  
738 virtual and real-emission contributions together. As was shown in Section 3.2, the sin-  
739 gularities appearing in both virtual loop calculations and in soft/collinear configura-  
740 tions of real emissions should combine to give finite quantities for any IR-safe observable.<sup>1</sup>  
741 Although this is analytically true, in the case of MC computations, the different contrib-  
742 utions are first sampled over different phase-spaces, and only then combined. Symbol-  
743 ically, we have:

$$\sigma^{\text{NLO}} = \int_{\Phi_m} d\sigma^B + \int_{\Phi_m} d\sigma^V + \int_{\Phi_{m+1}} d\sigma^R, \quad (4.4)$$

744 where the singularities in virtual and real contributions only cancel after integration.  
745 Numerically, the cancellation of IR divergences is thus non-trivial. At NLO, there are  
746 two kinds of algorithms to implement IR divergence cancellation: phase-space slicing and  
747 subtraction methods. The Catani-Seymour automatized subtraction of IR divergences  
748 is mostly used nowadays in NLO MC generators. The algorithm is outlined below and  
749 is used in all calculations present from Chapter 6 on.

750 Consider the addition of a subtraction term which approximates the ( $d = 4 - 2\epsilon$   
751 regularized) real contribution and reproduces its IR singularity pattern in  $d$  dimensions:

$$d\sigma^V + d\sigma^R = d\sigma^V + d\sigma^S + (d\sigma^R - d\sigma^S). \quad (4.5)$$

752 Then, the ( $d = 4$ )-dimension limit can be taken directly for the integration of the real-  
753 emission and the local counterterm cancels the divergence in the phase-space integrand.  
754 The same is true for the virtual contribution, in general, only after integration. Returning  
755 to the phase-space integrated result, the total NLO cross-section takes the form:

$$\sigma^{\text{NLO}} = \int_{\Phi_m} d\sigma^B + \int_{\Phi_m} \left( d\sigma^V + \int_{\Phi_1} d\sigma^S \right)_{\epsilon=0} + \int_{\Phi_{m+1}} (d\sigma^R|_{\epsilon=0} - d\sigma^S|_{\epsilon=0}), \quad (4.6)$$

756 where both of the last integrals are now separately finite. The Catani-Seymour dipole  
757 formalism is a factorization formula that allows the automatic generation of the subtrac-  
758 tion term  $d\sigma^S$ . Universal dipole factors are introduced for any process, and setting the  
759 subtraction term to

---

<sup>1</sup>Generally, at NLO, regularized poles appear either as double poles (soft and collinear), or single poles (soft, collinear, or UV).

$$d\sigma^S = \sum_{\text{dipoles}} d\sigma^B \otimes dV_{\text{dip}}, \quad (4.7)$$

$$\int_{\Phi_{m+1}} d\sigma^S = \sum_{\text{dipoles}} \int_{\Phi_m} d\sigma^B \otimes \int_{\Phi_1} dV_{\text{dip}} =: \int_{\Phi_m} d\sigma^B \otimes \mathbf{I} \quad (4.8)$$

760 allows one to compute the cross-section  $\sigma^{\text{NLO}}$  of any process:

$$\int_{\Phi_m} d\sigma^B + \int_{\Phi_m} (d\sigma^V + d\sigma^B \otimes \mathbf{I})|_{\epsilon=0} + \int_{\Phi_{m+1}} \left( d\sigma^R|_{\epsilon=0} - \sum_{\text{dipoles}} d\sigma^B \otimes dV_{\text{dip}}|_{\epsilon=0} \right) \quad (4.9)$$

761 with  $\mathbf{I}$  the integrated CS insertion operator. The universal dipole factors are obtained  
 762 by considering the soft/collinear limits of a one-emission matrix-element with respect to  
 763 the Born configuration:

$$|\mathcal{M}_{m+1}|^2 = \sum_{k \neq i,j} \mathcal{D}_{ij,k}(p_1, \dots, p_{m+1}) + (\text{regular in } p_i \cdot p_j \rightarrow 0) \quad (4.10)$$

$$= - \sum_{k \neq i,j} \frac{1}{2p_i \cdot p_j} \mathcal{M}_m^\dagger(i, j \rightarrow \tilde{i}\tilde{j}, \tilde{k}) \left( \frac{\mathbf{T}_k \cdot \mathbf{T}_{ij}}{\mathbf{T}_{ij}^2} \mathbf{V}_{ij,k} \right) \mathcal{M}_m(i, j \rightarrow \tilde{i}\tilde{j}, \tilde{k}) \\ + (\text{regular in } p_i \cdot p_j \rightarrow 0) \quad (4.11)$$

764 where the singular terms are collected in the dipoles  $D_{ij,k}$ . The  $\mathbf{T}_i$  are the generators of  
 765 the colour algebra and  $\mathcal{M}_m$  is a general matrix-element corresponding to an  $m$ -particle  
 766 final-state,  $\mathcal{M}_m = |1, \dots, m\rangle$ . Then Eq. (4.11) states that the matrix-element corre-  
 767 sponding to an  $(m+1)$ -particle final-state factorizes into dipole factors  $\mathbf{V}_{ij,k}$  convo-  
 768 luted with an underlying Born configuration where partons  $i$  and  $j$  are assembled into  
 769 one parton  $(\tilde{i}\tilde{j})$  (the so-called *emitter*), and parton  $\tilde{k}$  (the *spectator*) absorbs the residual  
 770 4-momentum. The formulae for the universal dipoles  $\mathbf{V}_{ij,k}$  are very closely related to  
 771 the Altarelli-Parisi splitting functions, see Section 4.2.

772 In the case of the presence of initial-state hadrons like at the LHC, Eq. (4.11) is  
 773 modified and an additional dipole term has to be added in Eq. (4.8),  $dV_{\text{dip}} \rightarrow dV_{\text{dip}} +$   
 774  $dV'_{\text{dip}}$ . Eq. (4.8) then becomes

$$\int_{\Phi_{m+1}} d\sigma^S = \int_{\Phi_m} d\sigma^B \otimes \mathbf{I} + \int_0^1 dx \int_{\Phi_m} d\sigma_B(xp) \otimes (\mathbf{P} + \mathbf{K})(x), \quad (4.12)$$

775 where  $xp$  is the proton momentum fraction carried away from the hadron, and  $\mathbf{P}, \mathbf{K}$   
 776 are insertion operators appearing from the convolution with the PDF.

## 4.2 Parton-shower models

### 4.2.1 Altarelli-Parisi splitting functions

Inherently, the few-parton, high-energy final-state generated by the hard process matrix-element further produces both QCD and QED radiation. The parton-shower algorithm evolves partons from the collision scale  $Q^2$ , letting them radiate new partons (and photons), to a cutoff scale  $Q_{\min}^2$  that is set around the hadronization scale. At that point, the shower terminates and the final-state is passed on to the hadronization model. Schematically, the simplest shower algorithms are based on the so-called Dokshitzer-Gribov-Lipatov-Altarelli-Parisi (DGLAP) kernels [76–78] for  $1 \rightarrow 2$  collinear particle splitting  $P_{a \rightarrow bc}$ , as given in Fig. 4.3.

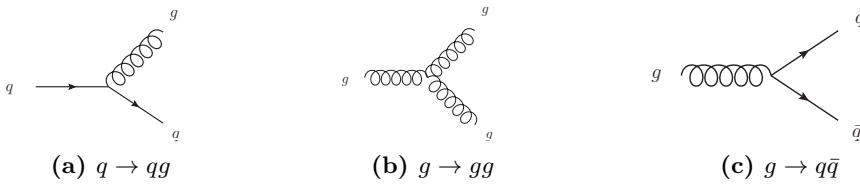


**Figure 4.3:** The QCD vertices for  $1 \rightarrow 2$  splittings allow to calculate the leading-order kernels appearing in the DGLAP evolution equation.

The (unregularized) LO kernels can be computed from the QCD interaction vertices as:

$$P_{q \rightarrow qg}(z) = C_F \frac{1+z^2}{1-z}, \quad (4.13)$$

$$P_{g \rightarrow gg}(z) = 2C_A \left( \frac{1-z}{z} + z(1-z) + \frac{z}{1-z} \right), \quad (4.14)$$

$$P_{g \rightarrow q\bar{q}}(z) = T_R(1 - 2z(1-z)). \quad (4.15)$$

with  $z$ ,  $0 \leq z \leq 1$ , the longitudinal momentum fraction of the parent parton  $a$ . Notice the undefined behavior of  $P_{q \rightarrow qg}$  and  $P_{g \rightarrow gg}$  for  $z = 1$ : the splitting functions can be regularized from general constraints to:

$$P_{q \rightarrow qg}(z) = C_F \left( \frac{1+z^2}{(1-z)_+} + \frac{3}{2} \delta(z-1) \right), \quad (4.16)$$

$$P_{g \rightarrow gg}(z) = 2C_A \left( \frac{1-z}{z} + z(1-z) + \frac{z}{(1-z)_+} + \left( \frac{11}{12} - \frac{1}{3} \frac{T_R}{C_A} \right) \delta(z-1) \right), \quad (4.17)$$

$$P_{g \rightarrow q\bar{q}}(z) = T_R(1 - 2z(1-z)). \quad (4.18)$$

The factor  $(1-z)^{-1}$  is regularized in being interpreted as a plus-distribution  $(1-z)_+^{-1}$  such that for any test function  $f(z)$  sufficiently regular at  $z = 0, z = 1$ ,

$$\int_0^1 \frac{dz f(z)}{(1-z)_+} = \int_0^1 \frac{f(z) - f(1)}{1-z} . \quad (4.19)$$

794     The master equation governing the evolution of the collinear splitting of a parton  $a$   
 795     from a scale  $q^2$  to a scale  $q^2 + dq^2$  is then given by

$$dP_{a \rightarrow bc} = \frac{dq^2}{q^2} \frac{\alpha_s}{2\pi} P_{a \rightarrow bc}(z) dz , \quad (4.20)$$

796     where  $q^2$  is an arbitrary strong-ordered evolution variable. It can be the azimuthal  
 797     angle of emission  $E_a^2 \theta^2$ , or the particle's virtuality  $m^2$ , or the transverse momentum  
 798      $p_T^2$ . Different shower algorithms implement different choices of the evolution variable.  
 799     This will be of importance when considering parton-shower related uncertainties, see  
 800     Chapters 7 and 11.

### 801     4.2.2 The Sudakov form factor

802     Going from the one-emission to the multiple-emission case, and using broad assump-  
 803     tions<sup>2</sup>, the probability of no-emission between scales  $Q^2$  and  $Q_{\max}^2$  is given by the *Sudakov*  
 804     form factor:

$$dP_{a \rightarrow bc}(z) = \frac{dq^2}{q^2} \frac{\alpha_s}{2\pi} P_{a \rightarrow bc}(z) dz \times \exp \left( - \sum_b \int_{Q^2}^{Q_{\max}^2} \frac{dq'^2}{q'^2} \int \frac{\alpha_s}{2\pi} P_{a \rightarrow bc}(z') dz' \right) . \quad (4.21)$$

805     As explained in Sec. 3.1.3, the perturbative expansion of the cross-section in  $\alpha_s$  can  
 806     suffer from large enhancements in the soft/collinear regions of phase-space. In general,  
 807     double logarithms of the form  $\alpha_s^n \log^{2n}(Q^2/q^2)$  appear when a soft particle is emitted, or  
 808     when it becomes collinear to one of the incoming partons. Here,  $q^2$  is the scale describing  
 809     the soft/collinear emission, and  $Q^2$  is the global scale of the process. Generally, this tower  
 810     of large logarithms can be analytically resummed to all orders in  $\alpha_s$ . Instead, the parton  
 811     shower algorithm offers the possibility of resumming soft and collinear contributions  
 812     within the Monte-Carlo framework. Nowadays, most parton showers only guarantee  
 813     leading-logarithmic (LL) accuracy, although recent studies [79] have found differences at  
 814     LL (subleading number of colors  $N_C$ ), and NLL (leading- $N_C$ ) between parton-showers  
 815     and analytic resummations.

### 816     4.2.3 Parton-shower matching

817     The shower algorithm should respect the theoretical accuracy of the hard matrix-element,  
 818     and at the same time conserve the logarithmic accuracy of the parton-shower resumma-  
 819     tion in their respective limits. In particular, the cross-section after showering should

---

<sup>2</sup>Namely that the time between emissions can be sliced, and unitarity as well as multiplicativity (meaning the shower has no memory of past emissions) hold.

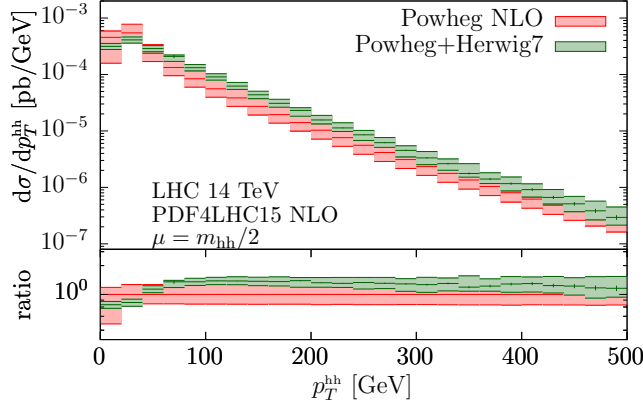


**Figure 4.4:** The transverse momentum  $p_T^{hh}$  in di-Higgs production is compared for the fixed-order NLO prediction to a parton-shower matched calculation. The parton-shower correctly reproduces the NLO computation at high-transverse momentum and softens the low-momentum region (Sudakov suppression).

be identical to the fixed-order cross-section. Also, kinematic configurations that belong both to the hard matrix-element and the parton-shower final-states should not be double-counted. This whole procedure is called *matching*. At NLO, the matching of the parton-shower algorithm to the fixed-order matrix-element handles both these issues. Roughly said, it interpolates between the two kinematic regions where the hard matrix-element, respectively the parton-shower, generate their respective dominant contributions. An illustration of this fact is shown in Fig. 4.4 for the case of  $gg \rightarrow hh$  production, where a fixed-order NLO calculation is matched to the **Herwig 7** [80, 81] parton-shower. Among the various matching procedures that keep in line with the above criteria, the subtractive MC@NLO [82] and the multiplicative POWHEG [83] schemes are among the most used ones.

As examples of available parton-shower algorithms mostly used by the physics community, the **Pythia 8** [84, 85] and **Herwig 7** codes implement a  $p_T$ -ordering, respectively an angular-ordering in the choice of the evolution variable. **Herwig** also uses a dipole shower as an alternative algorithm (which is based on a Catani-Seymour dipole formulation of  $2 \rightarrow 3$  splitting kernels). The **Sherpa** [86] generator implements two alternative parton-shower algorithms based on variations of the CS dipoles.

### 4.3 Hadronization

Once particles have been showered down to the hadronization scale, the hadronization model takes over. By far, the two most used hadronization models are the Lund string model and the cluster model.

841 **4.3.1 Lund string model**

842 The Lund string model [87] bases on the principle of quark color confinement. When  
 843 two quarks with electric charges  $q_1, q_2$  are separated by a distance  $r$ , the potential takes  
 844 the form:

$$U(r) = -\frac{q_1 q_2}{r} + \kappa r, \quad (4.22)$$

845 and the linear confinement contribution dominates for larger distances, with  $\kappa \sim$   
 846 1 GeV/fm. In analogy to a classical elastic potential, the field lines build up a stretched  
 847 *string*. When the distance between a quark-pair increases, the string tension grows  
 848 until the string breaks: the freed energy creates another quark-antiquark pair appearing  
 849 from the vacuum. The creation of the quark-pair happens with a Gaussian probability  
 850 (similarly to quantum tunnelling) in the quark transverse mass  $m_T^2$ . From Lorentz  
 851 invariance, causality and left-right symmetry, the fragmentation function  $f(z)$  can be  
 852 constrained and fixes the longitudinal momentum fraction  $z$  carried away by the created  
 853 hadron:

$$\mathcal{P} \propto \exp\left(-\frac{\sigma m_T^2}{\kappa}\right), \quad f(z) \propto \frac{(1-z)^a}{z} \exp\left(-\frac{bm_T^2}{z}\right). \quad (4.23)$$

854 The Lund string model is implemented in the **Pythia 8** generator and the main pa-  
 855 rameters  $a, b, \sigma$  are determined by tuning to data. For the more complex case of baryons,  
 856 the three quarks can be pictured in a quark-diquark frame. Finally, the gluons appear  
 857 as kinks on strings. For more details and improvements to the model, see the **Pythia**  
 858 manual [88].

859 **4.3.2 Cluster model**

860 Instead of building on color confinement, the cluster model [89, 90] makes the assumption  
 861 that gluons can be viewed as carrying color and anticolor and behaving as a  $q\bar{q}$  pair.  
 862 Color singlets usually obey a mass spectrum that peaks at low mass due to the property  
 863 of preconfinement of the parton shower [91], i.e. they are closer to one another in phase-  
 864 space. The model then clusters these color singlets together and splits them per the  
 865 following procedure: if a cluster of mass  $M$ , with parton constituents of masses  $m_1, m_2$ ,  
 866 satisfies

$$M^{C_{\text{pow}}} > C_{\text{max}}^{C_{\text{pow}}} + (m_1 + m_2)^{C_{\text{pow}}}, \quad (4.24)$$

867 the algorithm splits it and the masses get redistributed. To split a cluster, the model  
 868 pops a  $q\bar{q}$  pair from vacuum and forms two new clusters with one original parton each,  
 869 and masses distributed according to

$$M_{1,2} = m_{1,2} + (M - m_{1,2} - m_q)\mathcal{R}_{1,2}^{P_{\text{split}}}, \quad (4.25)$$

870 with  $\mathcal{R}_{1,2} \in [0, 1]$  two random numbers. Again, the parameters  $C_{\text{pow}}$ ,  $C_{\text{max}}$  and  $P_{\text{split}}$   
 871 have to be tuned to data.

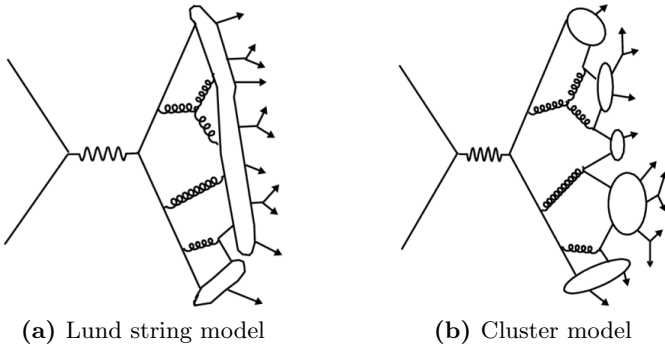


**Figure 4.5:** A pictorial representation of both hadronization models. (a) In the Lund model, the potential energy from the color field between two quarks increases linearly with the distance, like in a string. When a string breaks, a new quark-antiquark pair is created. (b) The **Herwig** model groups color-connected partons together into clusters and lets them decay isotropically.

Notice that the cluster model does not propagate any spin information: the hadronized clusters therefore decay isotropically. Historically, the cluster model was implemented in the **Herwig** event generator. Fig. 4.5 summarizes the conceptual differences between the Lund string and the cluster model.

As a concluding remark, the MC event generators represent the basis of a large fraction of experimental measurements. They are quite complex systems whose constituents are all inter-correlated: the different pieces interact and the matching between all appearing physical scales is not always explicit at the end of the simulation. Typically, the parton-shower output influences the hadronization tune, and it is in general difficult to disentangle their respective contributions. As such, variations in the MC setup are linked to large uncertainties which should, in principle, be taken into account with their full correlations.



## 884 5 The LHC and the ATLAS detector

885 The Large Hadron Collider, or LHC, is currently the most powerful particle accelerator  
886 worldwide and is located at the Centre Européen pour la Recherche Nucléaire (CERN)  
887 on the French-Swiss border, near Geneva. Historically, it replaced the Large Electron-  
888 Positron (LEP) collider after it was decommissioned in 2000, and is being housed in  
889 the same tunnel. In this Chapter, we shall briefly review the main working parts of  
890 the accelerator complex, and then dive in more detail into the structure of the ATLAS  
891 detector. A short overview of the trigger system and data acquisition will close the  
892 subject.

### 893 5.1 The Large Hadron Collider

894 The LHC's main collider ring is installed in a circular tunnel of  $\sim 27$  km circumference  
895 and a depth varying between 45 m and 170 m under ground level. It is designed to  
896 accelerate protons to a design center-of-mass energy of 14 TeV at a peak luminosity  
897 of  $10^{34} \text{ cm}^{-2} \text{ s}^{-1}$ . As a side note, the LHC also collides heavy ions, and in the past a  
898 few runs of lead-lead, proton-lead and xenon-xenon collisions have also given interesting  
899 complementary physics results.

900 To accelerate protons to the design center-of-mass energy, a sequence of pre-accelerators  
901 boosts the proton beams before injecting them into the next link. A schematic of the full  
902 accelerator complex is presented in Fig. 5.1. Upon being produced and pre-collimated,  
903 the protons are accelerated to 50 MeV in the Linac2, then to 1.4 GeV in the PS Booster,  
904 to 26 GeV in the Proton Synchrotron (PS). Within the PS, the protons are collimated  
905 into 25 ns-spaced (7.5 m) bunches of around  $1.15 \cdot 10^{11}$  protons per bunch. From there,  
906 the Super Proton Synchrotron ramps up the energy to 450 GeV, and injects both beams  
907 in opposite directions into the LHC itself. After approximately 20 minutes of acceleration  
908 in the main LHC beampipe by 16 radiofrequency (RF) cavities, the proton bunches  
909 achieve the current energy of 6.5 TeV per beam. From the start of Run II in 2015 until  
910 the Long Shutdown of December 2018, the LHC delivered a total integrated luminosity  
911 of around  $150 \text{ fb}^{-1}$  at a center-of-mass energy of 13 TeV and a peak luminosity of  
912  $2.1 \cdot 10^{34} \text{ cm}^{-2} \text{ s}^{-1}$ , even surpassing the design value.

913 Equipped with 1232 superconducting main dipole magnets, the LHC operates with  
914 magnetic fields of  $\sim 8.3$  T to keep the proton bunches on their circular trajectory.  
915 The main dipoles are supplemented by higher-multipole magnets to correct for edge  
916 imperfections in the dipole field. Along the LHC lattice, 392 main quadrupole magnets  
917 are used to re-focus the proton beams.

918 Once at the nominal energy, the two circulating proton beams are made to collide  
919 at four different interaction points, corresponding to the four biggest LHC experiments:

## 5 The LHC and the ATLAS detector

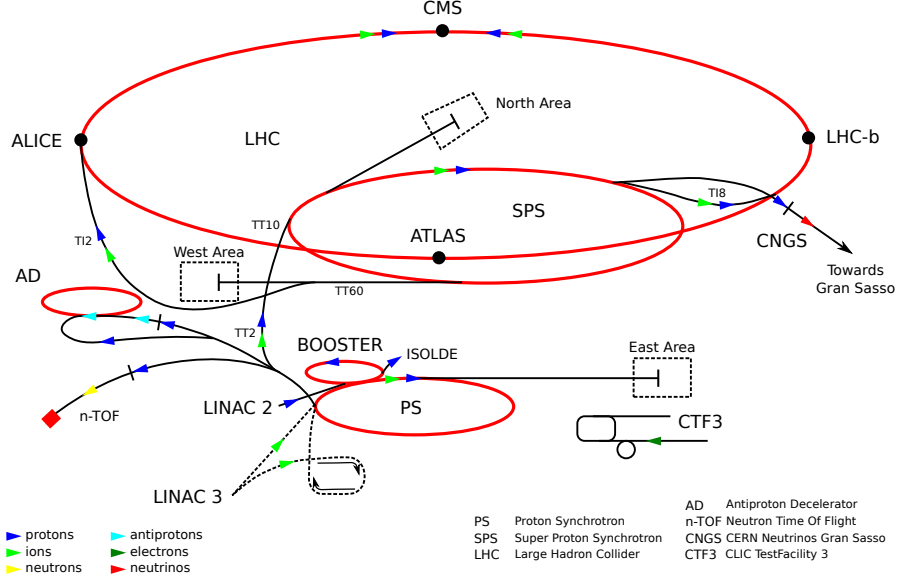


**Figure 5.1:** The LHC accelerator complex.

ATLAS, CMS, ALICE and LHCb. Out of these, ATLAS and CMS are general-purpose detectors designed to discover higher-mass particles like the Higgs boson or possible supersymmetric resonances, as well as to produce high-precision measurements of particles like the top-quark, whose properties were poorly resolved in earlier experiments. ALICE and LHCb, on the other hand, are dedicated to studies of heavy-ion collisions and focus on high-density QCD bound states and flavor physics. In the next Section, we will concentrate on the ATLAS detector substructure.

## 5.2 The ATLAS detector

A Toroidal LHC ApparatuS (ATLAS) aims for high-energy precision measurements of the SM in all possible sectors: with the help of the enormous statistics produced at LHC and the precision of the detector tracker and calorimeters, it allows for measurements of particle masses and couplings (from the CKM matrix to the Higgs boson coupling to other particles,  $\alpha_s$  measurements and PDF fits) or cross-section measurements, but also the observation of rare SM processes and decay channels (like  $t\bar{t}h$  production, light-by-light scattering or  $B^0 \rightarrow \mu^+\mu^-$  decays). These high-precision tests of the SM are intrinsically linked to searches for Beyond the SM (BSM) physics: higher-scale BSM particles participating in loop corrections to the SM can have an important impact on the cross-sections or kinematic observables, and any observed deviation would hint at New Physics not far from the TeV scale. In general, though, direct searches are employed to discover potential high-mass resonances.

The ATLAS detector, situated at the LHC beam interaction point 1 near Meyrin, Switzerland, is an onion-shell structure comprised of particle trackers, an electromagnetic

and hadronic calorimeter, and a muon detector: from inner to outer radii, the produced particles encounter the Inner Detector, the Liquid Argon and the Tile Calorimeter, and finally the Muon Spectrometer. The detector itself is 44 m long and has a diameter of 25 m, and weighs more than 7000 tons. Fig. 5.2 shows a rendering of the ATLAS detector. To bend the charged-particle tracks for momentum measurement, ATLAS relies on four magnets: a 2 T central solenoid close to the interaction point, an 8-coil barrel toroid that is cylindrically placed around the detector generating a magnetic field of 8 T, and two other 8-coil toroid magnets at the detector endcaps. The geometry of the magnet coils is shown in Fig. 5.3.

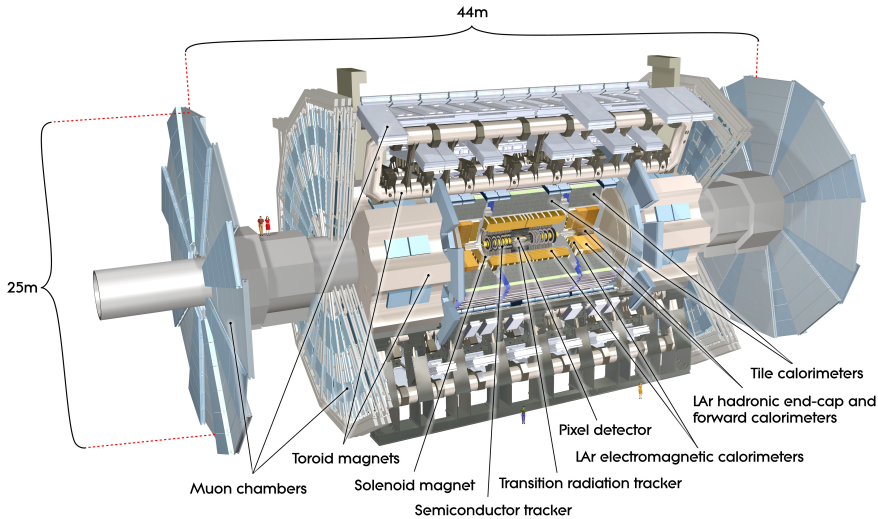


**Figure 5.2:** A cut-away view of the ATLAS detector.

By definition, the coordinate system is right-handed and centered at the interaction point, with the beam axis chosen as the  $z$ -axis, and the  $x$ -axis pointing towards the center of the LHC ring. The transverse plane is thus the  $(x, y)$ -plane.

### 5.2.1 The Inner Detector

Being the piece of equipment closer to the beampipe, the Inner Detector (ID) must fulfill several criteria for the reconstruction of charged-particles four-momenta, as well as for the identification of secondary vertices due to the decay of bottom-flavored particles and the measurement of the impact parameter. The ID is further divided into a Silicon Pixel Detector (SPD), a Semiconductor Tracker (SCT) and a Transition Radiation Tracker (TRT). In Fig. 5.4, the structure of the ID is presented in a cut view along the beampipe (with the notable absence of the new insertable  $B$ -layer).

The SPD has a total of  $86 \cdot 10^6$  channels and is the element closest to the interaction point. Four concentric layers of silicon pixel detectors are laid out around the beam axis in so-called barrel layers. The innermost layer is called the insertable  $B$ -layer (IBL) and was installed during the first Long Shutdown. It is only 3.3 cm away from the

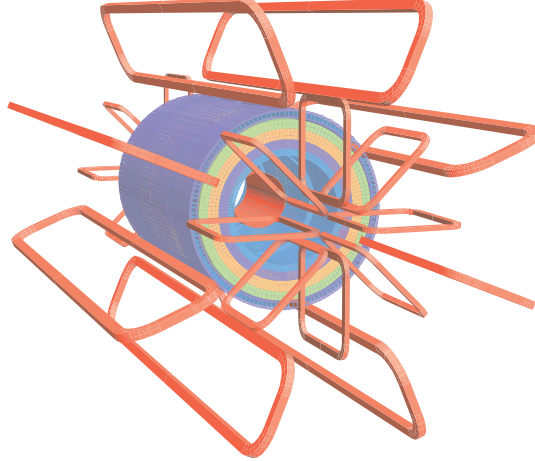


**Figure 5.3:** The geometry of the coils used to produce the magnetic field in the ATLAS detector. A solenoid magnet (4 T) is installed cylindrically around the beampipe, surrounded by a toroid magnet (8 T) and two endcap toroid magnets.

interaction point and allows for precise measurements of secondary vertex positions, and was designed to work in a high-radiation environment. Three other layers (including the earlier  $B$ -layer) are disposed concentrically around the beampipe, while three pixel disks are mounted on each endcap. All in all, the barrel layer and endcap disks have a resolution of  $12 \mu\text{m} \times 87 \mu\text{m}$ , respectively  $13 \mu\text{m} \times 78 \mu\text{m}$  in the transverse-, respectively longitudinal- ( $T, L$ ) directions.

At intermediate radius, the SCT is a silicon microstrip tracker and provides, out of  $6.2 \cdot 10^6$  readout channels, a measurement of the  $(\phi, r, z)$  track points. Four SCT barrel layers are disposed at radii between 299 mm and 514 mm away from the beampipe, while 18 more planar discs are placed at the endcaps. The barrel modules have a resolution of  $15 \mu\text{m} \times 530 \mu\text{m}$ .

Finally, at the outer layer, the TRTs are made of thin-walled straw tubes and give information for distinguishing between electrons and pions, as well as contribute to the transverse position measurement for a total of  $350 \cdot 10^3$  readout channels. A straw tube is a 4 mm-diameter cylinder filled with gaseous xenon and a gold-plated tungsten wire strung through the center. With the inner tube wall (cathode) and the wire (anode) held at 1.5kV of voltage difference, a charged particle passing through ionizes the gas, and the freed electrons drift to the wire: the drift time can then be used to determine the distance from the anode. Moreover, electron identification succeeds by transition-radiation photons created between the straws and converted in the xenon gas. The probability of transition radiation is proportional to the relativistic factor  $\gamma$ , which is usually higher for electrons and positrons. The TRTs determine the transverse position at a resolution of  $\sim 100 \mu\text{m}$ .

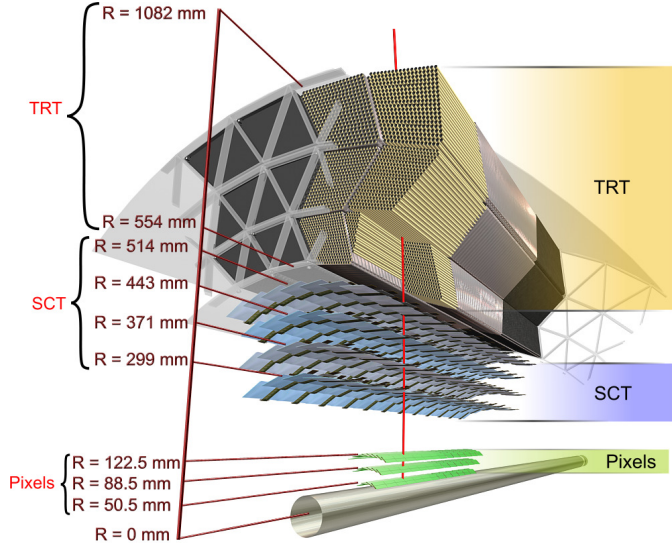


**Figure 5.4:** In order of increasing distance to the beampipe, the Inner Detector particle tracker is made up of the Silicon Pixel Detector, the microstrip Semiconductor Tracker (SCT), and the Transition Radiation Tracker (TRT).

### 5.2.2 The Liquid Argon (LAr) Calorimeter

Both the electromagnetic (EM) and the hadronic calorimeters are found between the ID and the muon spectrometer. Fig. 5.5 depicts the LAr calorimeter in yellow, which is closest to the ID and enveloped by the Tile Calorimeter (see Section 5.2.3). The calorimeters mainly measure the energy deposited by the corresponding particle type, but they also contribute to position measurements and particle identification (as well as to the measurement of the missing transverse energy). The LAr calorimeter contains both EM and hadronic detectors. In principle, a passing electron or photon produces an electromagnetic shower in the EM calorimeter mainly through brehmsstrahlung and electron-positron pair creation. In comparison, hadrons generate further hadronic activity by primary nuclear reactions and spallation, as well as EM showers when the produced particles decay electromagnetically. The LAr calorimeter functions as a system of alternating lead/stainless steel absorbers and electrodes measuring the signal drift-time, with the whole system immersed in liquid argon which plays the role of a scintillator.

The electromagnetic barrel (EMB,  $|\eta| < 1.475$ ) and endcap (EMEC,  $1.375 < |\eta| < 3.2$ ) calorimeters use the same absorber material and geometry. In the forward region (FCal) at rapidities  $3.1 < |\eta| < 4.9$ , a copper-based absorber covers EM activity while a tungsten module provides measurement of hadronic energy deposition. Finally, a hadronic LAr calorimeter is also placed at the endcaps (HEC) and should complement readings from the Tile Calorimeter.

1010 **5.2.3 The Tile Calorimeter (TileCal)**

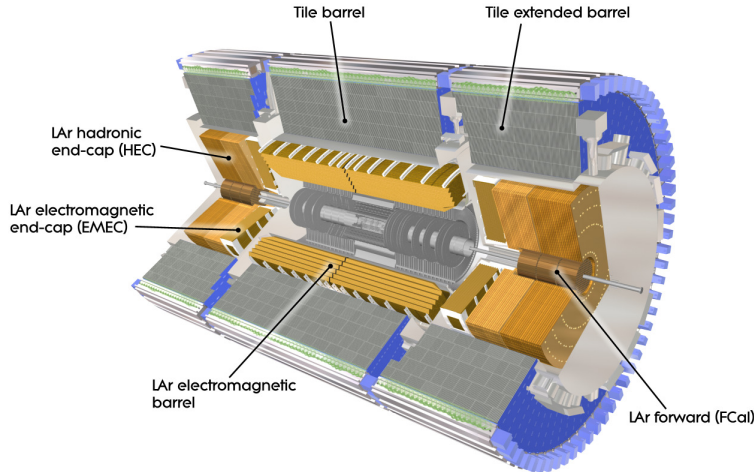


**Figure 5.5:** The ATLAS calorimetry system is composed of the inner Liquid Argon calorimeter (yellow) and the outer Tile Calorimeter (gray).

1011 The central and two extended barrel regions are covered by the TileCal, which is  
1012 cylindrically disposed around the beampipe (see Fig. 5.5) and is made of iron plate  
1013 absorbers and plastic scintillators as the active medium. The scintillating light created  
1014 by hadronic energy deposition is wavelength-shifted and led to photomultiplier tubes  
1015 that amplify the signal.

1016 **5.2.4 The Muon Spectrometer**

1017 At the outmost layer of the ATLAS detector, the Muon Spectrometer (MS) is designed to  
1018 deliver high-precision measurements of the muons' transverse momentum. It uses four  
1019 different techniques to trigger and detect the produced muons: resistive-plate cham-  
1020 bers (RPC), cathode strip chambers (CSC), monitored drift tubes (MDT) and thin-gap  
1021 chambers (TGC), shown in Fig. 5.6. The muons are bent by three toroid magnets  
1022 which contain the detectors, for a rapidity-dependent magnetic field of 0.3 – 1.2 T which  
1023 amounts to a resolution of  $\sim 10\%$  in the transverse momentum of high-energy muons at  
1024 around 1 TeV. Both the RPCs and the TGCs are used as a first-level trigger on well-  
1025 resolved, high- $p_T$  muons in the barrel region, respectively the endcaps. On the other  
1026 hand, the MDTs which are laid out in the barrel and endcap regions, and the CSCs in  
1027 the forward region, measure the position of the incoming muons in the bending plane.

1028 **5.2.5 Trigger & Data acquisition**

1029 The collision data rate at high-energy collider experiments like ATLAS poses enormous  
1030 computing and storage problems. At LHC, the proton bunch crossing rate at the current  
1031 luminosity towers at a vertiginous 40 MHz. With a data content of  $\sim 1.6$  MB per event,

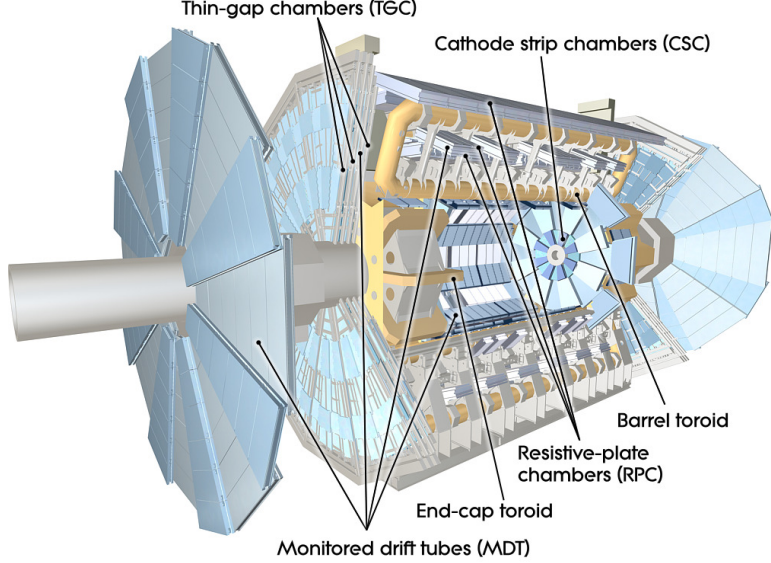


**Figure 5.6:** The ATLAS muon spectrometer.

1032 the storage of all events would produce an impossible  $\sim 60$  TB per second. Thus the  
 1033 event rate needs to be reduced to an affordable storage and readout rate. The ATLAS  
 1034 trigger and data acquisition system [92, 93] lowers the stored event rate using certain  
 1035 quality criteria from the detectors. The trigger system is organized in three sublevels:

- 1036 • **Level 1:** The first layer triggers at the hardware level already, and uses both  
 1037 calorimetry information (cluster energy sum and isolation criteria) and data from  
 1038 the muon trigger chambers ( $high-p_T$ ) to reduce the event rate from 40 MHz to  
 1039  $\sim 75$  kHz.
- 1040 • **Level 2:** At the software level, the Level 2 Trigger uses regions-of-interest identified  
 1041 by Level 1 and combines information from all subdetectors to focus on the physics  
 1042 objects. The event rate is then reduced from 75 kHz to  $\sim 1 - 3$  kHz.
- 1043 • **Event Filter:** The full event data is analyzed online and the Level 2 selection  
 1044 is refined by the Event Filter, which can also perform full event reconstruction at  
 1045 this stage. Accepted events are then stored permanently on disk at a rate of  $\sim 200$   
 1046 Hz for an acceptable total storage rate of around 300 MB per second.

1047 The raw data is stored first in the central CERN data center. These sites make up  
 1048 the so-called Tier-0 system. It is then redistributed to other storage and analysis sites  
 1049 called Tier-1, Tier-2 and Tier-3 in refined formats that prune away information that is  
 1050 not needed by the final analyses.



1051

## **Part II**

1052

# **Top-Quark Mass Determinations**



## 6 Theoretical predictions for $t\bar{t}$ final-states

The top-quark pairs created e.g. at the LHC are not observable *per se*. The only directly measurable quantities are the kinematic properties of the decayed final-states. Fortunately, the top-quark has a branching ratio of 99.8% for  $t \rightarrow W^+ b$ ,  $\bar{t} \rightarrow W^- \bar{b}$ . So, the final-state contains two  $b$ -jets that can be experimentally tagged, and depends only on the decay mode of the  $W$ -bosons. In the case of top-quark pair production, both  $W$ -bosons can decay either hadronically or leptonically, with branching ratios  $\Gamma(W \rightarrow q\bar{q}') = 0.67$ ,  $\Gamma(W \rightarrow \ell\nu_\ell) = 0.33$ : so the final-state can either be dileptonic, monoleptonic (lepton+jets) or all-hadronic, and the top-quark properties must then be reconstructed from the measured final-states. Fig. 6.1 depicts the topology of the three decay channels and Table 6.1 gives an overview of their respective cross-sections, advantages and disadvantages.

A precise computation for top-quark pair production cross-section and differential observables is of paramount importance for the extraction of top-quark properties. Most theoretical systematic uncertainties are well under control and have been the subject of various studies in the last few years [103–106]. In this Chapter, we first review the different theoretical descriptions of  $pp \rightarrow t\bar{t}$  production, summarize the most important issues and discuss their potential impact on the extraction of top-quark properties from data, with a special focus on the top-quark observables. To do so in a realistic and quantitative way, we setup an analysis close to the ATLAS 8 TeV top-quark mass extraction in the dilepton channel. The dilepton channel is the cleanest decay mode for an experimental measurement of the top-quark mass. It has the advantage of having a small background (coming mainly from fake leptons, diboson and  $Z$ +jets production)

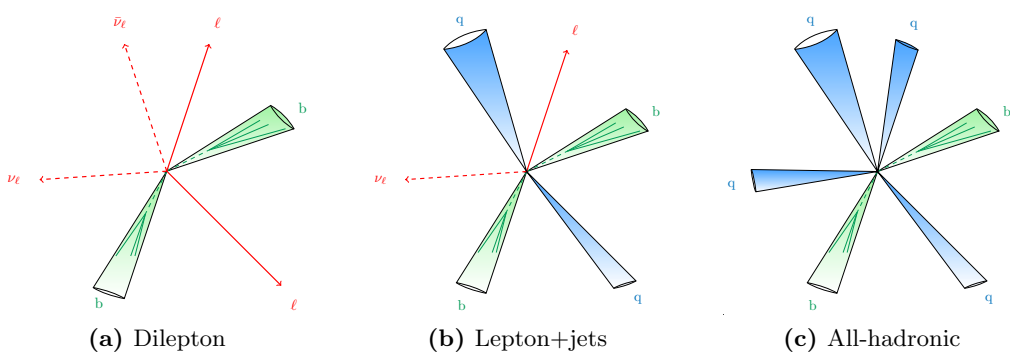


**Figure 6.1:** Topologies for  $t\bar{t}$  events are either stemming from (a) dileptonic, (b) monoleptonic or (c) all-hadronic decays.

## 6 Theoretical predictions for $t\bar{t}$ final-states

Final-state $X$	dilepton (w. $\tau^+\tau^-$ )	$\ell+$ jets (w. $\tau+j$ )	all-hadronic	all channels
$\Gamma(t\bar{t} \rightarrow X) [\%]$	10.89	44.02	44.89	100.0
$\sigma_{\text{NNLO}} [\text{pb}]$	90.58	366.14	373.38	$831.76^{+2.37\%}_{-3.51\%}$
Advantages	Clean signature	Full reconstruction	Largest branching	
Drawbacks	No full reconstruction	Jet-scale uncertainties	QCD background	
References	[94–96],[97, 98]	[95, 99],[5]	[100],[101]	

**Table 6.1:** For the three decay channels in  $t\bar{t}$  production, the branching ratios and inclusive theoretical cross-sections at QCD NNLO were computed with the Top++ program [102] for a top-quark mass  $m_t = 172.5$  GeV. Advantages and drawbacks of (any) top-quark measurement in said channel are given. References for ATLAS measurements of the top-quark mass in particular are also laid out for each subchannel for the top-quark pole mass (in black), and for the MC mass (in blue) from template fits.

and a clean signature, but suffers from the small branching fraction ( $\Gamma \sim 4.8\%$  for  $e/\mu$  in the final-state). Cross-sections for all considered theoretical descriptions of  $t\bar{t}$  final-states are given at the end of the Chapter for the fiducial cuts employed in our analysis.

### 6.1 The narrow-width approximation

If we consider the intermediate state  $W^+W^-b\bar{b}$ , it makes sense at first to approximate it and examine only on-shell, doubly-resonant top-quark diagrams: the cross-section contribution stemming from non-resonant diagrams is expected to be of the order of  $\mathcal{O}(\Gamma_t/m_t) \leq 1\%$ , and usually neglecting other contributions is fine. This description is called the *narrow-width approximation* (NWA), and it builds on the limit  $\Gamma_t \rightarrow 0$ , where the top-quark propagator can then be written as

$$\lim_{\Gamma_t \rightarrow 0} \frac{1}{(p^2 - m_t^2) + m_t^2 \Gamma_t^2} = \frac{\pi}{m_t \Gamma_t} \delta(p^2 - m_t^2) + \mathcal{O}\left(\frac{\Gamma_t}{m_t}\right). \quad (6.1)$$

That is, top-quark production and decay entirely factorize, i.e.:

$$\mathcal{M}_{pp \rightarrow W^+W^-b\bar{b}} = \mathcal{M}_{pp \rightarrow t\bar{t} \rightarrow W^+W^-b\bar{b}}^{\text{NWA}} + \mathcal{O}(\Gamma_t/m_t) \quad (6.2)$$

$$= \mathcal{P}_{pp \rightarrow t\bar{t}} \otimes \mathcal{D}_{t \rightarrow W^+b} \otimes \mathcal{D}_{\bar{t} \rightarrow W^-\bar{b}} + \mathcal{O}(\Gamma_t/m_t), \quad (6.3)$$

where  $\mathcal{P}$  denotes the  $t\bar{t}$  production and  $\mathcal{D}$  the top-quark decay dynamics, and the spin correlations are correctly taken into account as indicated by the symbol  $\otimes$ . The corresponding three LO Feynman diagrams, as well as a few examples of one-loop diagrams for  $gg \rightarrow t\bar{t}$  production, are shown in Fig. 6.2. Nowadays, most of the theoretical predictions used for the extraction of top-quark properties in experimental analyses rely on NLO matrix-elements for top-quark pair production. The top-quark decay and all subsequent radiation is left to the MC generator, with the approximations it entails: particle decay usually only has LO accuracy, spin correlations (in particular in the parton-shower)

## 6.1 The narrow-width approximation

were only recently implemented, and resummation is as good as the shower algorithm's accuracy. Even so, there exists a number of more complete MC implementations for  $t\bar{t}$  production in the NWA: the effects of NLO corrections to both production and decay were investigated in the POWHEG-BOX-v2 [17–19] framework called `ttb_NLO_dec` [107]. The `Herwig 7.1` MC generator supports a new multijet merging algorithm adapted to  $t\bar{t}$  production at NLO, and finally the `SHERPA` generator allows for the matching of the CS shower to  $t\bar{t}$  production with 1-, 2- and 3-jets at NLO.

Furthermore, some dedicated calculations have appeared over the years. In particular, QCD NNLO corrections for  $t\bar{t}$  production have been calculated for differential distributions [108–110], and combined with NLO EW corrections [111]. For a review of NLO EW effects, see Refs. [112–114]. Leaving corrections in top-quark pair production and considering now the top-quark decay, it was later shown that higher-order corrections to the top-quark decay have a measurable impact on differential distributions in certain regions of phase-space. NLO radiative corrections to the top-quark decays were computed [115–117] and completed by NNLO QCD corrections [118, 119], NNLL resummation and other improvements above higher-order corrections in  $\alpha_s$  [120–125]. Within the NWA, the calculation of QCD NNLO + NNLL' (soft-gluon and small-mass resummation) corrections for differential distributions was combined with NLO EW corrections and is the most complete fixed-order calculation up-to-date [126].

For the results shown in Section 6.5 in the NWA, the top-quark pair production is described at NLO QCD and factorizes from the top-quark decay. Furthermore, we consider only the  $e\mu$  dilepton channel, that is  $pp \rightarrow (e^+\nu_e)(\mu^-\bar{\nu}_\mu)b\bar{b}$  production for the analysis presented in Chapter 7. The top-quark decay accuracy is handled in three different ways.

- (1) Top-quark decay at LO is realized in the fixed-order `SHERPA` setup, as in Ref. [127] (referred to as **NLO<sub>NWA</sub><sup>LOdec</sup>** from now on).
- (2) The top-quark decay at NLO is computed in Ref. [116], and is shortly described below (**NLO<sub>NWA</sub><sup>NLOdec</sup>**).
- (3) The top-quark decay is handled by the parton-shower, namely through the `SHERPA` CSS shower (**NLO<sub>PS</sub>**).

Briefly, the **NLO<sub>NWA</sub><sup>NLOdec</sup>** calculation in the NWA bases on the following formula where top-quark pair production and decay factorize. Taking the perturbative expansion of Eq. (6.3) to NLO gives

$$\begin{aligned} \mathcal{M}_{ij \rightarrow t\bar{t} \rightarrow b\bar{b}2\ell2\nu}^{\text{NWA, NLO}} = & \mathcal{P}_{ij \rightarrow t\bar{t}}^{\text{LO}} \otimes \mathcal{D}_{t \rightarrow b\ell^+\nu}^{\text{LO}} \otimes \mathcal{D}_{\bar{t} \rightarrow \bar{b}\ell^-\bar{\nu}}^{\text{LO}} + \mathcal{P}_{ij \rightarrow t\bar{t}}^{\delta\text{NLO}} \otimes \mathcal{D}_{t \rightarrow b\ell^+\nu}^{\text{LO}} \otimes \mathcal{D}_{\bar{t} \rightarrow \bar{b}\ell^-\bar{\nu}}^{\text{LO}} \\ & + \mathcal{P}_{ij \rightarrow t\bar{t}}^{\text{LO}} \otimes \left( \mathcal{D}_{t \rightarrow b\ell^+\nu}^{\delta\text{NLO}} \otimes \mathcal{D}_{\bar{t} \rightarrow \bar{b}\ell^-\bar{\nu}}^{\text{LO}} + \mathcal{D}_{t \rightarrow b\ell^+\nu}^{\text{LO}} \otimes \mathcal{D}_{\bar{t} \rightarrow \bar{b}\ell^-\bar{\nu}}^{\delta\text{NLO}} \right). \end{aligned} \quad (6.4)$$

As mentioned above, the NWA is expected to be precise enough for most calculations and yet, NLO and off-shell effects in the top-quark decay can have an important impact on sensitive regions of phase-space. In practice, analyses either include single-top quark

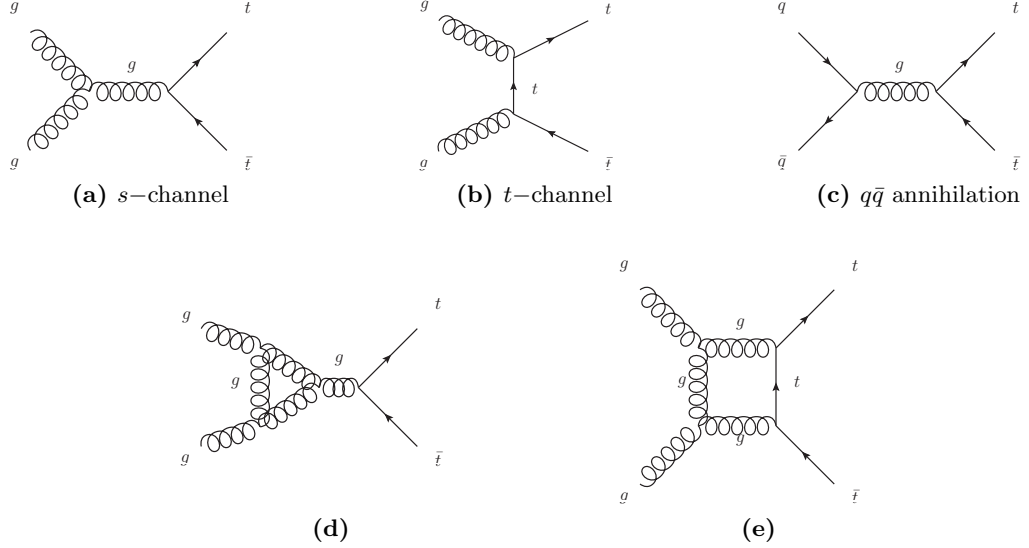


**Figure 6.2:** (a-c) Leading-order diagrams for  $t\bar{t}$  production and (d-e) two examples of NLO QCD one-loop diagrams for  $gg \rightarrow t\bar{t}$

production in the signal, or have to subtract it consistently as background since it contributes to the same final-state at NLO. This is generally accomplished with the help of a diagram subtraction (DS) or diagram removal (DR) scheme [128] to account for the interference between top-quark pair and single-top production. This procedure is not entirely free of quirks and violates gauge-invariance. To get an entirely consistent theoretical prediction, it is therefore preferable to produce the full intermediate state  $pp \rightarrow W^+W^-b\bar{b}$ , which contains the more complete set of Feynman diagrams at NLO.

## 6.2 $W^+W^-b\bar{b}$ production: review of existing calculations

In this Section, we shall describe the setup used for calculating NLO QCD corrections to the  $pp \rightarrow W^+W^-b\bar{b}$  process, which is computationally more demanding than  $t\bar{t}$  production in the NWA. The full calculation at NLO contains all doubly-resonant top-quark diagrams, but also non-doubly resonant as well as non-factorizing contributions. Fig. 6.3 illustrates the additional Feynman diagrams.

At LO, the full  $W^+W^-b\bar{b}$  final-state including the non-resonant diagrams has been computed in Refs. [127, 129–131]. In general, the calculation of NLO corrections poses some technical problems because of the existence of  $b$ -quarks in both initial- and final-state. In the 5-flavour scheme (5FNS), where  $b$ -quarks are treated as massless, collinear  $g \rightarrow b\bar{b}$  splittings contribute to the final-state and the corresponding IR divergence has to be handled (see Section 6.3). Considering massive  $b$ -quarks (4FNS) has the advantage of allowing any phase space restrictions on the  $b$ -quarks without endangering infrared safety, and thus allows to consider exclusive 0-, 1- and 2-jet bins for  $pp \rightarrow$

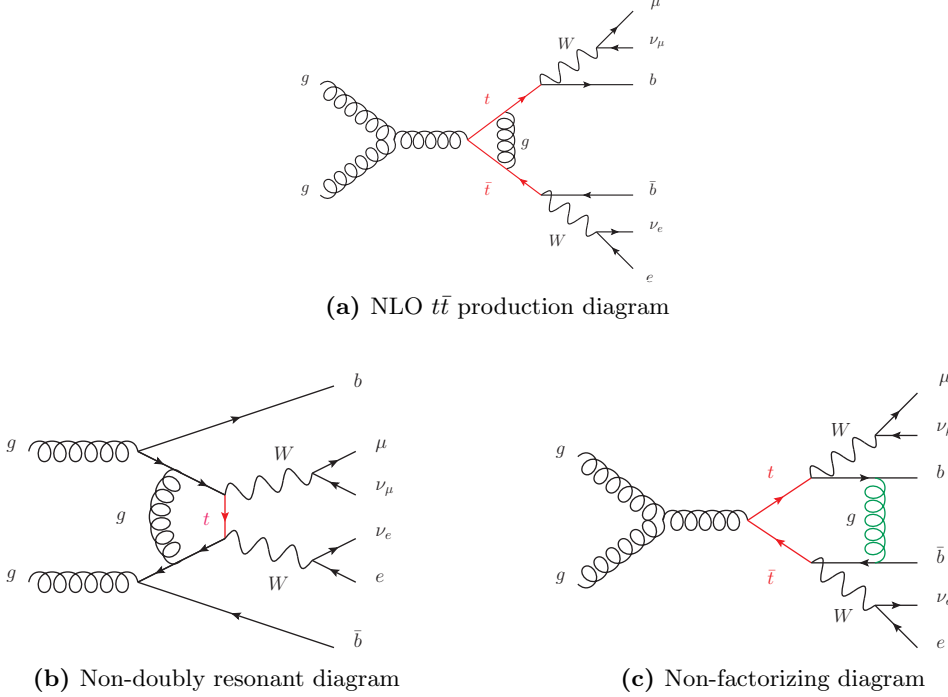


**Figure 6.3:** One-loop diagrams for  $pp \rightarrow W^+W^-b\bar{b}$  production contain (a) NLO corrections to standard NWA  $t\bar{t}$  production, but also (b) diagrams with one or no top-quark propagators and (c) resonant diagrams with non-factorizing legs

(e<sup>+</sup> $\nu_e$ )(μ<sup>-</sup> $\bar{\nu}_\mu$ ) $b\bar{b}$  in the same setup. On the other hand, massive  $b$ -quarks are accompanied by an additional mass scale to the one-loop integrals and thus renders the integral evaluation less straightforward. In Refs. [132, 133], NLO calculations in the 4FNS have been performed.

Often, the  $W^+W^-b\bar{b}$  prediction differs from the NWA in phase-space regions accessible only at NLO or sensitive to the top-quark decay kinematics. In Ref. [127], particular emphasis has been put on the impact of the non-factorising contributions on the top quark mass measurements in the dilepton channel. Recently the calculation of the NLO QCD corrections to  $W^+W^-b\bar{b}$  production with full off-shell effects has also been achieved in the lepton+jets channel [134].

### 6.3 $W^+W^-b\bar{b}$ calculation setup at NLO QCD

The calculation is analogous to the one described in Ref. [135]. We compute the NLO QCD corrections to the  $pp \rightarrow W^+W^-b\bar{b} \rightarrow (e^+\nu_e)(\mu^-\bar{\nu}_\mu)b\bar{b}$  process, i.e. up to  $\mathcal{O}(\alpha_s^2\alpha^2)$ , in the 5-flavour scheme. This means that interference from (massless)  $b$ -quarks in the initial-state is taken into account. Top-quark finite width effects are fully included. The complex mass scheme is used to incorporate the width in a gauge-invariant way, where the top-quark mass is replaced by a complex number  $\mu_t$ :

## 6 Theoretical predictions for $t\bar{t}$ final-states

$$\mu_t^2 = m_t^2 - im_t\Gamma_t . \quad (6.5)$$

1169     The  $W$ - and intermediate  $Z$ -bosons also acquire a complex mass. Note that we consider  
 1170     only resonant  $W$ -boson diagrams: non-resonant contributions and finite- $W$ -width  
 1171     effects were found to be small compared to top-quark effects [136]. The calculation is  
 1172     realized at parton-level within the SHERPA v2.2.3 framework,<sup>1</sup> where we used tree-level  
 1173     and real amplitudes from SHERPA matrix-element generators COMIX and AMEGIC. The  
 1174     one-loop amplitudes are compiled by GO-SAM and linked to SHERPA via the BLHA  
 1175     interface. Finally, the IR divergences are subtracted with the help of the Catani-Seymour  
 1176     dipole formalism as automated in SHERPA.

1177     There are 334 diagrams contributing to the  $q\bar{q} \rightarrow W^+W^-b\bar{b}$  virtual corrections, where  
 1178      $q$  are the light quarks  $u, d, s, c$ , and 1068 diagrams to  $gg \rightarrow W^+W^-b\bar{b}$ . Additionally,  
 1179     because of the  $b$ -quarks present in the initial-state, 668 one-loop diagrams contribute  
 1180     to  $b\bar{b} \rightarrow W^+W^-b\bar{b}$ .

1181     In the results presented in Chapters 7 and 8, the full  $pp \rightarrow W^+W^-b\bar{b} \rightarrow (e^+\nu_e)(\mu^-\bar{\nu}_\mu)b\bar{b}$   
 1182     QCD NLO prediction is compared with various  $t\bar{t}$  predictions in the NWA. To disentangle  
 1183     the effects from production and decay corrections (as well as extra radiation in  
 1184     a parton-shower resummed approximation), the four theoretical descriptions considered  
 1185     in the next Chapter are summarized again for completeness:

1186     **NLO<sub>full</sub>**: full NLO corrections to  $pp \rightarrow W^+W^-b\bar{b}$  with leptonic  $W$ -decays,

1187     **NLO<sub>NWA</sub><sup>NLOdec</sup>**: NLO  $t\bar{t}$  production  $\otimes$  NLO decay,

1188     **NLO<sub>NWA</sub><sup>LOdec</sup>**: NLO  $t\bar{t}$  production  $\otimes$  LO decay,

1189     **NLO<sub>PS</sub>**: NLO  $t\bar{t}$  production+shower  $\otimes$  decay via parton showering.

1190     The PDF4LHC15\_nlo\_30\_pdfs sets are interfaced to SHERPA via LHAPDF and events  
 1191     are produced at a center-of-mass energy of  $\sqrt{s} = 13$  TeV. The central top-quark mass  
 1192     was set to  $m_t = 172.5$  GeV and the  $G_\mu$ -electroweak scheme was used with the following  
 1193     numerical values:

$$G_\mu = 1.16637 \cdot 10^{-5} \text{ GeV}^{-2}, \quad M_W = 80.385 \text{ GeV}, \quad M_Z = 91.1876 \text{ GeV}, \quad (6.6)$$

$$\begin{aligned} \Gamma_t^{\text{LO}} &= & 1.4806 \text{ GeV}, & \Gamma_t^{\text{NLO}} &= & 1.3535 \text{ GeV}, \\ \Gamma_W^{\text{LO}} &= & 2.0454 \text{ GeV}, & \Gamma_W^{\text{NLO}} &= & 2.1155 \text{ GeV}, \\ \Gamma_Z &= & 2.4952 \text{ GeV}, & & & \end{aligned} \quad (6.7)$$

1194     where the LO (NLO) widths were used for the LO (NLO) decays, respectively.

---

<sup>1</sup>A patched version was used for the CSS shower, with the correct eikonal expressions for radiating off massive top-quarks.

## 1195 6.4 Event requirements

1196 To give a more quantitative assessment of the difference between our predictions with  
 1197 respect to the extracted top-quark mass, we implement an analysis that is similar to  
 1198 the ATLAS top-quark mass measurement in the dilepton channel at 8 TeV [137], where  
 1199 the trigger cuts on leptons and jets are adapted to the ATLAS 13 TeV standards. For  
 1200 details of the analysis, the reader is referred to Chapter 7. We require:

1201 •  $n_{b,\text{jets}} = 2$  with  $p_T^{\text{jet}} > 25 \text{ GeV}$  and  $|\eta^{\text{jet}}| < 2.5$ . Jets are clustered with **FastJet** [138,  
 1202 139] using a jet radius parameter of  $\Delta R = 0.4$ . Jets containing a  $b\bar{b}$  pair are also  
 1203 defined as  $b$ -jets.

1204 • exactly two oppositely charged leptons which fulfill  $p_T^\mu > 28 \text{ GeV}$ ,  $|\eta^\mu| < 2.5$  for  
 1205 muons and  $p_T^e > 28 \text{ GeV}$ ,  $|\eta^e| < 2.47$  for electrons excluding the dead region  
 1206  $1.37 < |\eta^e| < 1.52$  between barrel and endcap EM calorimeters. For charged  
 1207 leptons we require a separation of  $\Delta R(\ell, \text{jet}) > 0.4$  to any jet.

1208 •  $p_T^{\ell b} > 120 \text{ GeV}$ . Using the same lepton- $b$ -jet assignments as for  $m_{\ell b}$ , we define  $p_T^{\ell b}$   
 1209 as the average transverse momentum of both lepton- $b$ -jet systems.

1210 We chose  $\mu_R = \mu_F = m_t$  as our central scale. The scale variation bands are obtained  
 1211 by varying  $\mu_{R,F} = c_{R,F} m_t$ , with  $(c_R, c_F) \in \{(0.5, 0.5), (2, 2)\}$ .<sup>2</sup>

In the NWA parton-shower results, the central scale was also compared to a dynamic scale called  $\mu_{t\bar{t}}$ . The latter is a “colour-flow inspired” QCD scale suggested in Ref. [140]. For the Mandelstam invariants  $s$ ,  $t$  and  $u$ , the dynamic scale is given by

$$\mu_{t\bar{t}}^2(q\bar{q} \rightarrow t\bar{t}) = 2 p_q p_t = m_t^2 - t , \quad (6.8)$$

$$\mu_{t\bar{t}}^2(\bar{q}q \rightarrow t\bar{t}) = 2 p_q p_t = m_t^2 - u , \quad (6.9)$$

$$\mu_{t\bar{t}}^2(gg \rightarrow t\bar{t}) = \begin{cases} m_t^2 - t & \text{with weight } w_1 \propto \frac{u-m_t^2}{t-m_t^2} + \frac{m_t^2}{m_t^2-t} \left\{ \frac{4t}{t-m_t^2} + \frac{m_t^2}{s} \right\} \\ m_t^2 - u & \text{with weight } w_2 \propto \frac{t-m_t^2}{u-m_t^2} + \frac{m_t^2}{m_t^2-u} \left\{ \frac{4u}{u-m_t^2} + \frac{m_t^2}{s} \right\} , \end{cases} \quad (6.10)$$

1212 the value of  $\mu_{t\bar{t}}$  being chosen with a probability proportional to the two weights  $w_1$ ,  $w_2$ .

---

<sup>2</sup>Also, 7-point variations were considered but the simultaneous variations are identical to their envelope.

## 1213 6.5 Total cross-section results

1214 The fiducial cross-sections after applying the aforementioned cuts are given in Table 6.2  
 1215 for all considered predictions, where we also add production at LO accuracy for com-  
 1216 pleteness. The renormalization and factorization scale uncertainties are given in percent.

	X=LO [fb]	X=NLO [fb]
$\mathbf{X}_{\text{full}}$	$(739.5 \pm 0.3)^{+31.5\%}_{-22.4\%}$	$(914 \pm 3)^{+2.1\%}_{-7.6\%}$
$\mathbf{X}_{\text{NWA}}^{\text{LOdec}}$	$(727.3 \pm 0.2)^{+31.4\%}_{-22.3\%}$	$(1029 \pm 1)^{+10.4\%}_{-11.5\%}$
$\mathbf{X}_{\text{NWA}}^{\text{NLOdec}}$	-	$(905 \pm 1)^{+2.3\%}_{-7.7\%}$
$\mathbf{X}_{\text{PS}}, \mu = m_t$	$(637.7 \pm 0.9)^{+29.7\%}_{-21.0\%}$	$(886 \pm 1)^{+8.5\%}_{-9.3\%}$
$\mathbf{X}_{\text{PS}}, \mu = \mu_{t\bar{t}}$	$(499.7 \pm 0.7)^{+27.6\%}_{-19.3\%}$	$(805.2 \pm 0.9)^{+12.3\%}_{-10.9\%}$

1217 **Table 6.2:** Cross-sections for all predictions at LO, respectively NLO in production, where the  
 1218 top-quark mass  $m_t = 172.5$  GeV. The uncertainty stemming from MC integration  
 1219 is given in parentheses, and scale variation uncertainties are shown in percent.

1220 While the cross-sections for  $\text{NLO}_{\text{full}}$  and  $\text{NLO}_{\text{NWA}}^{\text{NLOdec}}$  agree with each other within  
 1221 expectations, the  $\text{NLO}_{\text{NWA}}^{\text{LOdec}}$  cross-section is about 13% higher than the latter. The  
 1222  $\text{NLO}_{\text{PS}}$  cross-section, in comparison, is smaller because of the softening of  $b$ -jets which  
 1223 leads to a higher rejection rate when taking jet requirements into account. The  $\mu_{t\bar{t}}$   
 1224 scale is larger than the central scale  $m_t$ , thus the even smaller cross-section for this  
 1225 scale choice. Notice also the reduction in the renormalization and factorization scale  
 1226 uncertainties when including NLO corrections to the top-quark decay. Usually, rather  
 1227 than total inclusive cross-sections, the most sensitive top-quark mass measurements rely  
 1228 on differential distributions, where mostly the distributions for  $t\bar{t}$  final-states are MC-  
 1229 generated and *fitted* to extract the top-quark mass. One caveat of considering differential  
 1230 distributions is that the measured top-quark mass is rather represented by the MC input  
 1231 top-quark mass parameter  $m_t^{\text{MC}}$ , instead of the top-quark pole mass (or any other QFT-  
 1232 defined mass) measured in inclusive  $t\bar{t}$  measurements.

1233 Leaving the difference between heavy-quark mass schemes aside, we detail the exact  
 1234 procedure used in current ATLAS analyses for measuring the MC top-quark mass in  
 1235 the next Chapter, along with quantitative comparisons of the theoretical predictions  
 1236 outlined above.

# <sup>1234</sup> 7 NWA versus $W^+W^-b\bar{b}$ : Top-quark mass <sup>1235</sup> uncertainties at parton-level

<sup>1236</sup> We base our extraction of the top-quark mass on the ATLAS 8 TeV analysis in the  
<sup>1237</sup> dilepton channel [137], where we adapted the ATLAS cuts to the 13 TeV center-of-  
<sup>1238</sup> mass energy. This Chapter first introduces the template fit method that was used in  
<sup>1239</sup> the experimental measurement. After a short discussion of important features of the  
<sup>1240</sup> considered observables, the results for the fit of the top-quark mass and its dependence  
<sup>1241</sup> on the different theoretical descriptions of the  $t\bar{t}$  dilepton final-state are laid out.

## <sup>1242</sup> 7.1 The template fit method

<sup>1243</sup> In the dilepton channel, the top-quark momenta cannot be fully reconstructed because  
<sup>1244</sup> of the two-particle spectrum spread given by the neutrinos from both  $W$ -decays. One  
<sup>1245</sup> successful method is to use a differential distribution that is sensitive to the top-quark  
<sup>1246</sup> mass instead and which can be defined without having to properly reconstruct the top-  
<sup>1247</sup> quark intermediate states. The procedure is the following:

- <sup>1248</sup> • Choose a distribution that is sensitive to the theoretical top-quark mass: for ex-  
<sup>1249</sup> ample, we choose the average invariant mass of the lepton- $b$ -jet system  $m_{\ell b}$  (which  
<sup>1250</sup> make up the visible top-quark decay products) as a function of the top-quark mass  
<sup>1251</sup> set in the MC event generator.
- <sup>1252</sup> • Generate distributions for different input top-quark masses  $m_t^{\text{in}}$ . These are called  
<sup>1253</sup> *template* distributions.
- <sup>1254</sup> • Individually fit the template distributions simulated for the input masses  $m_t^{\text{in}}$  with  
<sup>1255</sup> an appropriate function. If we consider the simple example of a Gaussian fit, this  
<sup>1256</sup> gives:

$$\mathcal{G}(A, \mu, \sigma; m_t^{\text{in}}) = A(m_t^{\text{in}}) \exp\left(-\frac{\mu(m_t^{\text{in}}) - m_t^{\text{in}}}{2\sigma^2(m_t^{\text{in}})}\right), \quad (7.1)$$

<sup>1257</sup> where the parameters  $A, \mu, \sigma$  are fit to the distributions generated for each input  
<sup>1258</sup> mass.

<sup>1259</sup> This step is called *calibration* in the following paragraphs, and the functions for each  
<sup>1260</sup> of the input top-quark masses are called calibration functions. The dependence of the  
<sup>1261</sup> parameters on  $m_t^{\text{in}}$  is assumed to be linear, a fact that is checked against the MC

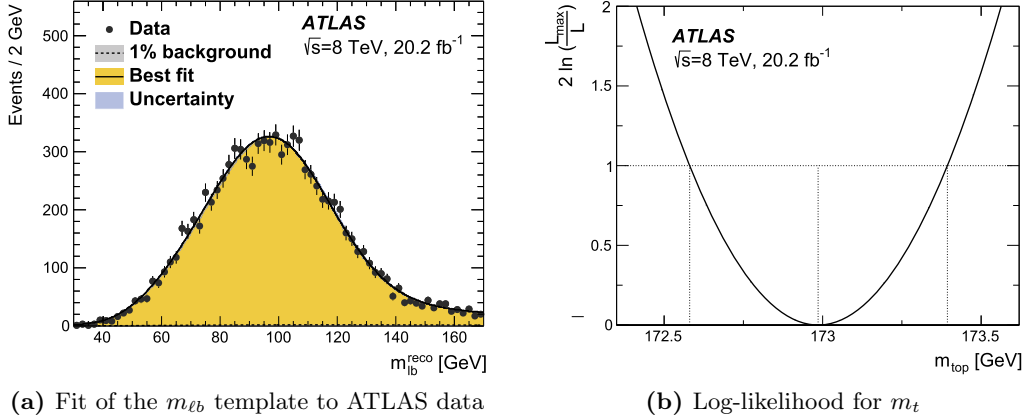


**Figure 7.1:** (a) The ATLAS 8 TeV analysis generates template distributions for  $m_{\ell b}$  for different input top-quark masses. These are fitted by a suitable function which parameters are expressed as linearly-dependent functions of  $m_t$ . (b) The likelihood function for  $m_t$  is then maximized in an unbinned fit to the measured  $m_{\ell b}$  distribution to extract the top-quark mass (Figures from Ref. [137]).

prediction. Once it is confirmed, the linear dependence is imposed (in our example,  $A(m_t^{\text{in}}) = a + b \cdot m_t^{\text{in}}$  with  $a$  and  $b$  fixed, and analogously for  $\mu(m_t^{\text{in}})$ ,  $\sigma(m_t^{\text{in}})$ ). The underlying linear parameters are then kept constant, and the only floating parameter is the extracted top-quark mass  $m_t = m_t^{\text{out}}$  to be measured. This function can then be used directly in an unbinned likelihood fit to the distribution measured in experimental data, as shown in Fig. 7.1 as an illustration from the ATLAS 8 TeV measurement.

For a satisfying modeling of the  $m_{\ell b}$  distribution, the sum of a Gaussian and a Landau distribution is used in the analysis. Also, the overall normalization factor is fit to the measured cross-section after cuts are applied. In the rest of this Chapter, we repeat the extraction from a custom analysis implemented in `Rivet` [141] similar to the one performed by ATLAS, for the four different theoretical setups presented in Chapter 6 at parton-level (at particle-level for the parton-showered  $t\bar{t}$  results). We also compare different observables in addition to  $m_{\ell b}$ .

## 7.2 Definition of the observables

The results presented in the rest of this Chapter were published in Ref. [142]. The reader is referred to the latter for details that are omitted in the following. We study a list of observables that should in principle be maximally sensitive to the top-quark mass while minimally sensitive to theoretical systematic uncertainties (that is, including differences between NWA and full  $W^+W^-b\bar{b}$  predictions):

- $m_{\ell b}$  – the invariant mass of the lepton- and  $b$ -jet system

$$m_{\ell b}^2 = (p_{\ell} + p_b)^2. \quad (7.2)$$

### 7.3 Comparison of the different theoretical descriptions

Since both top-quarks decay leptonically, and since there is no possibility to determine the charge of the  $b$ -jets experimentally, there is an ambiguity in the assignment of the lepton and  $b$ -jet to the two top-quarks. We use here the same criterion as the ATLAS analysis: the two possible pairs for the lepton- $b$ -jet system ( $\ell^+ b_1, \ell^- b_2$ ) are tried out, and we choose the pairing that minimizes the sum of the two  $m_{\ell b}$  values per event.

- $m_{T2}$  – following Refs. [143, 144] in the case of the final-state  $(e^+\nu_e)(\mu^-\bar{\nu}_\mu)b\bar{b}$ , the definition of this variable is given by

$$m_{T2}^2 = \min_{p_T^{\nu_1} + p_T^{\nu_2} = p_T^{\text{miss}}} \left[ \max \left\{ m_T^2 \left( p_T^{(\ell^+ b_1)}, p_T^{\nu_1} \right), m_T^2 \left( p_T^{(\ell^- b_2)}, p_T^{\nu_2} \right) \right\} \right]. \quad (7.3)$$

The same pairing as for  $m_{\ell b}$  is chosen for the lepton and  $b$ -jet systems, and the transverse mass is defined as

$$m_T^2 \left( p_T^{(\ell b_i)}, p_T^{\nu_i} \right) = m_{(\ell b_i)}^2 + 2 \left( E_T^{(\ell b_i)} E_T^{\nu_i} - p_T^{(\ell b_i)} p_T^{\nu_i} \right), \quad (7.4)$$

with  $E_T = \sqrt{|p_T|^2 + m^2}$  and we set  $m_{\nu_i} = 0$ .

- $E_T^{\Delta R}$  – the leptons' transverse energy weighted by the angular distance to the corresponding  $b$ -jet

$$E_T^{\Delta R} = \frac{1}{2} \left( E_T^{l_1} \Delta R(l_1, b_1) + E_T^{l_2} \Delta R(l_2, b_2) \right), \quad (7.5)$$

where again the above  $m_{\ell b}$  criterion is used.

Sets of MC samples were produced for input top-quark masses

$$m_t \in \{165.0, 172.5, 180.0\} \text{ [ GeV ]}. \quad (7.6)$$

The dependence on the input top-quark mass  $m_t$  is shown for all four observables in Fig. 7.2. Whereas  $m_{\ell b}$  and  $m_{T2}$  are the most sensitive to  $m_t$  with a ratio to the central choice of the order  $\mathcal{O}(2-3)$  for the considered masses, the dependence of the  $E_T^{\Delta R}$  and  $m_{\ell\ell}$  observables on the top-quark mass is rather weak.

## 7.3 Comparison of the different theoretical descriptions

The normalized differential cross-section for the  $m_{\ell b}$  observable is outlined in Fig. 7.3 for the four theoretical predictions presented in Chapter 6. We show the ratio to the complete  $W^+W^-b\bar{b}$  calculation, where the latter's scale uncertainties are represented by gray bands in the plot. Note that the  $m_{\ell b}$  distribution has a sharp kinematic edge at  $m_{\ell b}^{\text{edge}} = \sqrt{m_t^2 - m_W^2} \sim 153 \text{ GeV}$ . Beyond the kinematic edge, the bins are only populated by wrong lepton- $b$ -jet pairing, additional radiation from the initial-state clustered

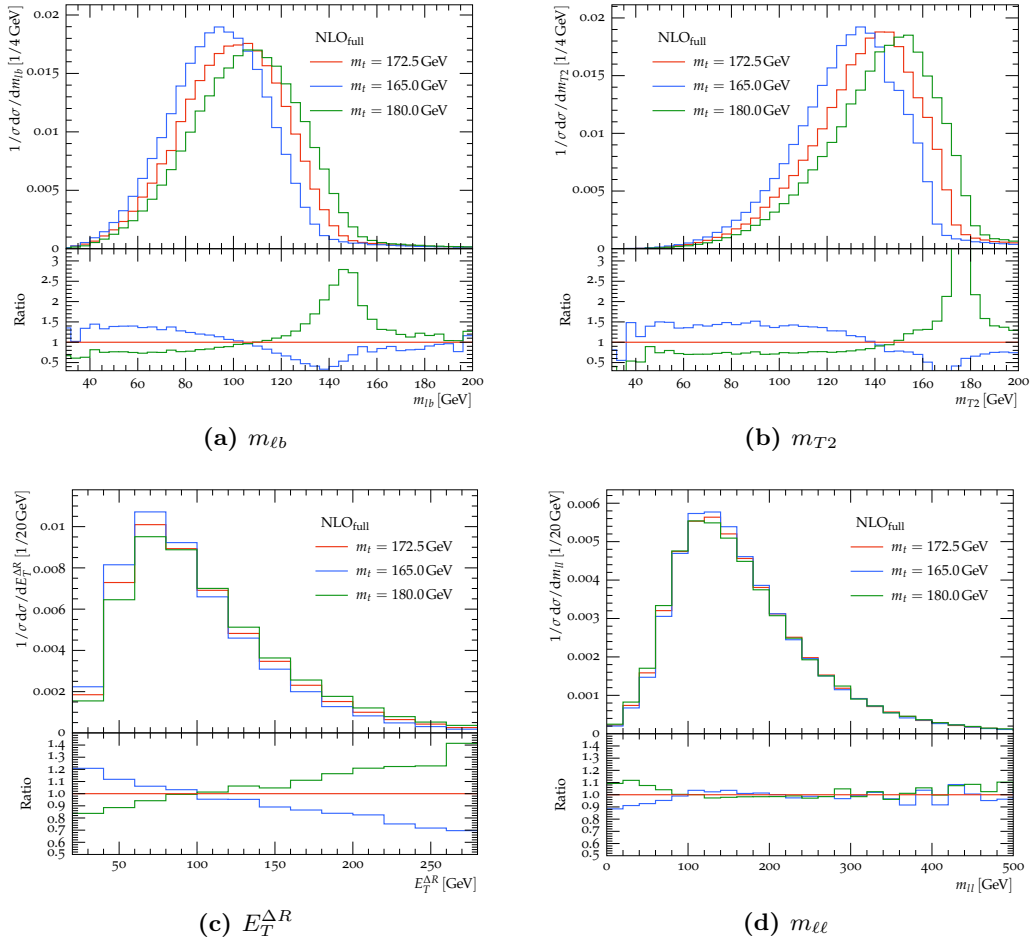


**Figure 7.2:** Differential observables are shown for three different top-mass points chosen symmetrically around  $m_t = 172.5$  GeV for the full  $W^+W^-b\bar{b}$  NLO prediction. While the (a)  $m_{\ell b}$  and the (b)  $m_{T2}$  observables show the highest top-mass dependence, the observables (c)  $E_T^{\Delta R}$  and (d)  $m_{\ell\ell}$  are not sensitive enough to the top-mass to be considered for the template fit.

along the lepton- $b$ -jet system, and non-resonant contributions. The LO cross-section for  $t\bar{t}$  production vanishes in this phase-space region. Thus, because NLO corrections represent the first non-trivial order contributing to this region, differences between the theoretical descriptions considered here are expected to be sizeable around and above this kinematic edge. On the other hand, as seen in Fig. 7.2, this region also displays the highest sensitivity to the top-quark mass. The template fit strategy should therefore be optimized to maximize the top-quark mass sensitivity while keeping the systematic uncertainty associated to the theoretical predictions to a minimum. We chose the fit range to be

### 7.3 Comparison of the different theoretical descriptions

$$40 \text{ GeV} \leq m_{\ell b} \leq 160 \text{ GeV}, \quad (7.7)$$

$$80 \text{ GeV} \leq m_{T2} \leq 180 \text{ GeV},$$

for  $m_{\ell b}$ , respectively for  $m_{T2}$ .

In Fig. 7.3, all predictions agree within a few percent in the bulk of the distribution,  $40 \text{ GeV} \leq m_{\ell b} \leq 140 \text{ GeV}$ , except for  $\text{NLO}_{\text{NWA}}^{\text{LOdec}}$ . The latter introduces a positive slope around and above the peak with differences of  $\mathcal{O}(-10)\%$  at small masses up to  $+20\%$  at  $\sim 140 \text{ GeV}$ , effectively shifting the peak to higher values of  $m_{\ell b}$ . This will translate into an artificially higher extracted mass for the top-quark when using LO decay predictions. In contrast,  $\text{NLO}_{\text{NWA}}^{\text{NLOdec}}$  is found within 4% of the  $\text{NLO}_{\text{full}}$  prediction for the bulk of the distribution, starting to differ above the kinematic edge and stagnating at  $-50\%$  of the full prediction in the tail, as expected. Finally, for the  $\text{NLO}_{\text{PS}}$  case, the tail at high  $m_{\ell b}$ -values is populated by the additional radiation from the parton-shower, and is driven closer to  $\text{NLO}_{\text{full}}$  while it mostly lies between  $\text{NLO}_{\text{NWA}}^{\text{LOdec}}$  and  $\text{NLO}_{\text{NWA}}^{\text{NLOdec}}$  in the rest of the distribution.

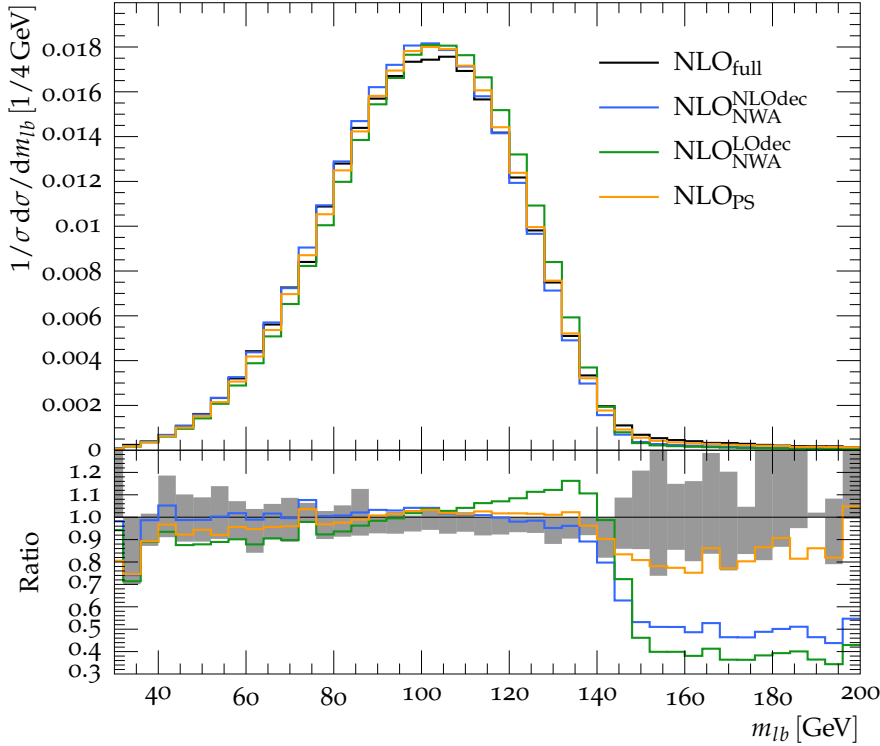


**Figure 7.3:** The normalized differential lepton- $b$ -jet system invariant mass  $m_{\ell b}$  is shown for all four theoretical predictions considered at 13 TeV, with their ratio to the  $\text{NLO}_{\text{full}}$  prediction. The gray band represents the latter's scale variation uncertainty.

Analogous features can be observed for the normalized distribution  $m_{T2}$  in Fig. 7.4 on a larger range up to the kinematic edge at  $m_{T2}^{\text{edge}} = m_t$ . In Figs. 7.5a and 7.5b, the

1331 normalized  $E_T^{\Delta R}$  and  $m_{\ell\ell}$  distributions show smaller differences between the theoretical  
 1332 predictions. Since they are much less sensitive to the top-quark mass, though, we do not  
 1333 consider them for the template fitting procedure in the results below.

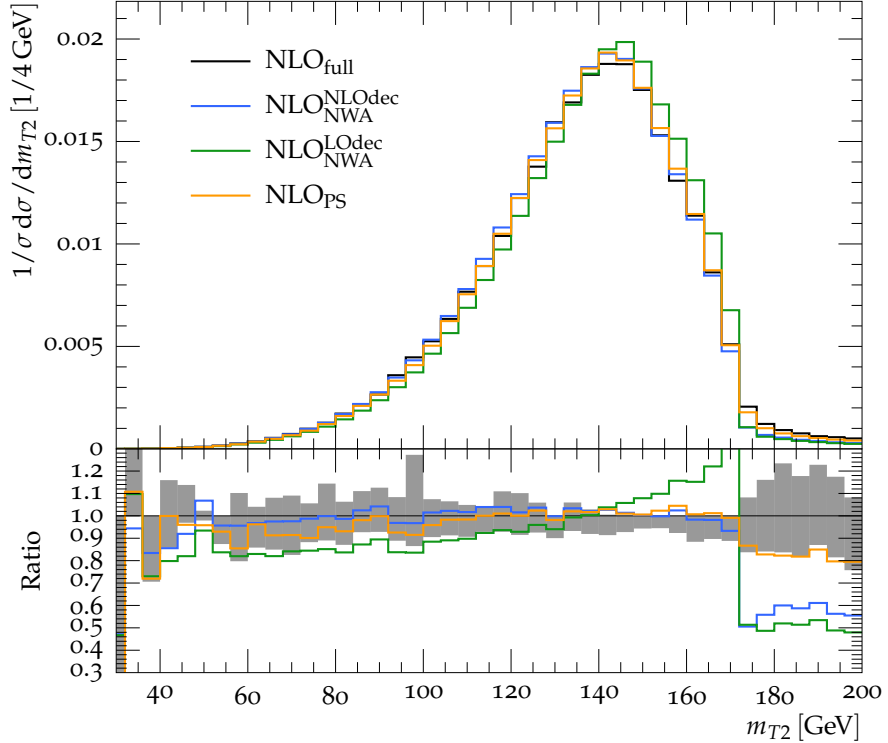


**Figure 7.4:** The normalized  $m_{T2}$  distribution is depicted for the four theoretical predictions, and shows a behavior similar to  $m_{\ell b}$ .

1334 It is also enlightening to look at the scale dependence of our four theoretical descrip-  
 1335 tions for LO, respectively NLO production. In Fig. 7.6a, the ratio of the  $W^+W^-b\bar{b}$   
 1336 prediction  $\text{NLO}_{\text{full}}$  to  $\text{LO}_{\text{full}}$  is shown for the  $m_{\ell b}$  observable. Although large corrections  
 1337 are expected above the kinematic edge when going from LO to NLO in production,  
 1338 one finds unexpectedly important corrections in the low-mass region as well, where dif-  
 1339 ferences between both orders of accuracy in production are not covered by the scale  
 1340 uncertainties. In the NWA case shown in Fig. 7.6b, describing the top-quark decays at  
 1341 NLO also pushes the prediction out of the  $\text{NLO}_{\text{NWA}}^{\text{LOdec}}$  scale uncertainties. The differ-  
 1342 ences between the  $\text{NLO}_{\text{NWA}}^{\text{LOdec}}$  and  $\text{NLO}_{\text{NWA}}^{\text{NLOdec}}$ , respectively  $\text{NLO}_{\text{PS}}$  are also not covered  
 1343 around the kinematic edge. In general, scale uncertainties in the NWA are shown to  
 1344 be misguidedly small in the tails of the  $m_{\ell b}$  and  $m_{T2}$  distributions. The behavior of  
 1345 scale-varied predictions is depicted for  $m_{T2}$ ,  $E_T^{\Delta R}$  and  $m_{\ell\ell}$  in Figs. 7.7–7.9.

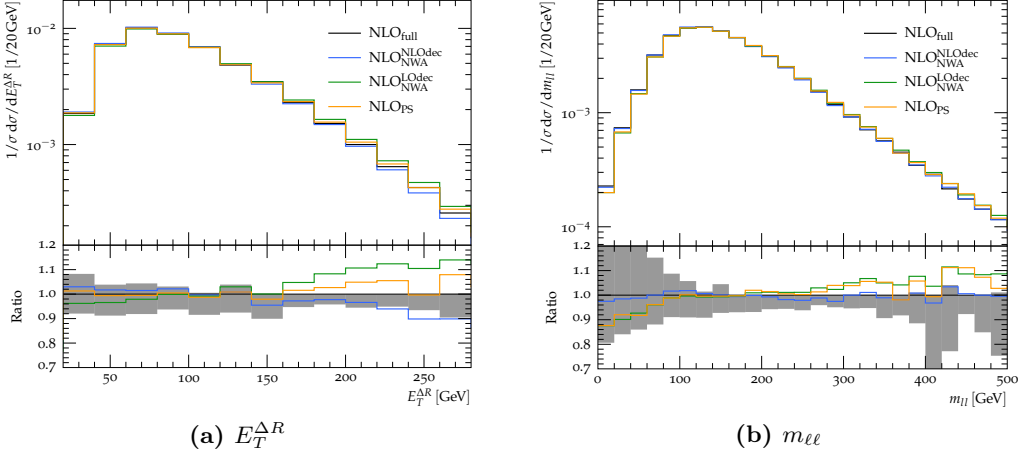


**Figure 7.5:** The normalized differential cross-sections for  $E_T^{\Delta R}$  and  $m_{\ell\ell}$  show less dependence on the theoretical description than the  $m_{\ell b}$  and  $m_{T2}$  observables, with differences that are maximally of  $\mathcal{O}(10 - 12\%)$  in the regions of lowest cross-section.

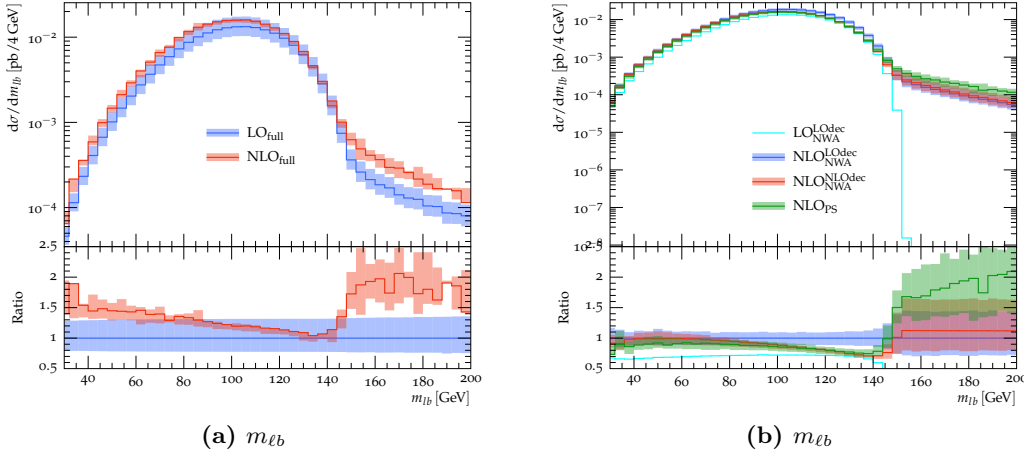


**Figure 7.6:** Results including scale variation bands for  $m_{lb}$ , for (a) the LO<sub>full</sub> and NLO<sub>full</sub> calculations, (b) the calculations based on the NWA. The ratios with respect to (a) LO<sub>full</sub> and (b) NLO<sub>NWA</sub><sup>L0dec</sup> are also shown.

## 1346 7.4 Template fit results

1347 After the qualitative discussion of differential results in the last Section, we now turn to  
 1348 the template fitting procedure and compare numerical values for the extracted top-quark  
 1349 mass from our different theoretical descriptions. To this effect, since we did not have  
 1350 real data to compare to, we adapt the procedure outlined in Section 7.1 and apply the  
 1351 following approach to produce plots like the ones displayed in Fig. 7.11:

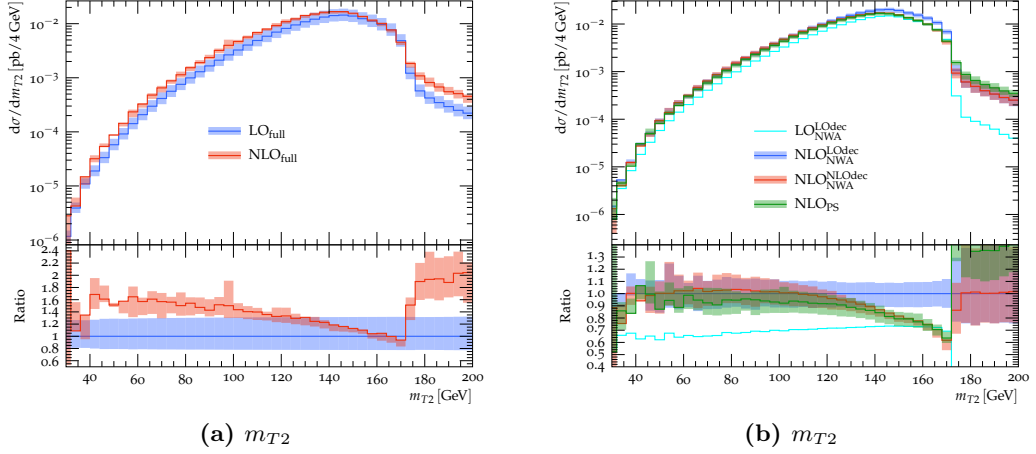


**Figure 7.7:** Results including scale variation bands for  $m_{T2}$ , for (a) the LO<sub>full</sub> and NLO<sub>full</sub> calculations, and (b) the calculations based on the NWA. The ratios are defined as in Fig. 7.6.

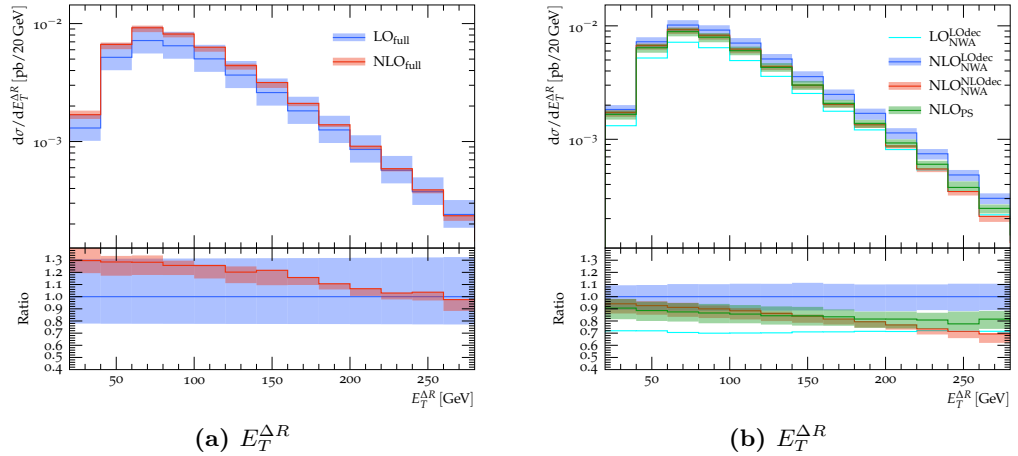


**Figure 7.8:** Results including scale variation bands for  $E_T^{\Delta R}$  for (a) the LO<sub>full</sub> and NLO<sub>full</sub> calculations, and (b) the calculations based on the NWA. The ratios are defined as in Fig. 7.6.

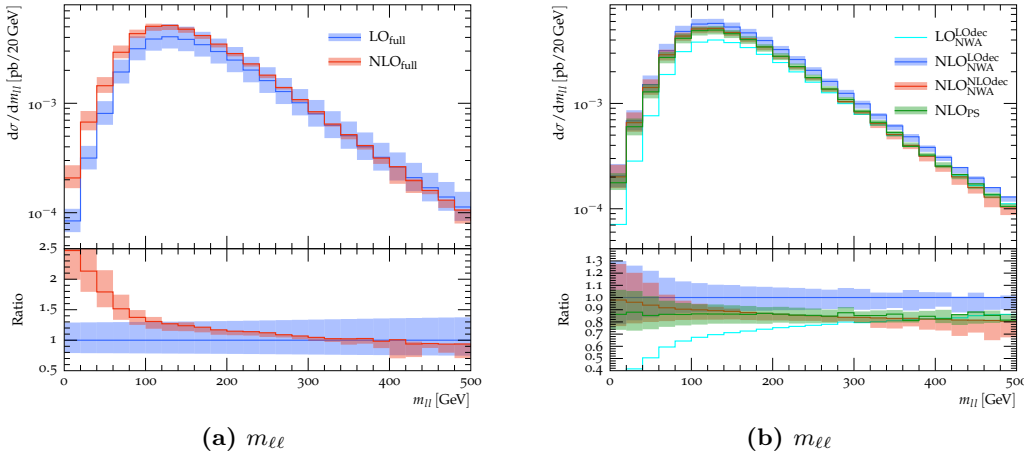


**Figure 7.9:** Results including scale variation bands for  $m_{ll}$ , for (a) the LO<sub>full</sub> and NLO<sub>full</sub> calculations, and (b) the calculations based on the NWA. The ratios are defined as in Fig. 7.6.

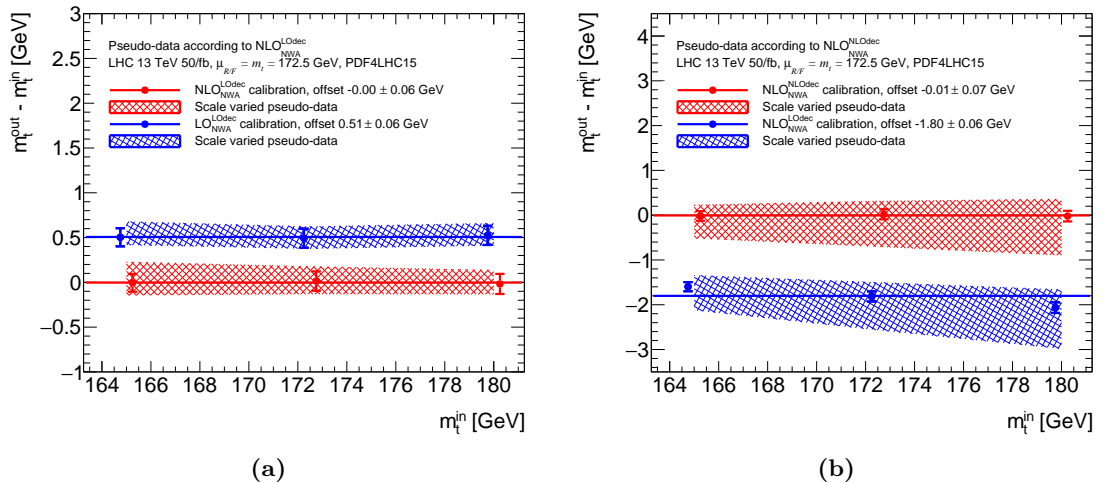
- **Simulation** : The distributions for  $m_{\ell b}$  and  $m_{T2}$  are produced with the three input top-quark masses  $m_t^{\text{in}}$  for all theoretical descriptions.
  - **Template calibration**: The template distributions produced in the first step are individually fitted to the sum of a Gaussian and a Landau function. The theoretical description used as a basis for the distribution is called the calibration set. In the example of Fig. 7.11a, the calibration sets are described by the red/blue reference points in the legend.
  - **Pseudo-data**: From the different theoretical descriptions, a subset of events is drawn and labeled as *pseudo-data*. This sample corresponds to a luminosity of  $50 \text{ fb}^{-1}$ . In Fig. 7.11a, the theoretical description used for producing pseudo-data is given at the top of the plot. In general, the pseudo-data set is drawn from the more complete of the two predictions, which should be closer to real data. Pseudo-experiments are performed by repeating the random drawing of the pseudo-data 1000 times from the subset of all events, for a given theory prediction.
  - **$m_t$  extraction**: For each of the input top-quark masses  $m_t^{\text{in}}$ , an unbinned likelihood fit is applied to the pseudo-data, using the corresponding calibration set, to determine the extracted value of the top-quark mass  $m_t^{\text{out}}$ .

1369 The normalization is kept fixed to the pseudo-data, so that the result of template fits  
 1370 only depend on differences in the distribution shape. Looking again at Fig. 7.11a for  
 1371 reference, the red/blue points indicate the bias of the extracted top-quark mass with  
 1372 respect to the MC input mass  $\Delta m_t^{\text{MC}} = m_t^{\text{out}} - m_t^{\text{in}}$ . When using the calibration func-  
 1373 tion generated from the same theoretical prediction as used to produce the pseudo-data,  
 1374 the offset  $\Delta m_t$  should be close to zero and serves as a cross-check that no systematic

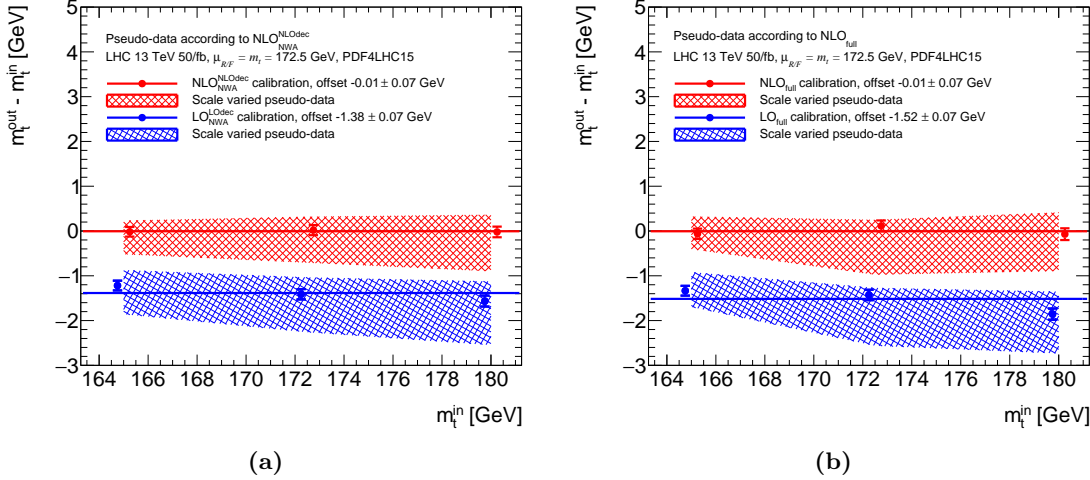
bias exists in the fitting procedure. The error bars on the points indicate the statistical  
 error associated with the finite pseudo-data sample. The results from the three mass  
 points are then fitted to a constant, and the numerical offset for  $\Delta m_t$  is given for each  
 prediction in the legend, accompanied by its statistical uncertainty. Finally, the sys-  
 tematic uncertainty bands are provided by fitting the calibration set to the scale-varied  
 pseudo-data.

Fig. 7.10a shows the offset between extracted and input top-quark masses when generating pseudo-data according to the  $\text{NLO}_{\text{NWA}}^{\text{LOdec}}$  prediction, and using the calibration function fitted from  $\text{LO}_{\text{NWA}}^{\text{LOdec}}$  MC templates in blue. The offset in  $m_t$  produced by going from LO to NLO in  $t\bar{t}$  production amounts to 0.51 GeV. For comparison, Fig. 7.10b gives the offset from fitting the  $\text{NLO}_{\text{NWA}}^{\text{NLOdec}}$  pseudo-data with the  $\text{NLO}_{\text{NWA}}^{\text{LOdec}}$  calibration function: higher-order corrections in the top-quark decay lead to a  $m_t$ -offset of  $-1.80$  GeV. Moreover, the NLO decay corrections in Fig. 7.10b lead to larger uncertainty bands, because the scale variations produce non-uniform shape differences. These results already highlight the importance of higher-order corrections to the top-quark decay in a mass measurement based on  $m_{tb}$ .

Fig. 7.11 gives results for the extracted top-quark mass bias when considering higher-order corrections in both production and decay, shown in Fig. 7.11a for the NWA case and in Fig. 7.11b for the full  $W^+W^-b\bar{b}$  case. The factorization of production and decay in the NWA approximation yields an offset of  $-1.38$  GeV, corresponding to the sum of the offsets in NLO production and decay shown in Fig. 7.10a, respectively Fig. 7.10b.



**Figure 7.10:** Pseudo-data is drawn according to (a)  $\text{NLO}_{\text{NWA}}^{\text{LOdec}}$  and (b)  $\text{NLO}_{\text{NWA}}^{\text{NLOdec}}$  for the three input top-quark masses. In each  $m_{tb}$  subplot, the calibration set from the same prediction (red) is used to show the absence of systematic bias in the template fit. The difference between the input mass and the template output is shown for each mass point. The calibration set from (a)  $\text{LO}_{\text{NWA}}^{\text{LOdec}}$  and (b)  $\text{NLO}_{\text{NWA}}^{\text{LOdec}}$  yields an offset (blue) in the top-quark mass extracted from the theoretically more complete respective pseudo-data of (a) 0.51 GeV and (b) -1.80 GeV.



**Figure 7.11:** From fitting the  $m_{\ell b}$  distribution, the bias for the extracted top-quark mass based on (a)  $\text{NLO}_{\text{NWA}}^{\text{NLOdec}}$  and (b)  $\text{NLO}_{\text{full}}$  pseudo-data underlines the effect of taking NLO contributions for production and decay into account.

Finally, we consider the offsets in  $m_t$  produced when fitting the  $\text{NLO}_{\text{full}}$  pseudo-data set with the calibration from the  $\text{NLO}_{\text{NWA}}^{\text{NLOdec}}$  and the  $\text{NLO}_{\text{PS}}$  predictions in Fig. 7.12a, respectively Fig. 7.12b. While  $\text{NLO}_{\text{NWA}}^{\text{NLOdec}}$  still yields a sizeable offset of 0.83 GeV, the uncertainty bands now overlap. In the case of the  $\text{NLO}_{\text{PS}}$  calibration, the offset with respect to  $\text{NLO}_{\text{full}}$  pseudo-data is compatible with zero within statistical uncertainties. Although the  $\text{NLO}_{\text{PS}}$  prediction does not describe the top-quark decay at NLO accuracy beyond the soft limit, it still largely reproduces the full  $W^+W^-b\bar{b}$  description for the most part of the  $m_{\ell b}$  fit range, as can be seen in Fig. 7.3. Further studies were performed to understand if the discrepancy between  $\text{NLO}_{\text{NWA}}^{\text{NLOdec}}$  and  $\text{NLO}_{\text{PS}}$  originates in the parton-shower resummation. More details are given in Appendix A, where the parton-shower number of emissions in both the  $t\bar{t}$  production and decay is gradually restricted, and offsets in  $m_t$  are compared to the  $\text{NLO}_{\text{NWA}}^{\text{NLOdec}}$  prediction. In particular, it seems that the general softening of  $m_{\ell b}$  (coming from resummation effects) around the kinematic edge is more important than the correct description of the hardest fixed-order radiative correction in the top-quark decay.

Similar results are also shown for the  $m_{T2}$  distribution in Appendix A. The numerical offsets for all comparisons are summarized in Table 7.1, together with a  $\chi^2$  computed from both  $m_{\ell b}$  and  $m_{T2}$  offsets for the same theoretical predictions. While almost all  $\chi^2$  values are consistent with zero, the comparison between  $\text{NLO}_{\text{NWA}}^{\text{NLOdec}}$  and  $\text{NLO}_{\text{PS}}$  differs significantly: the  $m_{T2}$  estimator for the top-quark mass is simply less sensitive to differences between the two latter predictions.

In conclusion, while NWA predictions are not disallowed, the former study shows that higher-order (and/or logarithmic) corrections to the top-quark decays are at least as important as corrections to  $t\bar{t}$  production. The comparisons presented above suffer from

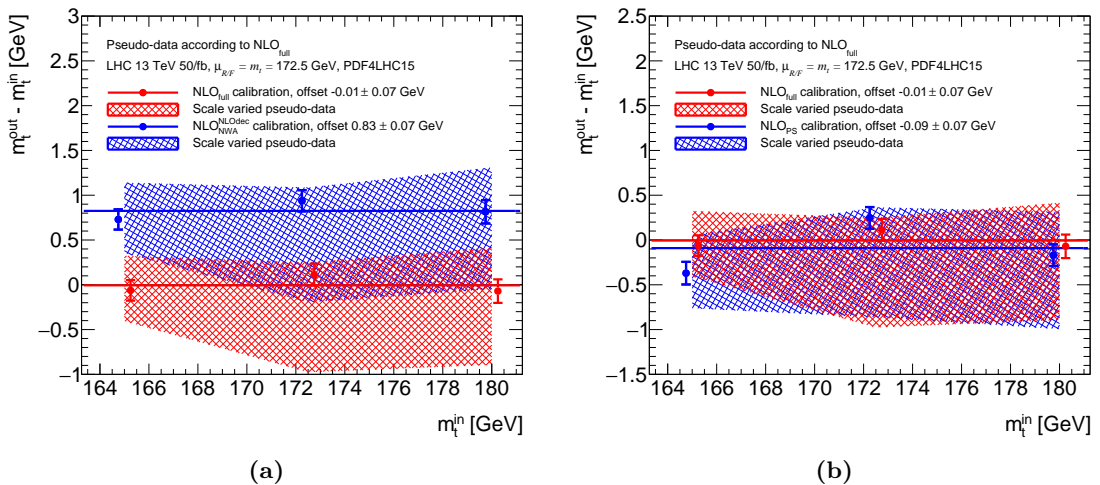


**Figure 7.12:** Top-quark mass bias from  $m_{tb}$  for pseudo-data generated from the NLO<sub>full</sub> prediction are reduced when considering the case of (a) NLO<sub>NWA</sub><sup>NLOdec</sup> and (b) NLO<sub>PS</sub> calibration functions.

1420 a few shortcomings: in particular, both non-perturbative effects (like hadronization)  
1421 and detector efficiencies are expected to partly wash out the differences observed in the  
1422 extracted top-quark mass. This is the subject of Chapter 9, which treats the topic in  
1423 an even closer experimental setup with the help of a folding procedure in the ATLAS  
1424 framework.

Pseudo-data	Calibration	Offset [GeV]		Figure		$\chi^2$
		$m_{\ell b}$	$m_{T2}$	$m_{\ell b}$	$m_{T2}$	
NLO <sub>NWA</sub> <sup>LOdec</sup>	LO <sub>NWA</sub> <sup>LOdec</sup>	+0.51 ± 0.06	+0.48 ± 0.04	7.10a	A.5a	0.17
NLO <sub>NWA</sub> <sup>NLOdec</sup>	NLO <sub>NWA</sub> <sup>LOdec</sup>	-1.80 ± 0.06	-1.67 ± 0.04	7.10b	A.5b	3.25
NLO <sub>NWA</sub> <sup>NLOdec</sup>	LO <sub>NWA</sub> <sup>LOdec</sup>	-1.38 ± 0.07	-1.24 ± 0.05	7.11a	A.5c	2.65
NLO <sub>NWA</sub> <sup>full</sup>	LO <sub>NWA</sub> <sup>full</sup>	-1.52 ± 0.07	-1.62 ± 0.05	7.11b	A.5d	1.35
NLO <sub>NWA</sub> <sup>full</sup>	NLO <sub>NWA</sub> <sup>NLOdec</sup>	+0.83 ± 0.07	+0.60 ± 0.06	7.12a	A.5e	6.22
NLO <sub>NWA</sub> <sup>full</sup>	NLO <sub>PS</sub>	-0.09 ± 0.07	-0.07 ± 0.06	7.12b	A.5f	0.05
NLO <sub>PS</sub>	NLO <sub>NWA</sub> <sup>LOdec</sup>	-0.92 ± 0.07	-1.17 ± 0.05	A.4a	A.5g	8.45
NLO <sub>PS</sub>	NLO <sub>NWA</sub> <sup>NLOdec</sup>	+0.96 ± 0.07	+0.68 ± 0.05	A.4b	A.5h	10.59
NLO <sub>PS</sub>	NLO <sub>PS</sub> ( $\mu_{t\bar{t}}$ )	-0.03 ± 0.07	+0.02 ± 0.05	A.6b	A.6d	0.34

**Table 7.1:** The offsets from the top-quark mass extraction are given in GeV for pairs of the considered theoretical descriptions, from which the pseudo-data is generated, respectively the calibration function produced. The results are given for both the  $m_{\ell b}$  and  $m_{T2}$  distributions, along with the corresponding plot references (see also Appendix A). Finally, the value of  $\chi^2$  is given for the offsets, and is defined as  $\chi^2 = (o_1 - o_2)^2 / (u_1^2 + u_2^2)$ , with  $i = 1, 2 = m_{\ell b}, m_{T2}$  and  $o_i \pm u_i$  are the corresponding offsets and their (uncorrelated) uncertainties.



# **8 Experimental resolution and bin migration**

In the following Chapter, we reproduce the results outlined above with full particle-level predictions and compare the NLO<sub>full</sub> prediction to  $t\bar{t}$  results in the ATLAS Athena framework. To study the extracted values of the top-quark mass at reconstruction level in a fast-simulation style, the distributions are folded from particle-level to detector-level in a custom implementation.

## **8.1 Inverse problems**

Usually, to compare experimentally measured cross-sections to a theoretical prediction, background contributions are first subtracted from data, and the corresponding signal distributions unfolded to particle-level so that available measurements can be directly compared to any theory prediction. The unfolding procedure is a particular example of inverse problems: having a true distribution  $f(x)$  for some observable  $\Omega$ ,  $x \in [\Omega_{\min}, \Omega_{\max}]$ , the measured distribution  $g(y)$  is given by the Fredholm integral equation:

$$g(y) = \int_{\Omega_{\min}}^{\Omega_{\max}} K(x, y) f(x) dx , \quad (8.1)$$

where the kernel  $K(x, y)$  is a continuous function. For binned results, discretizing Eq. (8.1) gives a linear equation for  $\mathbf{x}$ ,  $\mathbf{y}$  the  $n$ -, respectively  $m$ -bin histograms corresponding to the true, respectively the measured distribution:

$$y_j = \sum_{i=1}^n A_{ij} x_i, \quad j \in \{1, \dots, m\} , \quad (8.2)$$

where  $\mathbf{A}$  is the bin migration matrix. The problem of inverting Eq. (8.2), that is to uncover the true distribution  $\mathbf{x}$  of an observable  $\Omega$  from the measured signal distribution  $\mathbf{y}$ , is the foundation of unfolding procedures. Because noise in the measured function can lead to instabilities in the inversion of the response matrix  $\mathbf{A}$ , the procedure has to be regularized. There are two distinct unfolding methods: direct unfolding procedures, which usually implement some regularization parameter for a smooth inversion of Eq. (8.2), and iterative methods. For a short review of unfolding methods in particle physics, see Ref. [145].

In the case at hand, we compute bin migration matrices and detector efficiencies to directly fold the particle-level predictions to detector-level to apply the ATLAS 13 TeV dilepton analysis.

## 8.2 Folding setup in ATLAS

With one central prediction and one parameter for the template fit (e.g. the top-quark mass  $m_t$ ), one already has to produce and simulate as many samples as top-quark mass points. Fig. 8.1 illustrates the analysis workflow for five top-quark mass points.

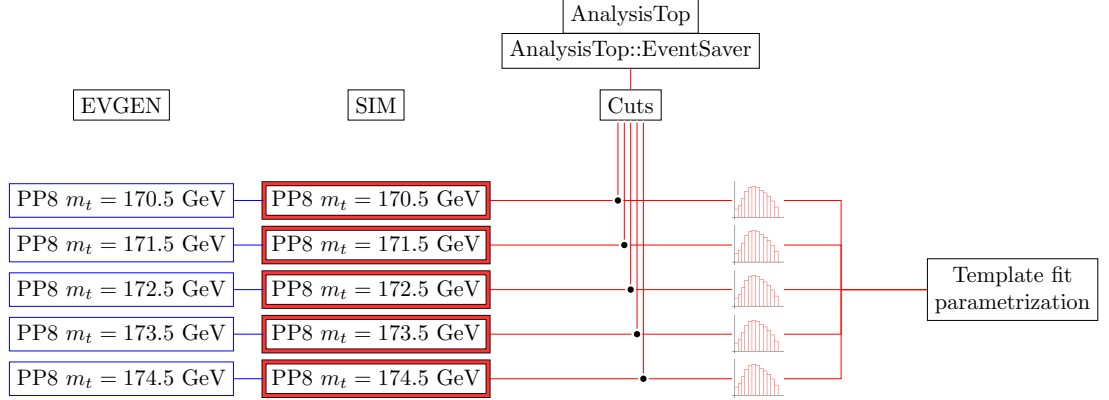


**Figure 8.1:** The workflow for a template fit with a central prediction (for example POWHEG+PYTHIA8 PP8) and five top-quark mass points. Each of the samples is produced at particle-level first (EVGEN in blue on the far left) and has to be simulated (SIM in red). The same analysis is run and distributions are produced for the individual top-mass samples, and fed to the template parametrization.

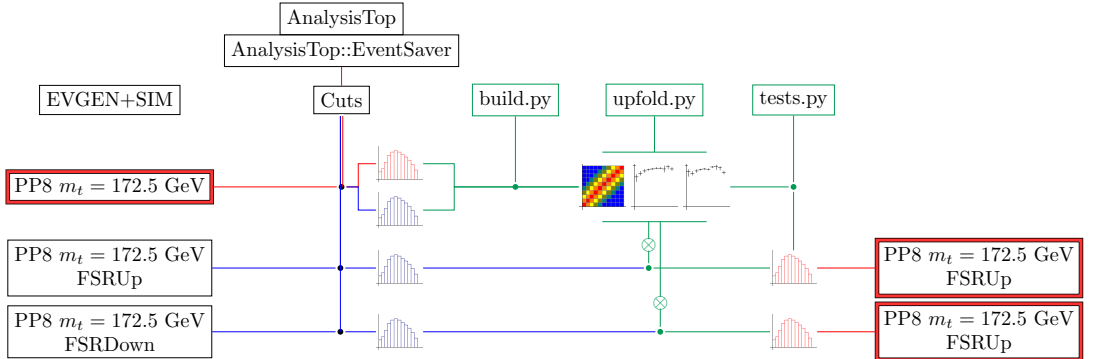


**Figure 8.2:** The folding package builds migration matrices and efficiency histograms from the simulated detector- and the particle-level of a central sample, for example POWHEG+PYTHIA8 with  $m_t = 172.5 \text{ GeV}$ . Histograms from variation samples (e.g. FSRUP and FSRDOWN here) can then be folded to detector-level and later be used in the template parametrization fit for an estimate of the uncertainty on the extracted top-quark mass, without having to fully simulate them.

In the ATLAS 13 TeV analysis, only the central sample is fully simulated with GEANT4 [146], while all samples entering the template fit parametrization are fast-simulated with the ATLFAST [147] package. The latter parametrizes the smeared detector response and reconstruction efficiencies for all physics objects. A custom event

1506

## Part III

1507

# Top-Quark Mass Effects in Higgs Pair Production

1508



# 1509 10 Top-mass dependence in Higgs pair 1510 production at NLO

1511 We switch to an entirely different sector of the SM, which is still related to the top-  
 1512 quark and its mass, namely the Higgs sector. After the discovery of the Higgs boson  
 1513 by both ATLAS [148] and CMS [149] experiments in 2012, which was the crowning  
 1514 completion of one of LHC’s foremost goals, the experimental community set to measure  
 1515 its properties to further test if it was compatible with the SM predicted Higgs boson. As  
 1516 of today, some of the Higgs boson properties are very well-measured (as for the example  
 1517 of its mass, spin, or couplings to heavier fermions and gauge bosons). Still, because  
 1518 of lower branching ratios or difficult background, the measurement of the Higgs boson  
 1519 couplings to light fermions, as well as the Higgs self-coupling, is still accompanied by  
 1520 high uncertainties (of the order of  $\mathcal{O}(10 - 20\%)$ ) which leave room for New Physics to  
 1521 appear. The latest ATLAS constraint on the Higgs boson self-coupling, in ratio to its  
 1522 predicted value from the SM  $c_{hhh} = \lambda/\lambda_{SM}$ , is  $-5.0 \leq c_{hhh} \leq 12.1$  [16] at 95% confidence  
 1523 level (CL), from a combination of three searches for the  $hh$  final-states  $b\bar{b}b\bar{b}$ ,  $b\bar{b}\tau^+\tau^-$  and  
 1524  $b\bar{b}\gamma\gamma$ . These bounds assume the other Higgs couplings to be SM-like. In the future, with  
 1525 the accumulation of statistics at high-luminosity (HL)-LHC, these bounds are expected  
 1526 to get improved, and the measurement of differential distributions (with a small number  
 1527 of total events) is even conceivable. In the rest of this Chapter, we review the theoretical  
 1528 standpoint of  $hh$  production, and show how New Physics strongly affects this process in  
 1529 the framework of a non-linear EFT.

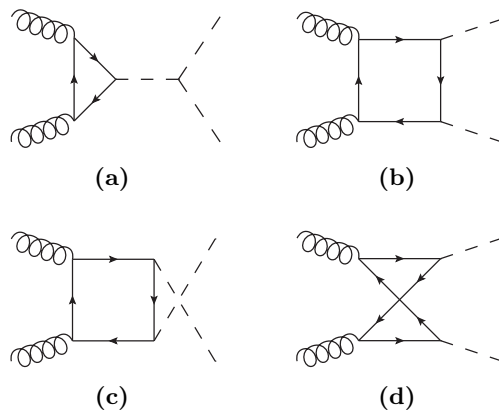


**Figure 10.1:** (a-d) LO Feynman diagrams for  $hh$  production by gluon-fusion.

## 1530 10.1 Theoretical descriptions of $hh$ production

1531 At the LHC, Higgs bosons (and in particular Higgs boson pairs, which we consider in  
 1532 the next Chapters) are produced mainly via a top-quark loop. Fig. 10.1 displays the LO  
 1533 Feynman diagrams for di-Higgs production in gluon-fusion: diagrams that contain the  
 1534 Higgs self-coupling  $\lambda$  are called *triangle*-like, and diagrams that do not *box*-like (at two-  
 1535 loop level, some diagrams do not contain the coupling  $\lambda$  but have triangular topologies,  
 1536 see e.g. the last diagram in Fig. 10.4). Because  $hh$  production is loop-induced, NLO  
 1537 corrections start at two-loop order already and pose a challenge to compute. The matrix-  
 1538 element for  $g(p_1, \mu, a) + g(p_2, \nu, b) \rightarrow h(p_3) + h(p_4)$  production decomposes into two form  
 1539 factors

$$\mathcal{M}_{ab}^{\mu\nu} = \frac{\alpha_s}{8\pi v^2} \delta_{ab} \epsilon_\mu \epsilon_\nu (F_1(\hat{s}, \hat{t}, m_h^2, m_t^2, d) T_1^{\mu\nu} + F_2(\hat{s}, \hat{t}, m_h^2, m_t^2, d) T_2^{\mu\nu}) , \quad (10.1)$$

1540 where the Lorentz structure is contained in the tensors  $T_1$ ,  $T_2$  and the functions  $F_1$ ,  
 1541  $F_2$  depend on four physical scales altogether (two kinematic invariants and both particle  
 1542 mass scales, as well as on the analytically-continued dimension  $d$ ). Finally, the first form  
 1543 factor can be further split into a contribution stemming only from triangle-like diagrams,  
 1544 respectively only box-like diagrams:

$$F_1 = F_\Delta + F_\square , \quad (10.2)$$

1545 and the box diagrams contribute to both  $F_\square$  and  $F_2$ . Historically, the LO one-loop  
 1546 total cross-section has been known analytically for a long time [150], and the triangular  
 1547 form factor given in Eq. (10.2), for  $\tau = 4m_t^2/\hat{s}$ , takes the form

$$F_\Delta = \frac{6m_h^2 \lambda \hat{s}}{\hat{s} - m_h^2} \tau (1 + (1 - \tau) f(\tau)) , \quad (10.3)$$

$$f(\tau) := \begin{cases} \arcsin^2\left(\frac{1}{\sqrt{\tau}}\right) & \tau \geq 1 \\ -\frac{1}{4} \left( \log\left(\frac{1+\sqrt{1-\tau}}{1-\sqrt{1-\tau}}\right) - i\pi \right)^2 & \tau < 1 . \end{cases}$$

1548 The triangle diagrams can be reduced to single Higgs production and subsequent  
 1549 attachment of the triple Higgs vertex, where all the NLO integrals (massive two-loop  
 1550 up to three-point) have been computed with the full top-mass dependence [151–153].  
 1551 The two-loop massive four-point integrals to  $gg \rightarrow hh$  are known analytically only  
 1552 partly [154–156]. Some computations exist with expansions in given kinematic limits  
 1553 (large top-quark mass [154], top-quark threshold [157], small Higgs transverse momen-  
 1554 tum [158], and high-energy expansion [159, 160]). We consider in the following only the  
 1555 heavy-top limit  $m_t \rightarrow \infty$ , without any expansion in  $1/m_t^{2n}$ , as well as several approxi-  
 1556 mations that include part of the full-theory result at NLO QCD.

### 1557 10.1.1 Approximations in the heavy-top limit ( $m_t \rightarrow \infty$ )

1558 To circumvent the direct computation of the difficult NLO QCD corrections to  $hh$ , one  
 1559 neat framework that was applied successfully in Higgs production (as well as in a whole  
 1560 collection of other processes) is to collapse one top-quark loop to an effective coupling  
 1561 between gluons and Higgs bosons within a so-called Effective Field Theory (EFT). EFTs  
 1562 are usually employed to describe physics entering at a higher-scale than the typical scales  
 1563 of the process at hand. In an agnostic approach, one assumes nothing about new particles  
 1564 whatsoever and instead computes effective couplings between known particles, that are  
 1565 only indirectly affected by more massive particles. Their exact degrees of freedom are  
 1566 thus integrated out of the calculation. This was for example the basic framework of  
 1567 the Fermi theory before  $W$ - and  $Z$ -bosons were discovered, where one assumes a 4-  
 1568 particle interaction vertex between fermions coupling with strength  $G_F$ . In the case  
 1569 of di-Higgs production, the top-quark degrees of freedom are integrated out and an  
 1570 effective coupling between gluons and Higgs bosons is introduced. There exist different  
 1571 consistent formulations of a theory with effective coupling vertices between gluons and  
 1572 Higgs bosons: usually, one introduces higher-dimension contact operators into the SM  
 1573 Lagrangian, with an EFT expansion in the New Physics scale  $1/\Lambda$ .<sup>1</sup> An alternative EFT  
 1574 formulation will be introduced in Section 10.2.

1575 In the next Sections, comparisons are shown between predictions for the full theory  
 1576 at QCD NLO and various approximations based on the heavy-top limit for variations of  
 1577 the Higgs couplings.<sup>2</sup> In order of increasing accuracy, these are:

- 1578 • **Pure HTL:** all top-quark loops are shrunk to an effective vertex between gluons  
 1579 and Higgs bosons. At LO, the form factors given in Eqs. (10.1), (10.3), for  $\tau \rightarrow \infty$ ,  
 1580 reduce to

$$F_{\Delta} \rightarrow \frac{3m_h^2 \lambda}{\hat{s} - m_h^2} \left( \frac{4}{3} \hat{s} \right), \quad (10.5)$$

$$F_{\square} \rightarrow -\frac{4}{3} \hat{s}, \quad (10.6)$$

$$F_2 \rightarrow 0. \quad (10.7)$$

1581 At NLO, they are at most given by one-loop diagrams.

- 1582 • **Born-improved HTL:** the virtual and real contributions are calculated within  
 1583 HTL, but reweighted on an event-by-event basis with the ratio of the full-theory  
 1584 Born to the HTL Born contribution,

$$d\sigma_{V,R}^{B,i} = d\sigma_{V,R}^{\text{HTL}} \frac{d\sigma_B^{\text{FT}}}{d\sigma_B^{\text{HTL}}}. \quad (10.8)$$

---

<sup>1</sup>Mostly, nowadays, analyses consider only dimension-6 operators, because the only dimension-5 operator violates lepton number conservation.

<sup>2</sup>In the SM case, there are already important differences between the considered approximations [161].

1585 • **FT<sub>approx</sub>** : the same prescription as given in Eq. (10.8) is applied for the virtual  
 1586 contribution, but the real-emission matrix-element is computed in the full theory  
 1587 (these are at most one-loop diagrams).

1588 • **Full theory:** the full two-loop virtual contribution is computed numerically.

### 1589 10.1.2 Two-loop contribution in the SM

1590 The first full computation of NLO QCD corrections to  $hh$  production in the SM was  
 1591 presented in Ref. [161]. All BSM results shown in Sections 10.3 and 11.2 are based on  
 1592 two-loop amplitudes calculated numerically for the SM.

1593 As a brief description of the calculation, the two-loop contribution to the SM amplitude  
 1594 was generated by an extended version of GoSAM called GoSAM-2LOOP. The reduction  
 1595 to master integrals was operated with REDUZE 2 [162], and the integral evaluation per-  
 1596 formed with the help of sector decomposition in SECDEC 3 [163–165]. In particular,  
 1597 the integration itself was implemented within a rank-one lattice quasi-Monte-Carlo rule  
 1598 (QMC) that is described in more detail in Ref. [166].

1599 Examples of the SM two-loop Feynman diagrams are given in the first, third and last  
 1600 rows of Fig. 10.4. The amplitude was calculated for a pre-sampled set of 5372 phase-  
 1601 space points at 14 TeV and 1343 points at 100 TeV, which are rescaled for non-SM values  
 1602 of the Higgs couplings (see Section 10.2). IR subtraction was performed within the CS  
 1603 dipole formalism, where for the  $gg$  channel, the insertion operator  $\mathbf{I}$  is given by

$$\mathbf{I}_{gg} = \frac{\alpha_s}{2\pi} \frac{(4\pi)^\epsilon}{\Gamma(1-\epsilon)} \left( \frac{\mu_R^2}{2p_1 \cdot p_2} \right)^\epsilon \cdot 2 \left( \frac{C_A}{\epsilon^2} + \frac{\beta_0}{2\epsilon} - C_A \frac{\pi^2}{3} + \frac{\beta_0}{2} + K_g \right), \quad (10.9)$$

1604 with  $\beta_0 = \frac{11}{6}C_A - \frac{2}{3}T_R N_f$  and  $K_g = \left( \frac{67}{18} - \frac{\pi^2}{6} \right) C_A - \frac{10}{9}T_R N_f$ . As a side note, the IR  
 1605 singular pattern is the same between the SM and the BSM case presented below. When  
 1606 inserting the CS operator into the Born term, see Eq. (4.8), the poles from the virtual  
 1607 contribution should cancel. To get the correct finite terms, thus, the Born has to be  
 1608 expanded up to  $\mathcal{O}(\epsilon^2)$ . The explicit cancellation of poles in  $\epsilon$  is checked numerically.

## 1609 10.2 The Electroweak Chiral Lagrangian

1610 Since we are interested in variations of the Higgs couplings, we consider the case of one  
 1611 particular extension of the SM called the Electroweak Chiral Lagrangian (EWChL) [167,  
 1612 168]. The latter framework is a non-linear realization of an EFT which will be described  
 1613 in some detail below. The EWChL, to leading-order, is given as

$$\begin{aligned}
 \mathcal{L}_2 = & -\frac{1}{2}\langle G_{\mu\nu}G^{\mu\nu} \rangle - \frac{1}{2}\langle W_{\mu\nu}W^{\mu\nu} \rangle - \frac{1}{4}B_{\mu\nu}B^{\mu\nu} + \sum_{\psi=q_L,l_L,u_R,d_R,e_R} \bar{\psi}iD\psi \\
 & + \frac{v^2}{4} \langle D_\mu U^\dagger D^\mu U \rangle (1 + F_U(h)) + \frac{1}{2}\partial_\mu h \partial^\mu h - V(h) \\
 & - v \left[ \bar{q}_L \left( Y_u + \sum_{n=1}^{\infty} Y_u^{(n)} \left( \frac{h}{v} \right)^n \right) UP_+ q_R + \bar{q}_L \left( Y_d + \sum_{n=1}^{\infty} Y_d^{(n)} \left( \frac{h}{v} \right)^n \right) UP_- q_R \right. \\
 & \left. + \bar{l}_L \left( Y_e + \sum_{n=1}^{\infty} Y_e^{(n)} \left( \frac{h}{v} \right)^n \right) UP_- l_R + \text{h.c.} \right], \tag{10.10}
 \end{aligned}$$

where  $U = \exp(2i\phi^a T^a/v)$  is the Goldstone matrix and contains the electroweak Goldstone fields  $\phi^a$ , and  $T^a$  are the generators of  $SU(2)_L$ . Here,  $P_\pm = 1/2 \pm T_3$  are the chiral projection operators, and the Higgs sector is characterized by an order-by-order expansion in the Higgs EW singlet  $h$ , given by the functions

$$F_U(h) = \sum_{n=1}^{\infty} f_{U,n} \left( \frac{h}{v} \right)^n, \quad V(h) = v^4 \sum_{n=2}^{\infty} f_{V,n} \left( \frac{h}{v} \right)^n. \tag{10.11}$$

The coefficients  $f_{U,n}$ ,  $V_{U,n}$  and  $Y_{u,d,e}^{(n)}$  are in principle free parameters and can be of  $\mathcal{O}(1)$ . The SM case is retrieved when

$$f_{U,1} = 2, \quad f_{U,2} = 1, \quad f_{V,2} = f_{V,3} = \frac{m_h^2}{2v^2}, \quad f_{V,4} = \frac{m_h^2}{8v^2}, \quad Y_f^{(1)} = Y_f. \tag{10.12}$$

Now, this Lagrangian is structured not in terms of canonical dimensions for the quantum fields and couplings, but rather in terms of *chiral* dimensions (as in the case of the chiral EFT of pions in QCD). The chiral dimension assigned to fields, derivatives and couplings are

$$d_\chi(A_\mu, \varphi, h) = 0, \quad d_\chi(\partial, \bar{\psi}\psi, g, y) = 1, \tag{10.13}$$

with  $A_\mu$  being any gauge field,  $g$  representing any of the SM gauge couplings, and  $y$  any weak coupling (like the Yukawa couplings). The ordering in the chiral dimension  $d_\chi$  is equivalent to counting the number of loops  $L$ ,  $d_\chi = 2L + 2$ . In summary, the NLO (in  $\alpha_s$ ) QCD corrections to  $hh$  production stem from one-loop diagrams in the leading (in  $d_\chi$ ) EWChL  $\mathcal{L}_2$  and from tree diagrams in the next-to leading part  $\mathcal{L}_4$ . All of these contributions are of chiral dimension  $d_\chi = 4$ . Then, the effective Lagrangian reduces to

$$\mathcal{L} \supset \underbrace{-m_t \left( c_t \frac{h}{v} + c_{tt} \frac{h^2}{v^2} \right) \bar{t}t}_{\mathcal{L}_2} - c_{hhh} \frac{m_h^2}{2v} h^3 + \underbrace{\frac{\alpha_s}{8\pi} \left( c_{ggh} \frac{h}{v} + c_{gggh} \frac{h^2}{v^2} \right) G_{\mu\nu}^a G^{a,\mu\nu}}_{\mathcal{L}_4}. \tag{10.14}$$

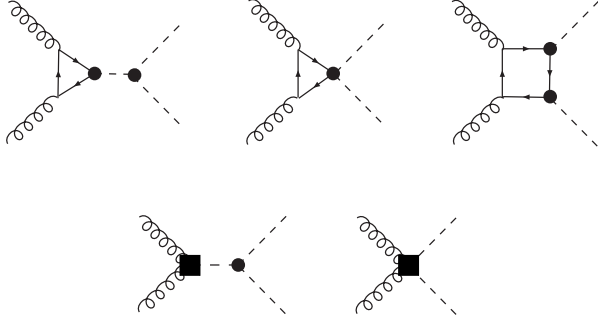


**Figure 10.2:** LO diagrams for the various terms from the EWChL Lagrangian. Both vertices from  $\mathcal{L}_2$  (black dots) and local contact terms from  $\mathcal{L}_4$  (black squares) contribute.

1630     The EWChL introduces five anomalous couplings to the SM and the corresponding  
 1631     LO Feynman diagrams are given in Fig. 10.2.

1632     Diagrams that are of higher chiral dimension (or do not belong to  $\mathcal{O}(\alpha_s^4 \alpha^2)$ ) are sys-  
 1633     tematically neglected, like the ones given in Fig. 10.3. The full virtual amplitude is then  
 1634     given by two-loop contributions (Fig. 10.4), one-loop diagrams that contain one effective  
 1635     coupling from  $\mathcal{L}_4$  (Fig. 10.5), and one tree-diagram containing exactly two effectives  
 1636     vertices between gluons and Higgs bosons (Fig. 10.6). Note that all two-loop diagrams  
 1637     with non-SM values of the Higgs couplings can be retrieved from their SM counterparts  
 1638     by rescaling at amplitude-level:

$$\begin{aligned} \mathcal{M}_V(\Delta_1) &\rightarrow \mathcal{M}_V^{\text{SM}}(\Delta_1) \cdot c_t c_{hh} && (1^{\text{st}} \text{ row in Fig. 10.4}) \\ \mathcal{M}_V(\Delta_2) &\rightarrow \mathcal{M}_V^{\text{SM}}(\Delta_1) \cdot \frac{\hat{s} - m_h^2}{3m_h^2} c_{tt} && (2^{\text{nd}} \text{ row in Fig. 10.4}) \\ \mathcal{M}_V(\square) &\rightarrow \mathcal{M}_V^{\text{SM}}(\square) \cdot c_t^2 && (3^{\text{rd}}, 4^{\text{th}} \text{ rows in Fig. 10.4}), \end{aligned}$$

1639     where  $\mathcal{M}_V(\Delta_1)$  are the triangle diagrams from the 1<sup>st</sup> row of Fig. 10.4,  $\mathcal{M}_V(\Delta_2)$  from  
 1640     the 2<sup>nd</sup> row (given by the corresponding diagrams from the 1<sup>st</sup> row where the  $s$ -channel  
 1641     Higgs propagator gets pinched), and  $\mathcal{M}_V(\square)$  are the box-diagrams from the 3<sup>rd</sup> row.  
 1642     Accordingly, we use the amplitudes computed in Ref. [161] for the pre-sampled set of  
 1643     phase-space points and simply rescale them.

1644     Finally, real-emission diagrams contain five-point one-loop diagrams with SM-like  
 1645     topologies, as well as tree diagrams carrying one effective coupling between gluons and  
 1646     Higgs bosons from  $\mathcal{L}_4$  (Fig. 10.7).

### 1647     10.3 Total cross-sections for BSM benchmark points

1648     All results for total and differential cross-sections presented in this Chapter can be  
 1649     found in Ref. [169]. To summarize, all HTL contributions were computed analytically  
 1650     with FORM. In FT<sub>approx</sub> and in the full theory predictions, the real radiation is provided

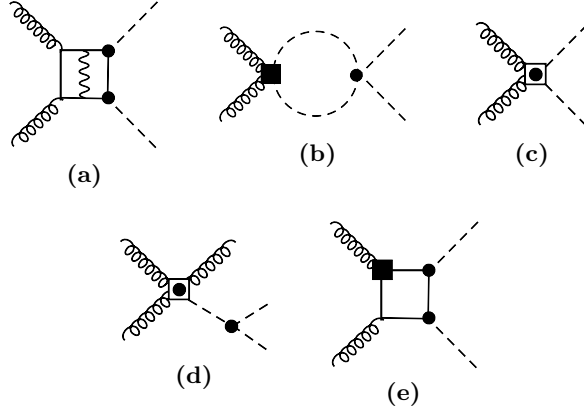


**Figure 10.3:** (a-d) Diagrams that do not scale like  $\alpha_s^4$  are consistently neglected. (e) The chromomagnetic operator  $Q_{ttG} = c_t g_s \bar{t}_L \sigma_{\mu\nu} G^{\mu\nu} t_R$  only contributes at two-loop order at least ( $d_\chi = 6$ ).

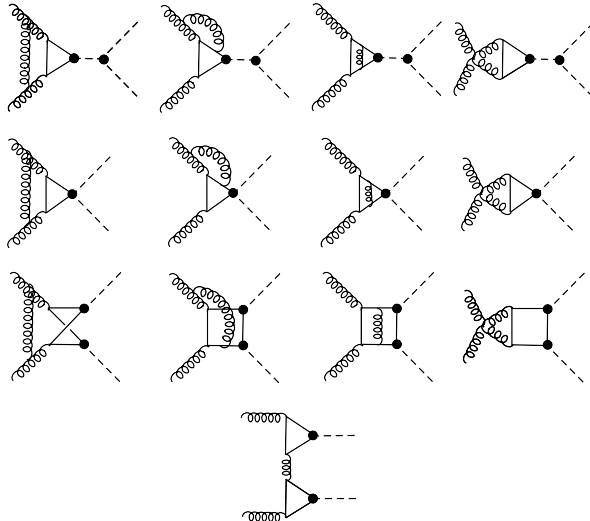


**Figure 10.4:** Two-loop diagrams generated by the EWChL at NLO QCD. They can all be computed by rescaling from the corresponding SM diagrams (see text).

1651 by GoSAM. A UFO model for the EWChL was produced with FEYNRULES [170, 171]  
 1652 and interfaced to GoSAM to produce all tree and one-loop diagrams. The various parts  
 1653 are assembled into a C++ code which performs the phase-space integration with VEGAS  
 1654 as interfaced through the CUBA package.

1655 The results shown below are produced at a center-of-mass energy of  $\sqrt{s} = 14$  TeV,  
 1656 where we use the PDF4LHC15\_nlo\_100\_pdfas interfaced through LHAPDF. The corre-  
 1657 sponding value of  $\alpha_s(\mu)$ , with  $\alpha_s(M_Z) = 0.118$ , is consistently employed throughout the  
 1658 calculation. The Higgs boson and top-quark masses are set to  $m_h = 125$  GeV, respec-

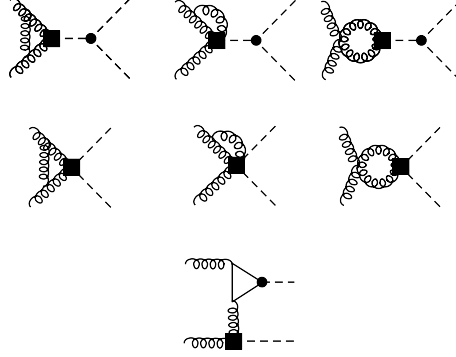


**Figure 10.5:** One-loop virtual contributions at NLO QCD: these diagrams contain exactly one effective contact coupling from  $\mathcal{L}_4$ .

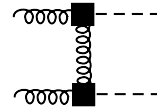


**Figure 10.6:** Tree diagram at NLO QCD containing exactly two effective couplings from  $\mathcal{L}_4$ .

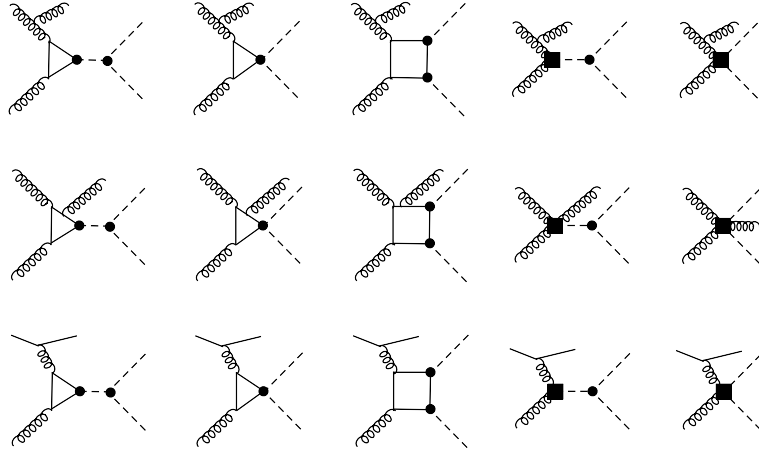


**Figure 10.7:** Real-emission contributions that are either one-loop diagrams without effective contact coupling, or tree diagrams with exactly one such coupling.

tively  $m_t = 173$  GeV, as the two-loop amplitudes were computed with these values, and both their widths are set to zero. Finally, the renormalization and factorization scales are set to  $\mu_R = \mu_F = \mu_0 = m_{hh}/2$  and uncertainties are estimated according to 7-point scale variations  $\mu_{R,F} = c_{R,F}\mu_0$  with  $(c_R, c_F) \in \{0.5, 1, 2\} \times \{0.5, 1, 2\} \setminus \{(0.5, 2), (2, 0.5)\}$ . To characterize the 5-dimensional BSM space, the set of Higgs coupling variations used in the following part is based mostly on the definition of benchmark (BM) points

### 10.3 Total cross-sections for BSM benchmark points

presented in Ref. [172]. There, the BSM space is scanned for different values of the Higgs anomalous couplings and clustered into blocks that manifest a similar behavior in differential distributions. The set of BM points is defined in Table 10.1, and the total cross-sections,  $K$ -factors and uncertainties are shown in Table 10.2.

First, looking at Table 10.1, the NLO cross-sections can become quite sizeable depending on the BM point considered (of order  $\mathcal{O}(100)$  times the SM cross-section), and some are even excluded considering recent bounds on  $hh$  production from experimental limits. With the ATLAS current limit [16] on the observed non-resonant  $hh$  production cross-section of 220 fb at 95% CL, several BM points would indeed be exhausted already. Second, the full  $m_t$ -dependent NLO corrections are important, with  $K$ -factors between 1.66 and 2.34, and are accompanied by large scale uncertainties of  $\mathcal{O}(15 - 20\%)$  (similarly to single Higgs production at NLO QCD [173, 174]). Finally, the  $K$ -factors themselves depend substantially on the considered BSM point. This is also illustrated in Fig. 10.8, where only one parameter is varied at a time. In fact, studies realized in the heavy-top limit suggest the  $K$ -factors's dependence on the different couplings to be quite small [175] (of  $\mathcal{O}(5\%)$  or less for all considered coupling variations). Once full top-quark loop corrections are taken into account, though, the  $K$ -factors for  $c_{hhh}$ ,  $c_{tt}$  and  $c_t$  vary by more than 30% (55% for  $c_{tt}$ ). Later on, in Section 10.4, we will show that this feature is especially prominent around the top-quark pair  $2m_t$  threshold when considering differential distributions.

BM	$c_{hhh}$	$c_t$	$c_{tt}$	$c_{ggh}$	$c_{gggh}$
1	7.5	1.0	-1.0	0.0	0.0
2	1.0	1.0	0.5	$-\frac{1.6}{3}$	-0.2
3	1.0	1.0	-1.5	0.0	$\frac{0.8}{3}$
4	-3.5	1.5	-3.0	0.0	0.0
5	1.0	1.0	0.0	$\frac{1.6}{3}$	$\frac{1.0}{3}$
6	2.4	1.0	0.0	$\frac{0.4}{3}$	$\frac{0.2}{3}$
7	5.0	1.0	0.0	$\frac{0.4}{3}$	$\frac{0.2}{3}$
8a	1.0	1.0	0.5	$\frac{0.8}{3}$	0.0
9	1.0	1.0	1.0	-0.4	-0.2
10	10.0	1.5	-1.0	0.0	0.0
11	2.4	1.0	0.0	$\frac{2.0}{3}$	$\frac{1.0}{3}$
12	15.0	1.0	1.0	0.0	0.0
SM	1.0	1.0	0.0	0.0	0.0

**Table 10.1:** Different BM points in the 5-dimensional Higgs coupling space are analyzed below at inclusive, respectively differential cross-section level.

Furthermore, the ratio of the cross-section to the SM can be parametrized [172, 176] in terms of the anomalous Higgs couplings: the cross-section ratio is expressed as a polynomial whose coefficients correspond to all squared/interference terms from the various diagrams. At LO, this gives 15 possible combinations:

BM	$\sigma_{\text{NLO}} [\text{fb}]$	$K$ -factor	scale uncert. [%]	stat. uncert. [%]	$\frac{\sigma_{\text{NLO}}}{\sigma_{\text{NLO,SM}}}$
$B_1$	194.89	1.88	$^{+19}_{-15}$	1.6	5.915
$B_2$	14.55	1.88	$^{+5}_{-13}$	0.56	0.4416
$B_3$	1047.37	1.98	$^{+21}_{-16}$	0.15	31.79
$B_4$	8922.75	1.98	$^{+19}_{-16}$	0.39	270.8
$B_5$	59.325	1.83	$^{+4}_{-15}$	0.36	1.801
$B_6$	24.69	1.89	$^{+2}_{-11}$	2.1	0.7495
$B_7$	169.41	2.07	$^{+9}_{-12}$	2.2	5.142
$B_{8a}$	41.70	2.34	$^{+6}_{-9}$	0.63	1.266
$B_9$	146.00	2.30	$^{+22}_{-16}$	0.31	4.431
$B_{10}$	575.86	2.00	$^{+17}_{-14}$	3.2	17.48
$B_{11}$	174.70	1.92	$^{+24}_{-8}$	1.2	5.303
$B_{12}$	3618.53	2.07	$^{+16}_{-15}$	1.2	109.83
SM	32.95	1.66	$^{+14}_{-13}$	0.1	1

**Table 10.2:** The total cross-sections for the considered BSM BM points, with their respective  $K$ -factors, scale and (MC) statistical uncertainties, as well as the ratio to the SM cross-section  $\sigma_{\text{NLO,SM}} = 32.95 \text{ fb}$ .

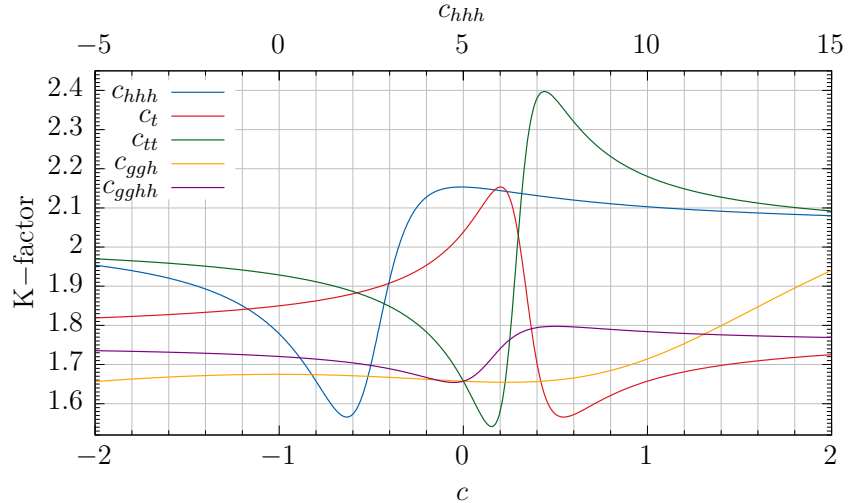


**Figure 10.8:** The  $K$ -factor dependence on the various Higgs anomalous couplings is stronger than suggested previously by HTL computations. Here, the  $K$ -factor is shown as a function of  $c_{hhh}$  on the top axis, and of the other couplings on the lower axis.

$$\begin{aligned}
 \sigma/\sigma_{SM} = & A_1 c_t^4 + A_2 c_{tt}^2 + A_3 c_t^2 c_{hhh}^2 + A_4 c_{ggh}^2 c_{hhh}^2 + A_5 c_{gggh}^2 + A_6 c_{tt} c_t^2 \\
 & + A_7 c_t^3 c_{hhh} + A_8 c_{tt} c_t c_{hhh} + A_9 c_{tt} c_{ggh} c_{hhh} + A_{10} c_{tt} c_{gggh} \\
 & + A_{11} c_t^2 c_{ggh} c_{hhh} + A_{12} c_t^2 c_{gggh} + A_{13} c_t c_{hhh}^2 c_{ggh} \\
 & + A_{14} c_t c_{hhh} c_{gggh} + A_{15} c_{ggh} c_{hhh} c_{gggh}. \tag{10.15}
 \end{aligned}$$

### 10.3 Total cross-sections for BSM benchmark points

1689 The coefficients  $A_1$  to  $A_{15}$  are corrected at NLO, and 8 new coefficients appear from  
 1690 genuine NLO diagrams:

$$\Delta\sigma/\sigma_{SM} = A_{16} c_t^3 c_{ggh} + A_{17} c_t c_{tt} c_{ggh} + A_{18} c_t c_{ggh}^2 c_{hhh} + A_{19} c_t c_{ggh} c_{gghh} \\ + A_{20} c_t^2 c_{ggh}^2 + A_{21} c_{tt} c_{ggh}^2 + A_{22} c_{ggh}^3 c_{hhh} + A_{23} c_{ggh}^2 c_{gghh}. \quad (10.16)$$

1691 These coefficients can be determined by dedicated event generation runs for a set of  
 1692 the 5-dimensional parameter space, and by projecting out a system of equations, or  
 1693 by a simple fit of the polynomial in Eq. (10.16) to the calculated set of cross-sections.  
 1694 The results for the NLO coefficients  $A_1$  to  $A_{23}$  at  $\sqrt{s} = 14$  TeV are given in Table C.1.  
 1695 Interestingly, once the cross-section coefficients are computed, the parametrization given  
 1696 in Eqs. (10.15), (10.16) yields the cross-section for any point in the BSM space. This for  
 1697 example allows to produce iso-contour plots where curves represent configurations in the  
 1698 BSM space which lead to the same cross-section, see Figs. 10.9, 10.10, 10.11. In the  
 1699 latter, two BSM couplings are simultaneously varied (within bounds still approximately  
 1700 allowed by experimental measurements), and iso-curves for the ratio to the SM cross-  
 1701 section at LO (red), respectively NLO (black), are shown.

1702 The cross-section iso-curves are given for  $c_{tt}$  against  $c_{gghh}$  in Fig. 10.9a, respectively  
 1703 against  $c_{ggh}$  in Fig. 10.9b. In both cases, the cross-section varies sizeably with respect  
 1704 to the SM value, and is generally more sensitive to changes in  $c_{tt}$ . The NLO corrections  
 1705 to  $hh$  introduce important shifts in the iso-curves (stemming from the large  $K$ -factors).  
 1706 Fig. 10.10 shows iso-contours for variations of  $c_{hhh}$  versus  $c_{ggh}$ , respectively  $c_{tt}$ . Again,  
 1707 the curves are much more dependent on  $c_{hhh}$  than on the Higgs contact coupling, as  
 1708 exhibited by Fig. 10.10a. In comparison, the dependence of the cross-section on  $c_{hhh}$   
 1709 and  $c_{tt}$  is large, with ratios to the SM cross-section going up to a factor  $\mathcal{O}(\sim 100)$ .  
 1710 Finally, iso-contours are also plotted for simultaneous variations of  $c_t$  versus  $c_{tt}$  and  $c_{hhh}$   
 1711 in Fig. 10.11.

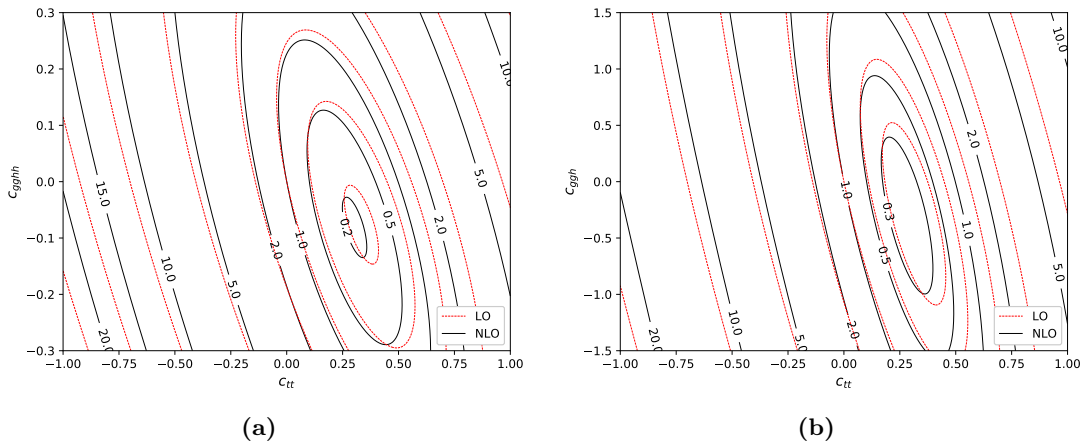


**Figure 10.9:** Iso-contours of  $\sigma/\sigma_{SM}$ : (a)  $c_{gghh}$  and (b)  $c_{ggh}$  versus  $c_{tt}$ .

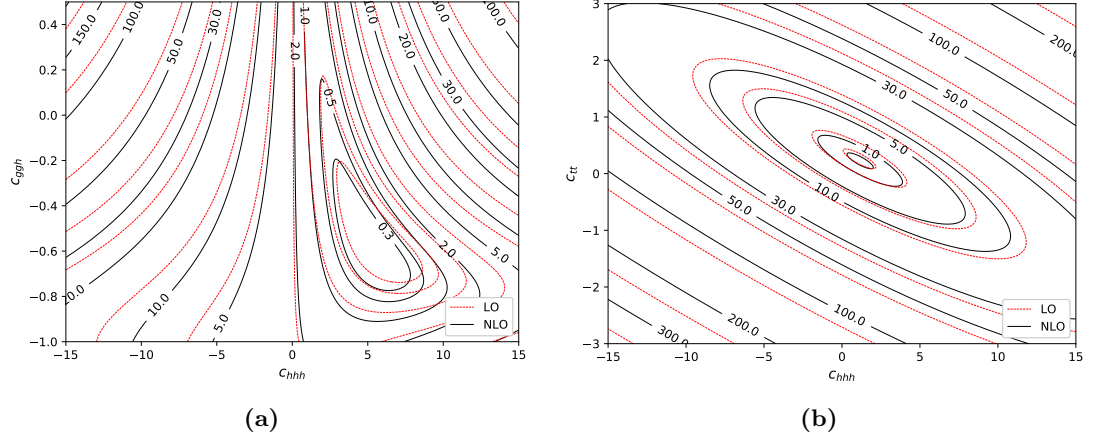


**Figure 10.10:** Iso-contours of  $\sigma/\sigma_{SM}$ : (a)  $c_{ghg}$  and (b)  $c_{tt}$  versus  $c_{hhh}$ .

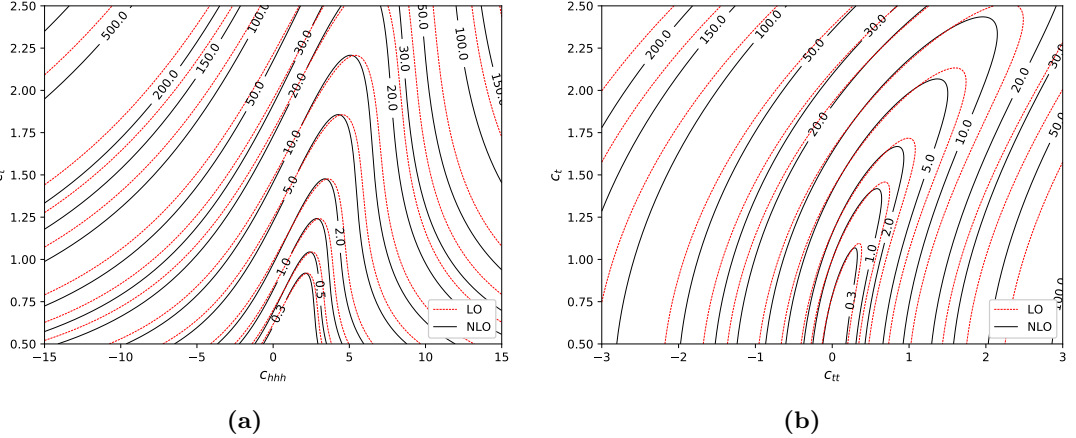


**Figure 10.11:** Iso-contours of  $\sigma/\sigma_{SM}$ : (a)  $c_t$  versus  $c_{hhh}$  and (b)  $c_{tt}$  versus  $c_t$ .

## 10.4 Differential cross-sections and HTL approximations

Next, differential cross-sections are compared for the various approximations laid out in Section 10.1.1. We show distributions of the invariant mass of the Higgs boson pair system  $m_{hh}$  and the transverse momentum of one (any) Higgs  $p_{T,h}$  for a subset of the BM points defined in Table 10.2.

In Fig. 10.12, both distributions are displayed for the BM point 6: the SM distributions are plotted against the the BSM Born-improved,  $FT_{approx}$  and full predictions, respectively, both at LO and NLO. While the  $B_6$  total cross-section is similar to the SM value for all considered NLO approximations, the interference pattern between triangle- and box-like diagrams is very different. The  $m_{hh}$  observable in Fig. 10.12a manifests a

1722 dip around  $m_{hh} = 370 \text{ GeV}$ ,<sup>3</sup> which would be a characteristic sign of BSM physics at  
 1723 the differential level. As a matter of fact, the chosen value of  $c_{hhh} = 2.4$  corresponds  
 1724 approximately to a maximal destructive interference between triangle- and box-like con-  
 1725 tributions when the other couplings are kept fixed at their SM values. Secondly, the  
 1726 differential  $K$ -factor shown in the first ratio plot, which is found to be relatively flat in  
 1727 the usual HTL approximations, varies by more than 70% for the full  $m_t$ -dependent NLO  
 1728 prediction. Finally, while both the Born-improved and FTapprox descriptions show the  
 1729 largest difference to the full NLO calculation around the top-quark pair threshold (see  
 1730 the second ratio plot), they describe the tail of the  $m_{hh}$  distribution rather well. The  
 1731 same considerations apply to the  $p_{T,h}$  distribution plotted in Fig. 10.12b.

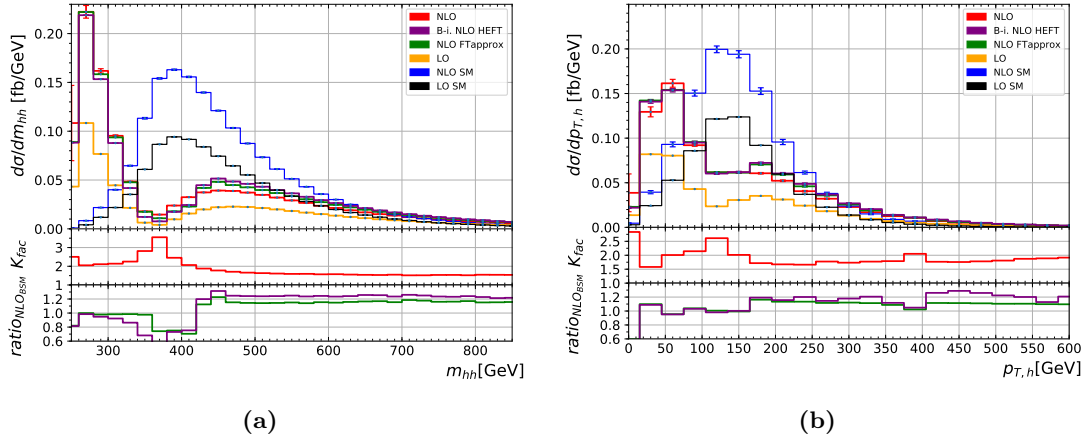


**Figure 10.12:** (a) Higgs boson pair invariant mass and (b) Higgs transverse momentum for BM point 6 ( $c_{hhh} = 2.4, c_t = 1, c_{tt} = 0, c_{ggh} = 2/15, c_{gggh} = 1/15$ ) with all considered  $hh$  production approximations.

1732 The same differential distributions are plotted for the BM point 9 in Fig. 10.13, which  
 1733 is characterized by SM values for  $c_{hhh}$  and  $c_t$  and non-zero values of  $c_{tt}$  and both gluon-  
 1734 Higgs contact couplings  $c_{ggh}$ ,  $c_{gggh}$ . In this case, the cross-section is much larger than  
 1735 the SM value. The anomalous gluon-Higgs coupling values also enhance the tail of both  
 1736 distributions (the dependence of the  $c_{gggh}$  term grows proportionally to the invariant  
 1737  $\hat{s}$  in the limit  $\hat{s} \rightarrow \infty$ ). Again, both NLO approximations fall short of describing the  
 1738 full-theory prediction around the top-quark pair threshold and in the middle-range part  
 1739 of the  $m_{hh}$  distribution.

1740 Renormalization and factorization scale uncertainties are given along the central pre-  
 1741 diction for the BM point 5 in Fig. 10.14. This BM point is one example where, contrary  
 1742 to the SM case, the envelope is not given by the two most extreme scale variations  
 1743  $c_{R,F} \in \{(0.5, 0.5), (2, 2)\}$ , which both give downwards deviations. As for the SM point,  
 1744 the NLO BM prediction is not covered by the LO scale uncertainties. All BM points not  
 1745 shown here are given in Appendix C for completeness.

<sup>3</sup>The LO pure HTL amplitude vanishes at  $m_{hh} = 429 \text{ GeV}$ .

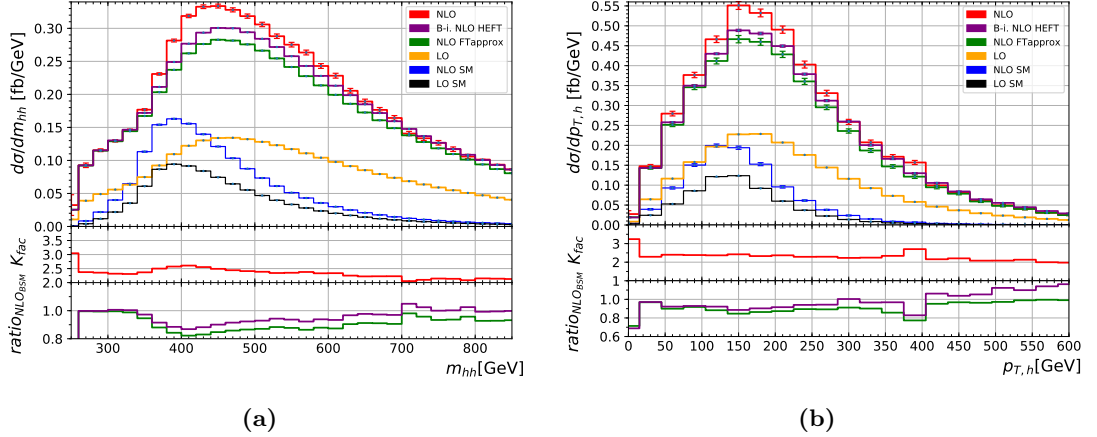


**Figure 10.13:** (a) Higgs boson pair invariant mass and (b) Higgs transverse momentum for BM point 9 ( $c_{hhh} = 1, c_t = 1, c_{tt} = 1, c_{ggh} = -0.4, c_{gghh} = -0.2$ ).

1746 Generally, the full  $m_t$ -dependent NLO prediction introduces a high dependence of  
 1747 the  $K$ -factor on both the anomalous Higgs couplings and at the differential level in  
 1748 distribution bins. For some BM points, the Born-improved and FT<sub>approx</sub> approximations  
 1749 fare rather poorly and should be replaced by the full theory prediction when comparing  
 1750 to experimentally measured cross-sections, for maximal exclusion limits on anomalous  
 1751 couplings. In particular, it should help identify updated BM points in the BSM space of  
 1752 anomalous Higgs couplings. In this prospect, we incorporate part of the EWChL setup  
 1753 presented above into a MC event generator available to experimentalists.

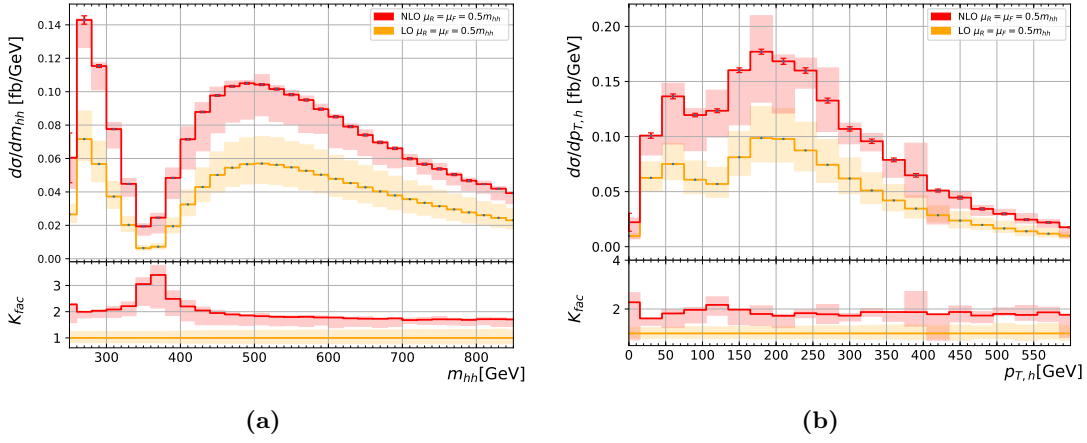


**Figure 10.14:** (a) Higgs boson pair invariant mass and (b) Higgs transverse momentum for BM point 5 ( $c_{hh} = 1, c_t = 1, c_{tt} = 0, c_{ggh} = 8/15, c_{gghh} = 1/3$ ), along with renormalization and factorization scale uncertainties.



# 1754 11 Variations of the triple Higgs-coupling 1755 and parton-shower effects

1756 Having considered the extension of the SM through the EWChL and the effects of the  
1757 full NLO QCD corrections due to the top-quark loops in  $hh$  production, we present its  
1758 implementation in a full-fledged MC event generator. Numerical results and differential  
1759 distributions are given in more detail in Ref. [169]. A version of the  $m_t$ -dependent prediction  
1760 at NLO was already implemented in the case of the SM in the POWHEG-BOX-V2  
1761 package `UserProcesses-V2/ggHH`. We extend it to allow for variations of both the Higgs  
1762 boson trilinear self-coupling  $\lambda$  and the top-Higgs Yukawa coupling  $y_t$ : the result is a public  
1763 MC generator that permits full particle-level production. In particular, Higgs bosons  
1764 are allowed to decay, and the fixed-order calculation can be matched to a parton-shower  
1765 and hadronization package. In this Chapter, we briefly present the working mode of  
1766 the POWHEG-BOX MC generator. The interfacing of the two-loop contribution to  $hh$   
1767 production (including the aforementioned coupling variations) is explained, and NLO  
1768 cross-sections at  $\sqrt{s} = 13, 14, 27$  TeV, as well as differential distributions at  $\sqrt{s} = 14$  TeV  
1769 are shown. Finally, the matching of the fixed-order NLO calculation to a parton-shower  
1770 is studied in more depth, and shower-related systematic uncertainties are estimated.

## 1771 11.1 The Powheg-BOX framework

1772 The POWHEG-BOX framework is a `fortran` MC event generator skeleton that handles  
1773 MC integration and event production for any arbitrary NLO process, supposing the user  
1774 grants the few necessary input ingredients for the calculation, namely a parametrization  
1775 of phase-space and the different contributions to the amplitude. The POWHEG-BOX  
1776 also constitutes a repository of previously calculated processes which are made publicly  
1777 available. In the following, we use the second version of the program POWHEG-BOX-V2.  
1778 The POWHEG formalism bases on the following formula for the hardest emission:

$$d\sigma_{\text{NLO}} = d\Phi_m \bar{B}(\Phi_m) \left( \Delta(p_{T,\min}, \mu^2) + \int_{p_{T,\min}} d\Phi_1 \Delta(p_T, \mu^2) \frac{R(\Phi_{m+1})}{B(\Phi_m)} \Theta(\mu^2 - p_T) \right), \quad (11.1)$$

1779 where  $p_{T,\min}$  is the parton-shower IR cutoff,  $\mu^2$  is the shower starting scale,  $B$  and  
1780  $R$  are the Born, respectively the real-emission matrix-elements and  $\bar{B}$  represents the  
1781 Born underlying configuration. Note that in general, the transverse momentum could  
1782 be replaced by any other shower evolution variable. The function  $\Delta$  is the Sudakov form

1783 factor (see Section 4.2.2) yielding the probability of no-emission above a given scale. In  
 1784 the POWHEG notation,

$$\Delta(t_0, t) = \exp \left( - \int d\Phi_1 \frac{R(\Phi_{m+1})\Theta(t - t_0)}{B(\Phi_m)} \right). \quad (11.2)$$

1785 For more details, the reader is referred to Ref. [18]. The workflow is quite simple and  
 1786 separates into four stages:

- 1787 • An importance sampling grid for the integration is determined: if run in parallel  
 1788 mode, POWHEG generates importance sampling grids for each seed and subse-  
 1789 quently combines them into one and stores the result in a `pwgxgrid.dat` file.
- 1790 • An upper bounding envelope is determined for the underlying Born kinematics  
 1791 cross-section  $\bar{B}$  and stored into a `pwggrid.dat` file.
- 1792 • The upper bound for the normalization of the radiation function  $R(\Phi_{m+1})/B(\Phi_m)$   
 1793 is found, and stored into a `pwgubound.dat` file.
- 1794 • Events can be generated in the LHE format, and run in parallel. Files `pwgevents.lhe`  
 1795 are produced and can then be fed to a parton-shower algorithm later on.

## 1796 11.2 Interfacing two-loop contributions

1797 The grid of pre-sampled phase-space points amplitudes used for producing the results of  
 1798 Chapter 10 is stored and has to be interfaced to POWHEG. As a first point, the program  
 1799 has to be able to call the virtual amplitude at any phase-space point (without having to  
 1800 recompute the expensive two-loop integrals for any possible kinematics  $(\hat{s}, \hat{t})$ ). In the SM  
 1801 `ggHH` program [177], this is handled by setting up a Python interface that interpolates  
 1802 the 2-dimensional grid: first, the  $(\hat{s}, \hat{t})$  phase-space is re-parametrized into new variables  
 1803  $(x, c_\theta)$  to produce an almost uniform distribution of phase-space points. This is achieved  
 1804 by choosing

$$x = f(\beta(\hat{s})), \quad c_\theta = |\cos(\theta)| = \left| \frac{\hat{s} + 2\hat{t} - 2m_h^2}{\hat{s}\beta(\hat{s})} \right|, \quad \beta = \sqrt{1 - \frac{4m_h^2}{\hat{s}}} \quad (11.3)$$

1805 with  $f$  any monotonic function. In this case,  $f(\beta(\hat{s}))$  is chosen to be the cumulative  
 1806 distribution function of the phase-space points generated in Ref. [161]. A uniform grid in  
 1807 the  $(x, c_\theta)$  space is generated, and the result at each point is set by linearly interpolating  
 1808 the amplitude using the neighbouring points computed by `SECDEC`. The amplitude at  
 1809 any phase-space points is then interpolated using the Clough-Tougher scheme in `SciPy`,  
 1810 which allows for a high numerical stability. For details on the grid performance and  
 1811 caveats, the reader is referred to Ref. [177].

1812 The implementation of variations of the Higgs trilinear self-coupling  $\lambda$  bases on a  
 1813 simple observation: at all orders (in QCD), the full amplitude for di-Higgs production  
 1814 is a second-order polynomial in  $\lambda$ ,

$$M_\lambda \equiv |\mathcal{M}_\lambda|^2 = A + B \lambda + C \lambda^2 . \quad (11.4)$$

1815 Thus knowing the amplitude for three values of  $\lambda$  allows to interpolate the matrix-  
 1816 element to any other arbitrary value. In our case, grids of the virtual amplitudes are  
 1817 produced for  $\lambda \in \{-1, 0, 1\}$ . Before starting the POWHEG run, the three grids are  
 1818 combined to a new grid containing the virtual amplitude for the user-given value of the  
 1819 Higgs self-coupling by simple Lagrange interpolation,

$$M_\lambda = M_0 (1 - \lambda^2) + \frac{M_1}{2} (\lambda + \lambda^2) + \frac{M_{-1}}{2} (-\lambda + \lambda^2) , \quad (11.5)$$

1820 where the uncertainties on the three amplitudes are added in quadrature. This grid is  
 1821 then further propagated to the Clough-Tougher interpolation routine. Note that in the  
 1822 BSM case, we also include points at 100 TeV in the grid to further improve statistics  
 1823 at higher center-of-mass energies, and by extension, in distribution tails. On the other  
 1824 hand, because BSM distributions differ in shape from the SM case (for example, see  
 1825 Fig. 11.2), phase-space regions that could well be populated for certain values of the  
 1826 anomalous couplings are not always well-sampled by the SM grid.

## 1827 11.3 Total and differential cross-sections at fixed-order

1828 We use the PDF4LHC15\_nlo\_30\_pdfas set interfaced to POWHEG-BOX-V2 through  
 1829 LHAPDF. Jets are clustered by the anti- $k_T$  algorithm [178] from **FastJet**, with a jet  
 1830 radius parameter of  $R = 0.4$  and a minimum transverse momentum  $p_{T,\min}^{\text{jet}} = 20 \text{ GeV}$ .  
 1831 Otherwise, the same setup presented in Section 10.3 is used for the next results. Note  
 1832 that the nomenclature is different, with respect to Chapter 10, for variations of the Higgs  
 1833 trilinear coupling and the top-Higgs Yukawa coupling: the Higgs self-coupling ratio to  
 1834 the SM value, formerly called  $c_{hhh}$ , is replaced by  $\kappa_\lambda$  (in reference to the widely-used  
 1835 experimental  $\kappa$  framework), and the top-Higgs Yukawa coupling ratio  $c_t$  is now named  
 1836  $y_t$ .

1837 Total cross-sections for various values of  $\kappa_\lambda = \lambda/\lambda_{\text{SM}}$  were computed for  $\sqrt{s} = 13, 14$   
 1838 and 27 TeV and are displayed in Table 11.1. Note again that the cross-section has a  
 1839 minimum around  $\kappa_\lambda \sim 2.4$ , for which the interference between triangle- and box-like  
 1840 diagrams is at its most destructive. The  $K$ -factor is plotted in Fig. 11.1 as a function  
 1841 of the Higgs self-coupling, this time ranging over the full, not yet excluded region for  $\kappa_\lambda$ .

1842 The distribution of the invariant mass of the Higgs boson pair  $hh$  is shown for the  
 1843 considered values of  $\kappa_\lambda$  in Fig. 11.2 with their respective scale uncertainties. For values  
 1844 of  $\kappa_\lambda$  that lead to minimal cross-section, the interference pattern is well-recognizable  
 1845 with a dip around  $m_{hh} \sim 350 \text{ GeV}$ , near the top-pair threshold. For greater values of  
 1846  $|\kappa_\lambda|$ , this dip completely disappears and the enhanced triangle-like contribution tends  
 1847 to populate the lower  $m_{hh}$ -region. A similar behavior is observed for the transverse  
 1848 momentum of one (any) Higgs boson, as presented in Fig. 11.3, although the effect is  
 1849 partly washed out.

## 11 Variations of the triple Higgs-coupling and parton-shower effects

$\lambda_{\text{BSM}}/\lambda_{\text{SM}}$	$\sigma_{\text{NLO}}@13\text{TeV} [\text{fb}]$	$\sigma_{\text{NLO}}@14\text{TeV} [\text{fb}]$	$\sigma_{\text{NLO}}@27\text{TeV} [\text{fb}]$	K-factor@14TeV
-1	$116.71^{+16.4\%}_{-14.3\%}$	$136.91^{+16.4\%}_{-13.9\%}$	504.9	1.86
0	$62.51^{+15.8\%}_{-13.7\%}$	$73.64^{+15.4\%}_{-13.4\%}$	275.29	1.79
1	$27.84^{+11.6\%}_{-12.9\%}$	$32.88^{+13.5\%}_{-12.5\%}$	$127.7^{+11.5\%}_{-10.4\%}$	1.66
2	$12.42^{+13.1\%}_{-12.0\%}$	$14.75^{+12.0\%}_{-11.8\%}$	59.10	1.56
2.4	$11.65^{+13.9\%}_{-12.7\%}$	$13.79^{+13.5\%}_{-12.5\%}$	53.67	1.65
3	$16.28^{+16.2\%}_{-15.3\%}$	$19.07^{+17.1\%}_{-14.1\%}$	69.84	1.90
5	$81.74^{+20.0\%}_{-15.6\%}$	$95.22^{+19.7\%}_{-11.5\%}$	330.61	2.14

**Table 11.1:** The cross-sections for di-Higgs production at full NLO QCD are given for  $\sqrt{s} = 13, 14$  and  $27 \text{ TeV}$  with scale uncertainties for several values of  $\kappa_\lambda = \lambda/\lambda_{\text{SM}}$ .

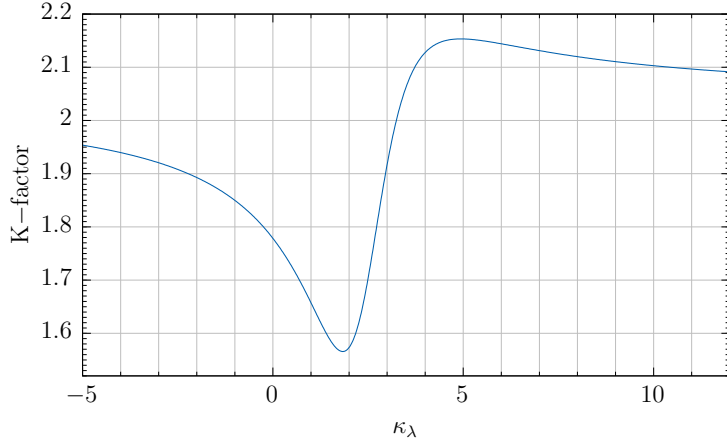


**Figure 11.1:** The  $K$ -factor is largely dependent on the value of  $\kappa_\lambda$  especially once the  $m_t$ -dependent NLO QCD corrections are taken into account.

Furthermore, variations of the top-Higgs Yukawa coupling  $y_t$  can be recovered by a trick: allowing for  $y_t$  variations changes Eq. (11.4) into

$$|\mathcal{M}|^2 = y_t^4 \left[ \mathcal{M}_B \mathcal{M}_B^* + \frac{\lambda}{y_t} (\mathcal{M}_B \mathcal{M}_T^* + \mathcal{M}_T \mathcal{M}_B^*) + \frac{\lambda^2}{y_t^2} \mathcal{M}_T \mathcal{M}_T^* \right], \quad (11.6)$$

where  $\mathcal{M}_B$  is the box- and  $\mathcal{M}_T$  is the triangle contribution, and only the ratio  $\frac{\lambda}{y_t}$  appears up to an overall factor. So, it suffices to generate events with the value of  $\lambda$  corresponding to the desired value of the ratio  $\frac{\lambda}{y_t}$ , and finally rescale all results by  $y_t^4$ . For example, to produce results for  $\kappa_\lambda = 1, y_t = 0.8$ , the cross-section is given by

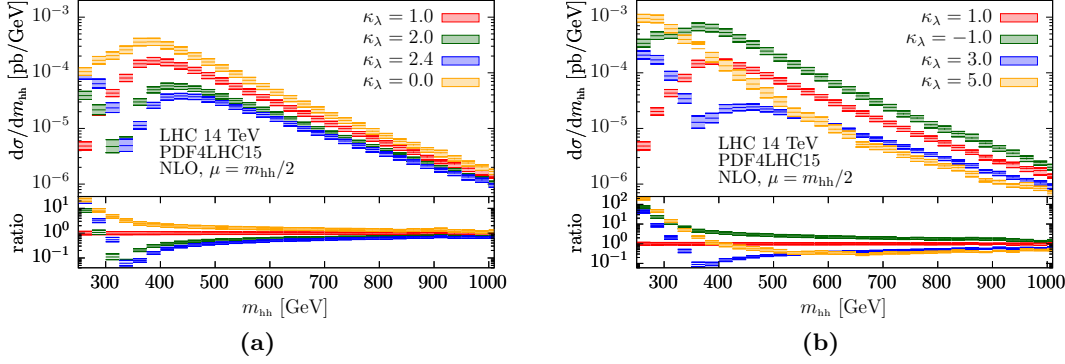


**Figure 11.2:** The Higgs boson pair invariant mass distributions for different values of  $\kappa_\lambda$  are given at  $\sqrt{s} = 14$  TeV.

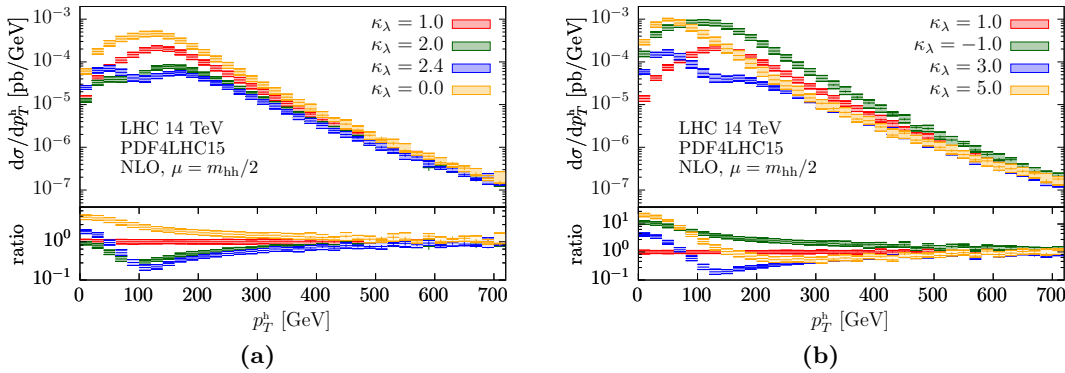


**Figure 11.3:** The transverse momentum of one (any) Higgs boson is shown for several values of  $\kappa_\lambda$  at  $\sqrt{s} = 14$  TeV.

$$d\sigma_{\text{NLO}}(\kappa_\lambda = 1, y_t = 0.8) = (0.8)^4 \cdot d\sigma_{\text{NLO}} \left( y_t = 1, \kappa_\lambda = \frac{1}{0.8} = 1.25 \right). \quad (11.7)$$

1856 Both  $m_{hh}$  and  $p_T^h$  distributions are displayed for  $y_t$ -values close to the currently ex-  
1857 cluded region in Fig. 11.4.

## 11.4 Parton-shower matched predictions at NLO

1859 To be used by experimentalists for full simulation, the fixed-order calculation is matched  
1860 to a parton-shower (whose final-state can also be hadronized later on) within POWHEG.  
1861 In the fourth generation stage presented above, POWHEG generates full parton-level  
1862 events and stores them in LHE files. These can then be used as input to most modern  
1863 parton-shower programs. For our purposes, two different parton-shower programs are

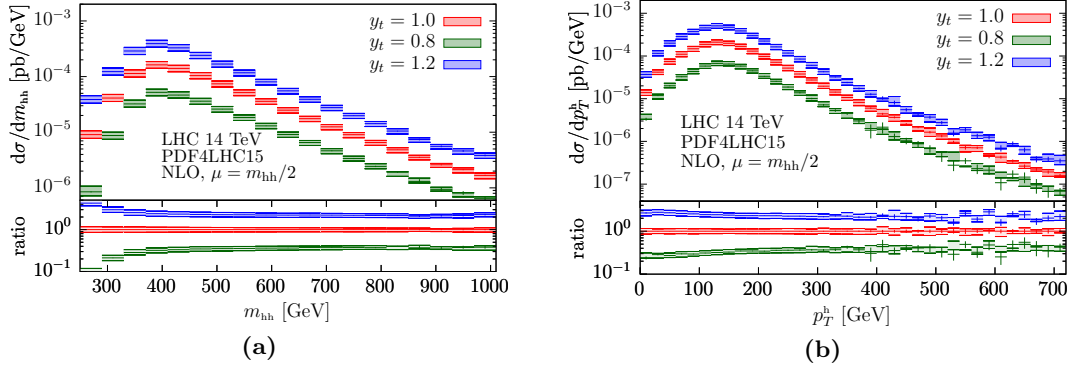


**Figure 11.4:** The framework also allows for variations of the top-Higgs Yukawa coupling  $y_t$ . The invariant mass of the Higgs boson pair system and the transverse momentum of one Higgs boson are shown for three values of  $y_t$  for good measure. The procedure for generating  $y_t$ -varied events is explained in the text.

employed, namely **Pythia** 8.235 and **Herwig** 7.1.4. Additionally, both the angular-ordered (so called  $\tilde{q}$ ) and the dipole shower algorithms present in **Herwig** are applied. The interfacing of both programs to POWHEG is mostly automatized: we use the standard **UserHooks** based on the **main31** LHE showering routine from **Pythia** to set the shower  $p_T$  definitions and vetoes (see Appendix D). For **Herwig** 7, a process-independent interface library is present since revision r3591 of the POWHEG-BOX-V2 which sets the **LHEReader** class and handles the **Herwig** output for the event analysis. Finally, in both showers, we leave the tunes to their default values. Note that the Sudakov form factor is automatically included by POWHEG when producing LHE files. The POWHEG  $h_{\text{damp}}$  parameter is kept fixed throughout the next Section and set to  $h_{\text{damp}} = 250$  GeV.

In Fig. 11.5a, the transverse momentum of one (any) Higgs boson  $p_T^h$  is shown for the fixed-order NLO prediction, as well as the matched predictions to the three different shower algorithms: **Pythia** 8 (PP8), and both the angular-ordered  $\tilde{q}$  shower (PH7- $\tilde{q}$ ) and the dipole shower (PH7-dipole) from **Herwig**. For variables that are inclusive in the additional radiation, like  $p_T^h$ , all predictions are very much identical. In the case of variables that are sensitive to real emission, like the angular distance of both Higgs bosons  $\Delta R^{hh} = \sqrt{(\eta_1 - \eta_2)^2 + (\phi_1 - \phi_2)^2}$  shown in Fig. 11.5b, the showered predictions differ from the NLO calculation. There, the Sudakov exponent effectively resums radiation around  $\Delta R^{hh} = \pi$ , where the Higgs bosons are close to a back-to-back configuration. In addition, the parton-shower starts populating the region  $\Delta R^{hh} < \pi$ . Also, differences between the **Pythia** and **Herwig** parton-showers are already visible: while both **Herwig** showers produce very similar results, **Pythia** overshoots their prediction by  $\sim 50\%$ .

The differences between both parton-shower programs become more obvious when considering the transverse momentum of the Higgs boson pair system  $p_T^{hh}$ , displayed in Fig. 11.6 for two values of the Higgs trilinear coupling  $\kappa_\lambda = 1$ ,  $\kappa_\lambda = 2.4$ . In that case, both **Pythia** and **Herwig** agree at low transverse momentum, until they start to deviate at  $p_T^{hh} \sim 100$  GeV already. Then, while both **Herwig** showers correctly reproduce the

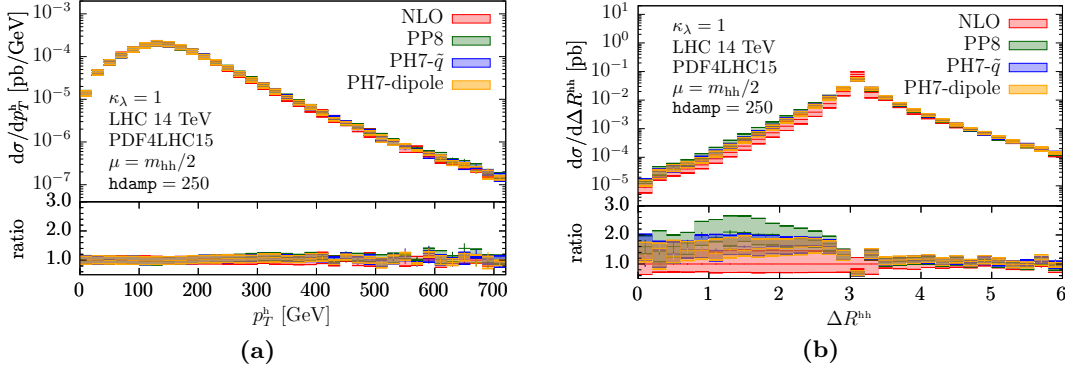


**Figure 11.5:** For the SM case  $\kappa_\lambda = 1$ , (a) the transverse momentum of one Higgs boson, and (b) the angular distance between both Higgs bosons are shown for the fixed-order NLO case, as well as for the three different parton-shower algorithms. The parton-level events from POWHEG are matched to Pythia 8 (PP8), and to both the angular-ordered  $\tilde{q}$ -shower (PH7- $\tilde{q}$ ) and the dipole shower (PH7-dipole) from Herwig 7.

1891 hard NLO emission in the high- $p_T^{hh}$  region, the Pythia parton-shower produces much  
 1892 harder radiation and its ratio to the fixed-order prediction stagnates at  $\sim 2$  over the  
 1893 remaining range. The harder spectrum from Pythia was found to be due to too hard  
 1894 sub-leading jets produced solely in the shower [179] as compared to the older Pythia 6  
 1895 parton-shower in di-Higgs production. In other processes, like  $t\bar{t}$  production, sizeable  
 1896 differences between Pythia and Herwig had also already been observed [180].

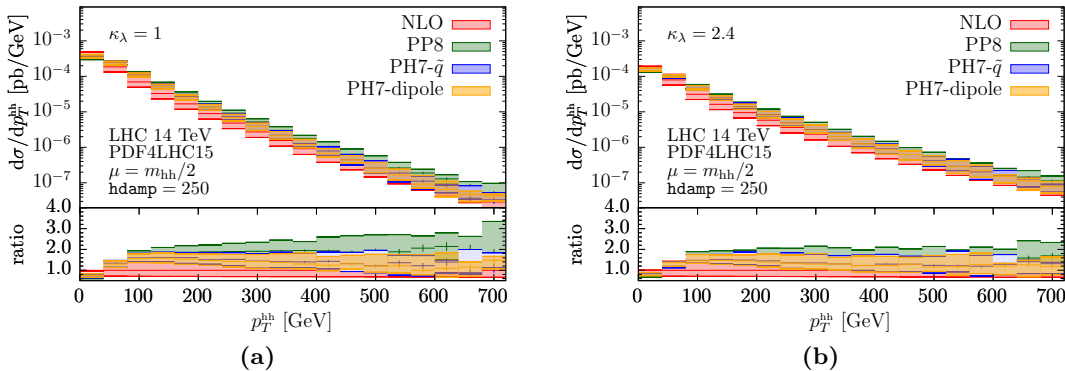


**Figure 11.6:** The NLO fixed-order prediction is compared to results from the three parton-shower algorithms with respect to the transverse momentum of the Higgs boson pair system  $p_T^{hh}$  for (a)  $\kappa_\lambda = 1$  and (b)  $\kappa_\lambda = 2.4$ .

1897 As a way to estimate shower-matching uncertainties, the maximal tranverse momentum  
 1898 allowed for shower emissions can be set in Herwig by varying the so-called hard scale  
 1899  $\mu_Q$ . The parameter `HardScaleFactor` is varied to  $c_Q = 0.5$ ,  $c_Q = 2$  and applied on the

1900 central hard shower scale separately for the up- and down-variations of the renormalization  
 1901 and factorization scales  $\mu_{R,F}$ . In Fig. 11.7, the result is presented for the di-Higgs  
 1902 transverse momentum  $p_T^{hh}$  and the angular separation between the Higgs bosons  $\Delta R^{hh}$ .  
 1903 The shower scale variations add to the renormalization/factorizations scale uncertainties,  
 1904 bringing their common envelope to a corresponding 50% – 100% overall systematic  
 1905 uncertainty in the far- $p_T^{hh}$  region of the distribution. The differences between the cen-  
 1906 tral Pythia and Herwig predictions are then partly covered by the hard shower scale  
 1907 variations.

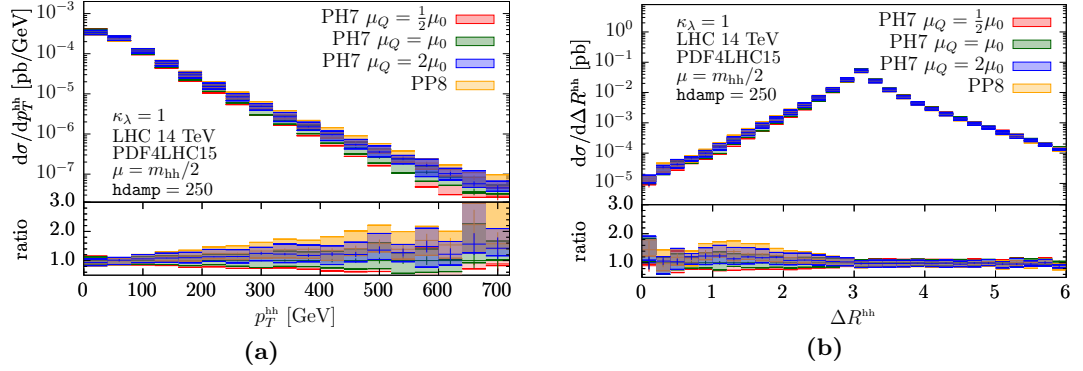


**Figure 11.7:** (a) The di-Higgs transverse momentum  $p_T^{hh}$  and (b) the angular separation  $\Delta R^{hh}$  between the Higgs bosons are shown for variations of the **Herwig** hard shower scale, which regulates the maximal allowed transverse momentum of shower emissions. The hard scale  $\mu_Q = c_Q \mu_0$  is varied by  $c_Q \in \{\frac{1}{2}, 2\}$  with respect to the default scale  $\mu_0$ .

1908 All in all, considering both scale and parton-shower uncertainties, the Higgs pair  
 1909 process underlines the necessity of computing higher-order corrections in both fixed-order  
 1910 and resummation accuracy. In the future, it will be informative to study parton-shower  
 1911 (as well as other non-perturbative, e.g. hadronization) modeling effects in loop-induced  
 1912 color singlet production and try and reduce the sizeable associated uncertainties.

<sup>1913</sup> **12 Conclusion & Outlook**



# 1914 Bibliography

- 1915 [1] PARTICLE DATA GROUP collaboration, *Review of particle physics*, *Phys. Rev. D* 1916 **98** (2018) 030001.
- 1917 [2] CDF collaboration, *Observation of Top Quark Production in  $\bar{p}p$  Collisions with* 1918 *the Collider Detector at Fermilab*, *Phys. Rev. Lett.* **74** (1995) 2626.
- 1919 [3] D0 collaboration, *Observation of the top quark*, *Phys. Rev. Lett.* **74** (1995) 2632.
- 1920 [4] “Lhc top working group.”
- 1921 <https://twiki.cern.ch/twiki/bin/view/LHCPhysics/LHCTopWG>.
- 1922 [5] ATLAS collaboration, *Measurement of the top quark mass in the  $t\bar{t} \rightarrow$*
- 1923 *lepton+jets channel from  $\sqrt{s} = 8$  TeV ATLAS data and combination with*
- 1924 *previous results*, *Submitted to: Eur. Phys. J.* (2018) [[1810.01772](#)].
- 1925 [6] CMS collaboration, *Measurement of the top quark mass using proton-proton data* 1926 *at  $\sqrt{(s)} = 7$  and 8 TeV*, *Phys. Rev.* **D93** (2016) 072004 [[1509.04044](#)].
- 1927 [7] P. Marquard, A. V. Smirnov, V. A. Smirnov and M. Steinhauser, *Quark Mass* 1928 *Relations to Four-Loop Order in Perturbative QCD*, *Phys. Rev. Lett.* **114** (2015)
- 1929 **142002** [[1502.01030](#)].
- 1930 [8] M. Beneke and V. M. Braun, *Heavy quark effective theory beyond perturbation* 1931 *theory: Renormalons, the pole mass and the residual mass term*, *Nucl. Phys.* 1932 **B426** (1994) 301 [[hep-ph/9402364](#)].
- 1933 [9] I. I. Y. Bigi, M. A. Shifman, N. G. Uraltsev and A. I. Vainshtein, *The Pole mass* 1934 *of the heavy quark. Perturbation theory and beyond*, *Phys. Rev.* **D50** (1994) 2234 1935 [[hep-ph/9402360](#)].
- 1936 [10] M. Beneke, *More on ambiguities in the pole mass*, *Phys. Lett.* **B344** (1995) 341 1937 [[hep-ph/9408380](#)].
- 1938 [11] A. H. Hoang, C. Lepenik and M. Preisser, *On the Light Massive Flavor* 1939 *Dependence of the Large Order Asymptotic Behavior and the Ambiguity of the* 1940 *Pole Mass*, *JHEP* **09** (2017) 099 [[1706.08526](#)].
- 1941 [12] A. H. Hoang and I. W. Stewart, *Top Mass Measurements from Jets and the* 1942 *Tevatron Top-Quark Mass*, *Nucl. Phys. Proc. Suppl.* **185** (2008) 220 [[0808.0222](#)].

## Bibliography

- 1943 [13] A. H. Hoang, S. Plätzer and D. Samitz, *On the Cutoff Dependence of the Quark  
1944 Mass Parameter in Angular Ordered Parton Showers*, *JHEP* **10** (2018) 200  
1945 [[1807.06617](#)].
- 1946 [14] ATLAS COLLABORATION collaboration, *Combined measurements of Higgs boson  
1947 production and decay using up to 80 fb<sup>-1</sup> of proton–proton collision data at  $\sqrt{s} =$   
1948 13 TeV collected with the ATLAS experiment*, Tech. Rep.  
1949 ATLAS-CONF-2018-031, CERN, Geneva, Jul, 2018.
- 1950 [15] CMS COLLABORATION collaboration, *Combined measurements of the Higgs  
1951 boson’s couplings at  $\sqrt{s} = 13$  TeV*, Tech. Rep. CMS-PAS-HIG-17-031, CERN,  
1952 Geneva, 2018.
- 1953 [16] ATLAS collaboration, *Combination of searches for Higgs boson pairs in pp  
1954 collisions at 13 TeV with the ATLAS experiment.*, Tech. Rep.  
1955 ATLAS-CONF-2018-043, CERN, Geneva, Sep, 2018.
- 1956 [17] P. Nason, *A New method for combining NLO QCD with shower Monte Carlo  
1957 algorithms*, *JHEP* **11** (2004) 040 [[hep-ph/0409146](#)].
- 1958 [18] S. Frixione, P. Nason and C. Oleari, *Matching NLO QCD computations with  
1959 Parton Shower simulations: the POWHEG method*, *JHEP* **11** (2007) 070  
1960 [[0709.2092](#)].
- 1961 [19] S. Alioli, P. Nason, C. Oleari and E. Re, *A general framework for implementing  
1962 NLO calculations in shower Monte Carlo programs: the POWHEG BOX*, *JHEP*  
1963 **06** (2010) 043 [[1002.2581](#)].
- 1964 [20] S. L. Glashow, *The renormalizability of vector meson interactions*, *Nuclear  
1965 Physics* **10** (1959) 107 .
- 1966 [21] S. Weinberg, *A model of leptons*, *Phys. Rev. Lett.* **19** (1967) 1264.
- 1967 [22] A. Salam and J. C. Ward, *Weak and electromagnetic interactions*, *Il Nuovo  
1968 Cimento (1955-1965)* **11** (1959) 568.
- 1969 [23] ATLAS collaboration, *Standard Model Summary Plots Spring 2019*, Tech. Rep.  
1970 ATL-PHYS-PUB-2019-010, CERN, Geneva, Mar, 2019.
- 1971 [24] F. Englert and R. Brout, *Broken symmetry and the mass of gauge vector mesons*,  
1972 *Phys. Rev. Lett.* **13** (1964) 321.
- 1973 [25] P. W. Higgs, *Broken symmetries and the masses of gauge bosons*, *Phys. Rev.  
1974 Lett.* **13** (1964) 508.
- 1975 [26] G. S. Guralnik, C. R. Hagen and T. W. B. Kibble, *Global conservation laws and  
1976 massless particles*, *Phys. Rev. Lett.* **13** (1964) 585.

## Bibliography

- [27] J. Bardeen, L. N. Cooper and J. R. Schrieffer, *Theory of superconductivity*, *Phys. Rev.* **108** (1957) 1175.
- [28] LHC HIGGS CROSS SECTION WORKING GROUP collaboration, *Handbook of LHC Higgs Cross Sections: 4. Deciphering the Nature of the Higgs Sector*, [1610.07922].
- [29] K. G. Chetyrkin and M. F. Zoller, *Three-loop  $\beta$ -functions for top-yukawa and the higgs self-interaction in the standard model*, *Journal of High Energy Physics* **2012** (2012) 33.
- [30] S. Chigusa, T. Moroi and Y. Shoji, *State-of-the-Art Calculation of the Decay Rate of Electroweak Vacuum in the Standard Model*, *Phys. Rev. Lett.* **119** (2017) 211801.
- [31] G. Degrassi, S. Di Vita, J. Elias-Miró, J. R. Espinosa, G. F. Giudice, G. Isidori et al., *Higgs mass and vacuum stability in the Standard Model at NNLO*, *Journal of High Energy Physics* **2012** (2012) 98.
- [32] A. V. Bednyakov, B. A. Kniehl, A. F. Pikelner and O. L. Veretin, *Stability of the electroweak vacuum: Gauge independence and advanced precision*, *Phys. Rev. Lett.* **115** (2015) 201802.
- [33] SUPER-KAMIOKANDE collaboration, *Evidence for oscillation of atmospheric neutrinos*, *Phys. Rev. Lett.* **81** (1998) 1562.
- [34] F. Borzumati, Y. Grossman, E. Nardi and Y. Nir, *Neutrino masses and mixing in supersymmetric models without R parity*, *Phys. Lett.* **B384** (1996) 123 [hep-ph/9606251].
- [35] N. Haba, M. Matsuda and M. Tanimoto, *Large neutrino flavor mixings and gauge mediated supersymmetry breaking scenario*, *Phys. Lett.* **B478** (2000) 351 [hep-ph/9911511].
- [36] M. D. Schwartz, *Quantum Field Theory and the Standard Model*. Cambridge University Press, 2014.
- [37] H. B. G. Casimir, *On the Attraction Between Two Perfectly Conducting Plates*, *Indag. Math.* **10** (1948) 261.
- [38] G. 't Hooft and M. Veltman, *Regularization and renormalization of gauge fields*, *Nuclear Physics B* **44** (1972) 189 .
- [39] G. Passarino and M. Veltman, *One-loop corrections for e+e annihilation into + in the Weinberg model*, *Nuclear Physics B* **160** (1979) 151 .
- [40] A. Denner and S. Dittmaier, *Reduction schemes for one-loop tensor integrals*, *Nucl. Phys.* **B734** (2006) 62 [hep-ph/0509141].

## Bibliography

- 2012 [41] J. M. Campbell, E. W. N. Glover and D. J. Miller, *One loop tensor integrals in  
2013 dimensional regularization*, *Nucl. Phys.* **B498** (1997) 397 [[hep-ph/9612413](#)].
- 2014 [42] J. Fleischer, F. Jegerlehner and O. V. Tarasov, *Algebraic reduction of one loop  
2015 Feynman graph amplitudes*, *Nucl. Phys.* **B566** (2000) 423 [[hep-ph/9907327](#)].
- 2016 [43] A. I. Davydychev, *A Simple formula for reducing Feynman diagrams to scalar  
2017 integrals*, *Phys. Lett.* **B263** (1991) 107.
- 2018 [44] C. G. Callan, *Broken scale invariance in scalar field theory*, *Phys. Rev. D* **2**  
2019 (1970) 1541.
- 2020 [45] K. Symanzik, *Small distance behaviour in field theory and power counting*,  
2021 *Communications in Mathematical Physics* **18** (1970) 227.
- 2022 [46] K. Symanzik, *Small-distance-behaviour analysis and wilson expansions*,  
2023 *Communications in Mathematical Physics* **23** (1971) 49.
- 2024 [47] A. D. Martin, W. J. Stirling, R. S. Thorne and G. Watt, *Parton distributions for  
2025 the LHC*, *The European Physical Journal C* **63** (2009) 189.
- 2026 [48] T. Hahn, *Cuba—a library for multidimensional numerical integration*, *Computer  
2027 Physics Communications* **168** (2005) 78 .
- 2028 [49] G. P. Lepage, *A new algorithm for adaptive multidimensional integration*,  
2029 *Journal of Computational Physics* **27** (1978) 192 .
- 2030 [50] J. H. Friedman and M. H. Wright, *A nested partitioning procedure for numerical  
2031 multiple integration*, *ACM Trans. Math. Softw.* **7** (1981) 76.
- 2032 [51] W. H. Press and G. R. Farrar, *Recursive stratified sampling for multidimensional  
2033 monte carlo integration*, *Computers in Physics* **4** (1990) 190  
2034 [<https://aip.scitation.org/doi/pdf/10.1063/1.4822899>].
- 2035 [52] J. Berntsen, T. O. Espelid and A. Genz, *An adaptive algorithm for the  
2036 approximate calculation of multiple integrals*, *ACM Trans. Math. Softw.* **17**  
2037 (1991) 437.
- 2038 [53] A. Buckley, J. Ferrando, S. Lloyd, K. Nordström, B. Page, M. Rüfenacht et al.,  
2039 *Lhapdf6: parton density access in the lhc precision era*, *The European Physical  
2040 Journal C* **75** (2015) 132.
- 2041 [54] Z. Nagy, *Next-to-leading order calculation of three-jet observables in  
2042 hadron-hadron collisions*, *Phys. Rev. D* **68** (2003) 094002.
- 2043 [55] J. M. Campbell, R. K. Ellis and W. T. Giele, *A multi-threaded version of mcfm*,  
2044 *The European Physical Journal C* **75** (2015) 246.

- 2045 [56] J. Alwall, R. Frederix, S. Frixione, V. Hirschi, F. Maltoni, O. Mattelaer et al.,  
 2046 *The automated computation of tree-level and next-to-leading order differential*  
 2047 *cross sections, and their matching to parton shower simulations, Journal of High*  
 2048 *Energy Physics* **2014** (2014) 79.
- 2049 [57] F. Caccioli, P. Maierhöfer and S. Pozzorini, *Scattering amplitudes with open*  
 2050 *loops, Phys. Rev. Lett.* **108** (2012) 111601.
- 2051 [58] F. Buccioni, S. Pozzorini and M. Zoller, *On-the-fly reduction of open loops, The*  
 2052 *European Physical Journal C* **78** (2018) 70.
- 2053 [59] G. Cullen, N. Greiner, G. Heinrich, G. Luisoni, P. Mastrolia, G. Ossola et al.,  
 2054 *Automated one-loop calculations with GoSam, The European Physical Journal C*  
 2055 **72** (2012) 1889.
- 2056 [60] G. Cullen, H. van Deurzen, N. Greiner, G. Heinrich, G. Luisoni, P. Mastrolia  
 2057 et al., *GoSam-2.0: a tool for automated one-loop calculations within the Standard*  
 2058 *Model and beyond, The European Physical Journal C* **74** (2014) 3001.
- 2059 [61] S. Badger, B. Biedermann, P. Uwer and V. Yundin, *Numerical evaluation of*  
 2060 *virtual corrections to multi-jet production in massless qcd, Computer Physics*  
 2061 *Communications* **184** (2013) 1981 .
- 2062 [62] K. Arnold, M. Bähr, G. Bozzi, F. Campanario, C. Englert, T. Figy et al.,  
 2063 *VBFNLO: A parton level Monte Carlo for processes with electroweak bosons,*  
 2064 *Computer Physics Communications* **180** (2009) 1661 .
- 2065 [63] J. Baglio et al., *VBFNLO: A Parton Level Monte Carlo for Processes with*  
 2066 *Electroweak Bosons – Manual for Version 2.7.0, [1107.4038].*
- 2067 [64] J. Baglio et al., *Release Note - VBFNLO 2.7.0, [1404.3940].*
- 2068 [65] F. Campanario, T. M. Figy, S. Plätzer and M. Sjödahl, *Electroweak Higgs Boson*  
 2069 *Plus Three Jet Production at Next-to-Leading-Order QCD, Phys. Rev. Lett.* **111**  
 2070 (2013) 211802.
- 2071 [66] T. Binoth, F. Boudjema, G. Dissertori, A. Lazopoulos, A. Denner, S. Dittmaier  
 2072 et al., *A proposal for a standard interface between Monte Carlo tools and*  
 2073 *one-loop programs, Computer Physics Communications* **181** (2010) 1612 .
- 2074 [67] S. Alioli, S. Badger, J. Bellm, B. Biedermann, F. Boudjema, G. Cullen et al.,  
 2075 *Update of the Binoth Les Houches Accord for a standard interface between Monte*  
 2076 *Carlo tools and one-loop programs, Computer Physics Communications* **185**  
 2077 (2014) 560 .
- 2078 [68] P. Nogueira, *Automatic Feynman Graph Generation, Journal of Computational*  
 2079 *Physics* **105** (1993) 279 .
- 2080 [69] J. A. M. Vermaasen, *New features of FORM, [math-ph/0010025].*

## Bibliography

- 2081 [70] T. Peraro, *Ninja: Automated integrand reduction via laurent expansion for*  
2082 *one-loop amplitudes*, *Computer Physics Communications* **185** (2014) 2771 .
- 2083 [71] G. Cullen, J.-P. Guillet, G. Heinrich, T. Kleinschmidt, E. Pilon, T. Reiter et al.,  
2084 *Golem95C: A library for one-loop integrals with complex masses*, *Computer*  
2085 *Physics Communications* **182** (2011) 2276 .
- 2086 [72] J. P. Guillet, G. Heinrich and J. F. von Soden-Fraunhofen, *Tools for NLO*  
2087 *automation: extension of the Golem95C integral library*, *Comput. Phys.*  
2088 *Commun.* **185** (2014) 1828 [[1312.3887](#)].
- 2089 [73] P. Mastrolia, G. Ossola, T. Reiter and F. Tramontano, *Scattering Amplitudes*  
2090 *from Unitarity-based Reduction Algorithm at the Integrand-level*, *JHEP* **08**  
2091 (2010) 080 [[1006.0710](#)].
- 2092 [74] R. K. Ellis and G. Zanderighi, *Scalar one-loop integrals for QCD*, *JHEP* **02**  
2093 (2008) 002 [[0712.1851](#)].
- 2094 [75] A. van Hameren, *Oneloop: For the evaluation of one-loop scalar functions*,  
2095 *Computer Physics Communications* **182** (2011) 2427 .
- 2096 [76] G. Altarelli and G. Parisi, *Asymptotic Freedom in Parton Language*, *Nucl. Phys.*  
2097 **B126** (1977) 298.
- 2098 [77] Y. L. Dokshitzer, *Calculation of the Structure Functions for Deep Inelastic*  
2099 *Scattering and e+ e- Annihilation by Perturbation Theory in Quantum*  
2100 *Chromodynamics.*, *Sov. Phys. JETP* **46** (1977) 641.
- 2101 [78] V. N. Gribov and L. N. Lipatov, *Deep inelastic e p scattering in perturbation*  
2102 *theory*, *Sov. J. Nucl. Phys.* **15** (1972) 438.
- 2103 [79] M. Dasgupta, F. A. Dreyer, K. Hamilton, P. F. Monni and G. P. Salam,  
2104 *Logarithmic accuracy of parton showers: a fixed-order study*, *JHEP* **09** (2018)  
2105 033 [[1805.09327](#)].
- 2106 [80] M. Bahr et al., *Herwig++ Physics and Manual*, *Eur. Phys. J.* **C58** (2008) 639  
2107 [[0803.0883](#)].
- 2108 [81] J. Bellm et al., *Herwig 7.0/Herwig++ 3.0 release note*, *Eur. Phys. J.* **C76** (2016)  
2109 196 [[1512.01178](#)].
- 2110 [82] S. Frixione and B. R. Webber, *Matching NLO QCD computations and parton*  
2111 *shower simulations*, *Journal of High Energy Physics* **2002** (2002) 029.
- 2112 [83] S. Frixione, P. Nason and C. Oleari, *Matching NLO QCD computations with*  
2113 *parton shower simulations: the POWHEG method*, *Journal of High Energy*  
2114 *Physics* **2007** (2007) 070.

- 2115 [84] T. Sjostrand, S. Mrenna and P. Z. Skands, *PYTHIA 6.4 Physics and Manual*,  
 2116 *JHEP* **05** (2006) 026 [[hep-ph/0603175](#)].
- 2117 [85] T. Sjostrand, S. Mrenna and P. Z. Skands, *A Brief Introduction to PYTHIA 8.1*,  
 2118 *Comput. Phys. Commun.* **178** (2008) 852 [[0710.3820](#)].
- 2119 [86] T. Gleisberg, S. Hoeche, F. Krauss, M. Schonherr, S. Schumann, F. Siegert et al.,  
 2120 *Event generation with SHERPA 1.1*, *JHEP* **02** (2009) 007 [[0811.4622](#)].
- 2121 [87] B. Andersson, G. Gustafson, G. Ingelman and T. Sjöstrand, *Parton  
 2122 fragmentation and string dynamics*, *Physics Reports* **97** (1983) 31 .
- 2123 [88] T. Sjöstrand, S. Ask, J. R. Christiansen, R. Corke, N. Desai, P. Ilten et al., *An  
 2124 introduction to PYTHIA 8.2*, *Computer Physics Communications* **191** (2015) 159  
 2125 .
- 2126 [89] A. Kupco, *Cluster hadronization in HERWIG 5.9*, in *Monte Carlo generators for  
 2127 HERA physics. Proceedings, Workshop, Hamburg, Germany, 1998-1999*,  
 2128 pp. 292–300, 1998, [[hep-ph/9906412](#)].
- 2129 [90] S. Gieseke, F. Loshaj and P. Kirchgæßer, *Soft and diffractive scattering with the  
 2130 cluster model in Herwig*, *The European Physical Journal C* **77** (2017) 156.
- 2131 [91] D. Amati and G. Veneziano, *Preconfinement as a property of perturbative qcd*,  
 2132 *Physics Letters B* **83** (1979) 87 .
- 2133 [92] ATLAS collaboration, *Performance of the atlas trigger system in 2010*, *The  
 2134 European Physical Journal C* **72** (2012) 1849.
- 2135 [93] ATLAS collaboration, *The Run-2 ATLAS Trigger System*, *J. Phys. Conf. Ser.*  
 2136 **762** (2016) 012003.
- 2137 [94] ATLAS collaboration, *Measurement of the top quark mass with the template  
 2138 method in the  $t\bar{t} \rightarrow$  lepton + jets channel using ATLAS data*, *The European  
 2139 Physical Journal C* **72** (2012) 2046.
- 2140 [95] ATLAS collaboration, *Measurement of the top quark mass in the  $t\bar{t} \rightarrow$   
 2141 lepton+jets and  $t\bar{t} \rightarrow$  dilepton channels using  $\sqrt{s} = 7$  TeV ATLAS data*, *The  
 2142 European Physical Journal C* **75** (2015) 330.
- 2143 [96] ATLAS collaboration, *Measurement of the  $t\bar{t}$  production cross-section using  $e\mu$   
 2144 events with b-tagged jets in pp collisions at  $\sqrt{s} = 7$  and 8TeV with the ATLAS  
 2145 detector*, *The European Physical Journal C* **74** (2014) 3109.
- 2146 [97] ATLAS collaboration, *Measurement of the top quark mass in the  $t\bar{t}$  dilepton  
 2147 channel from  $\sqrt{s} = 8$ TeV ATLAS data*, *Physics Letters B* **761** (2016) 350 .
- 2148 [98] ATLAS collaboration, *Measurement of lepton differential distributions and the  
 2149 top quark mass in  $t\bar{t}$  production in pp collisions at  $\sqrt{s} = 8$ TeV with the ATLAS  
 2150 detector*, *The European Physical Journal C* **77** (2017) 804.

## Bibliography

- 2151 [99] ATLAS collaboration, *Determination of the top-quark pole mass using  $t\bar{t}$  + 1-jet*  
2152 *events collected with the ATLAS experiment in 7 TeV pp collisions*, *Journal of*  
2153 *High Energy Physics* **2015** (2015) 121.
- 2154 [100] ATLAS collaboration, *Measurement of the top-quark mass in the fully hadronic*  
2155 *decay channel from ATLAS data at  $\sqrt{s} = 7$  TeV*, *The European Physical Journal*  
2156 *C* **75** (2015) 158.
- 2157 [101] ATLAS collaboration, *Top-quark mass measurement in the all-hadronic  $t\bar{t}$  decay*  
2158 *channel at  $\sqrt{s} = 8$  TeV with the ATLAS detector*, *Journal of High Energy*  
2159 *Physics* **2017** (2017) 118.
- 2160 [102] M. Czakon and A. Mitov, *Top++: A Program for the Calculation of the*  
2161 *Top-Pair Cross-Section at Hadron Colliders*, *Comput. Phys. Commun.* **185**  
2162 (2014) 2930 [[1112.5675](#)].
- 2163 [103] ATLAS collaboration, *Studies on top-quark Monte Carlo modelling for Top2016*,  
2164 *Tech. Rep. ATL-PHYS-PUB-2016-020*, CERN, Geneva, Sep, 2016.
- 2165 [104] ATLAS collaboration, *Studies on top-quark Monte Carlo modelling with Sherpa*  
2166 *and MG5\_aMC@NLO*, *Tech. Rep. ATL-PHYS-PUB-2017-007*, CERN, Geneva,  
2167 May, 2017.
- 2168 [105] ATLAS collaboration, *Investigation of systematic uncertainties on the*  
2169 *measurement of the top-quark mass using lepton transverse momenta*, *Tech. Rep.*  
2170 *ATL-PHYS-PUB-2018-001*, CERN, Geneva, Feb, 2018.
- 2171 [106] ATLAS collaboration, *Improvements in  $t\bar{t}$  modelling using NLO+PS Monte*  
2172 *Carlo generators for Run2*, *Tech. Rep. ATL-PHYS-PUB-2018-009*, CERN,  
2173 Geneva, Jul, 2018.
- 2174 [107] J. M. Campbell, R. K. Ellis, P. Nason and E. Re, *Top-pair production and decay*  
2175 *at NLO matched with parton showers*, *JHEP* **04** (2015) 114 [[1412.1828](#)].
- 2176 [108] M. Czakon, D. Heymes and A. Mitov, *High-precision differential predictions for*  
2177 *top-quark pairs at the LHC*, *Phys. Rev. Lett.* **116** (2016) 082003 [[1511.00549](#)].
- 2178 [109] M. Czakon, D. Heymes and A. Mitov, *Dynamical scales for multi-TeV top-pair*  
2179 *production at the LHC*, *JHEP* **04** (2017) 071 [[1606.03350](#)].
- 2180 [110] M. Czakon, D. Heymes and A. Mitov, *fastNLO tables for NNLO top-quark pair*  
2181 *differential distributions*, [[1704.08551](#)].
- 2182 [111] M. Czakon, D. Heymes, A. Mitov, D. Pagani, I. Tsinikos and M. Zaro, *Top-pair*  
2183 *production at the LHC through NNLO QCD and NLO EW*, *JHEP* **10** (2017) 186  
2184 [[1705.04105](#)].

- 2185 [112] W. Hollik and D. Pagani, *The electroweak contribution to the top quark  
2186 forward-backward asymmetry at the Tevatron*, *Phys. Rev.* **D84** (2011) 093003  
2187 [1107.2606].
- 2188 [113] J. H. Kühn, A. Scharf and P. Uwer, *Weak Interactions in Top-Quark Pair  
2189 Production at Hadron Colliders: An Update*, *Phys. Rev.* **D91** (2015) 014020  
2190 [1305.5773].
- 2191 [114] D. Pagani, I. Tsirikos and M. Zaro, *The impact of the photon PDF and  
2192 electroweak corrections on  $t\bar{t}$  distributions*, *Eur. Phys. J.* **C76** (2016) 479  
2193 [1606.01915].
- 2194 [115] W. Bernreuther, A. Brandenburg, Z. G. Si and P. Uwer, *Top quark pair  
2195 production and decay at hadron colliders*, *Nucl. Phys.* **B690** (2004) 81  
2196 [hep-ph/0403035].
- 2197 [116] K. Melnikov and M. Schulze, *NLO QCD corrections to top quark pair production  
2198 and decay at hadron colliders*, *JHEP* **0908** (2009) 049 [0907.3090].
- 2199 [117] J. M. Campbell and R. K. Ellis, *Top-quark processes at NLO in production and  
2200 decay*, *J. Phys.* **G42** (2015) 015005 [1204.1513].
- 2201 [118] M. Brucherseifer, F. Caola and K. Melnikov,  $\mathcal{O}(\alpha_s^2)$  corrections to  
2202 *fully-differential top quark decays*, *JHEP* **04** (2013) 059 [1301.7133].
- 2203 [119] J. Gao and A. S. Papanastasiou, *Top-quark pair-production and decay at high  
2204 precision*, *Phys. Rev.* **D96** (2017) 051501 [1705.08903].
- 2205 [120] M. Beneke, P. Falgari, S. Klein and C. Schwinn, *Hadronic top-quark pair  
2206 production with NNLL threshold resummation*, *Nucl. Phys.* **B855** (2012) 695  
2207 [1109.1536].
- 2208 [121] M. Cacciari, M. Czakon, M. Mangano, A. Mitov and P. Nason, *Top-pair  
2209 production at hadron colliders with next-to-next-to-leading logarithmic soft-gluon  
2210 resummation*, *Phys. Lett.* **B710** (2012) 612 [1111.5869].
- 2211 [122] A. Ferroglia, S. Marzani, B. D. Pecjak and L. L. Yang, *Boosted top production:  
2212 factorization and resummation for single-particle inclusive distributions*, *JHEP*  
2213 **01** (2014) 028 [1310.3836].
- 2214 [123] A. Broggio, A. S. Papanastasiou and A. Signer, *Renormalization-group improved  
2215 fully differential cross sections for top pair production*, *JHEP* **10** (2014) 98  
2216 [1407.2532].
- 2217 [124] N. Kidonakis, *High-order threshold corrections for top-pair and single-top  
2218 production*, in *Proceedings, Meeting of the APS Division of Particles and Fields  
2219 (DPF 2015): Ann Arbor, Michigan, USA, 4-8 Aug 2015*, 2015, [1509.07848].

## Bibliography

- 2220 [125] B. D. Pecjak, D. J. Scott, X. Wang and L. L. Yang, *Resummed differential cross*  
2221 *sections for top-quark pairs at the LHC*, *Phys. Rev. Lett.* **116** (2016) 202001  
2222 [[1601.07020](#)].
- 2223 [126] M. L. Czakon et al., *Top quark pair production at NNLO+NNLL' in QCD*  
2224 *combined with electroweak corrections*, in *11th International Workshop on Top*  
2225 *Quark Physics (TOP2018) Bad Neuenahr, Germany, September 16-21, 2018*,  
2226 2019, [[1901.08281](#)].
- 2227 [127] G. Heinrich, A. Maier, R. Nisius, J. Schlenk and J. Winter, *NLO QCD*  
2228 *corrections to  $W^+W^-b\bar{b}$  production with leptonic decays in the light of top quark*  
2229 *mass and asymmetry measurements*, *JHEP* **1406** (2014) 158 [[1312.6659](#)].
- 2230 [128] S. Frixione, E. Laenen, P. Motylinski, B. R. Webber and C. D. White, *Single-top*  
2231 *hadroproduction in association with a W boson*, *JHEP* **07** (2008) 029  
2232 [[0805.3067](#)].
- 2233 [129] A. Denner, S. Dittmaier, S. Kallweit and S. Pozzorini, *NLO QCD corrections to*  
2234  *$WWb\bar{b}$  production at hadron colliders*, *Phys. Rev. Lett.* **106** (2011) 052001  
2235 [[1012.3975](#)].
- 2236 [130] A. Denner, S. Dittmaier, S. Kallweit and S. Pozzorini, *NLO QCD corrections to*  
2237 *off-shell top-antitop production with leptonic decays at hadron colliders*, *JHEP* **10**  
2238 (2012) 110 [[1207.5018](#)].
- 2239 [131] G. Bevilacqua, M. Czakon, A. van Hameren, C. G. Papadopoulos and M. Worek,  
2240 *Complete off-shell effects in top quark pair hadroproduction with leptonic decay at*  
2241 *next-to-leading order*, *JHEP* **02** (2011) 083 [[1012.4230](#)].
- 2242 [132] R. Frederix, *Top Quark Induced Backgrounds to Higgs Production in the*  
2243  *$WW^{(*)} \rightarrow ll\nu\nu$  Decay Channel at Next-to-Leading-Order in QCD*, *Phys. Rev.*  
2244 *Lett.* **112** (2014) 082002 [[1311.4893](#)].
- 2245 [133] F. Cascioli, S. Kallweit, P. Maierhöfer and S. Pozzorini, *A unified NLO*  
2246 *description of top-pair and associated  $Wt$  production*, *Eur. Phys. J.* **C74** (2014)  
2247 2783 [[1312.0546](#)].
- 2248 [134] A. Denner and M. Pellen, *Off-shell production of top-antitop pairs in the*  
2249 *lepton+jets channel at NLO QCD*, *JHEP* **02** (2018) 013 [[1711.10359](#)].
- 2250 [135] G. Heinrich, A. Maier, R. Nisius, J. Schlenk and J. Winter, *NLO QCD corrections*  
2251 *to  $WWb\bar{b}$  production with leptonic decays in the light of top quark mass and*  
2252 *asymmetry measurements*, *Journal of High Energy Physics* **2014** (2014) 158.
- 2253 [136] A. Denner, S. Dittmaier, S. Kallweit and S. Pozzorini, *NLO QCD corrections to*  
2254 *off-shell top-antitop production with leptonic decays at hadron colliders*, *Journal*  
2255 *of High Energy Physics* **2012** (2012) 110.

- 2256 [137] ATLAS collaboration, *Measurement of the top quark mass in the  $t\bar{t} \rightarrow$  dilepton*  
 2257 *channel from  $\sqrt{s} = 8$  TeV ATLAS data*, *Phys. Lett.* **B761** (2016) 350  
 2258 [[1606.02179](#)].
- 2259 [138] M. Cacciari and G. P. Salam, *Dispelling the  $N^3$  myth for the  $k_t$  jet-finder*, *Phys.*  
 2260 *Lett.* **B641** (2006) 57 [[hep-ph/0512210](#)].
- 2261 [139] M. Cacciari, G. P. Salam and G. Soyez, *FastJet User Manual*, *Eur. Phys. J.* **C72**  
 2262 (2012) 1896 [[1111.6097](#)].
- 2263 [140] S. Höche, J. Huang, G. Luisoni, M. Schönherr and J. Winter, *Zero and one jet*  
 2264 *combined next-to-leading order analysis of the top quark forward-backward*  
 2265 *asymmetry*, *Phys. Rev.* **D88** (2013) 014040 [[1306.2703](#)].
- 2266 [141] A. Buckley, J. Butterworth, L. Lonnblad, D. Grellscheid, H. Hoeth, J. Monk  
 2267 et al., *Rivet user manual*, *Comput. Phys. Commun.* **184** (2013) 2803 [[1003.0694](#)].
- 2268 [142] G. Heinrich, A. Maier, R. Nisius, J. Schlenk, M. Schulze, L. Scyboz et al., *NLO*  
 2269 *and off-shell effects in top quark mass determinations*, *JHEP* **07** (2018) 129  
 2270 [[1709.08615](#)].
- 2271 [143] C. G. Lester and D. J. Summers, *Measuring masses of semiinvisibly decaying*  
 2272 *particles pair produced at hadron colliders*, *Phys. Lett.* **B463** (1999) 99  
 2273 [[hep-ph/9906349](#)].
- 2274 [144] A. Barr, C. Lester and P. Stephens,  *$m(T2)$ : The Truth behind the glamour*, *J.*  
 2275 *Phys.* **G29** (2003) 2343 [[hep-ph/0304226](#)].
- 2276 [145] V. Blobel, *An Unfolding method for high-energy physics experiments*, in *Advanced*  
 2277 *Statistical Techniques in Particle Physics. Proceedings, Conference, Durham,*  
 2278 *UK, March 18-22, 2002*, pp. 258–267, 2002, [[hep-ex/0208022](#)],  
 2279 <http://www.ippp.dur.ac.uk/Workshops/02/statistics/proceedings//blobel2.pdf>.
- 2280 [146] GEANT4 collaboration, *GEANT4: A Simulation toolkit*, *Nucl. Instrum. Meth.*  
 2281 **A506** (2003) 250.
- 2282 [147] E. Richter-Was, D. Froidevaux and L. Poggioli, *ATLFAST 2.0 a fast simulation*  
 2283 *package for ATLAS*, .
- 2284 [148] ATLAS collaboration, *Observation of a new particle in the search for the*  
 2285 *Standard Model Higgs boson with the ATLAS detector at the LHC*, *Phys. Lett.*  
 2286 **B716** (2012) 1 [[1207.7214](#)].
- 2287 [149] CMS collaboration, *Observation of a new boson at a mass of 125 GeV with the*  
 2288 *CMS experiment at the LHC*, *Phys. Lett.* **B716** (2012) 30 [[1207.7235](#)].
- 2289 [150] E. W. N. Glover and J. J. van der Bij, *Higgs Boson Pair Production via Gluon*  
 2290 *Fusion*, *Nucl. Phys.* **B309** (1988) 282.

## Bibliography

- 2291 [151] M. Spira, A. Djouadi, D. Graudenz and P. M. Zerwas, *Higgs boson production at  
2292 the LHC*, *Nucl. Phys.* **B453** (1995) 17 [[hep-ph/9504378](#)].
- 2293 [152] R. Bonciani, A. Ferroglio, P. Mastrolia, E. Remiddi and J. J. van der Bij,  
2294 *Two-loop  $N(F)=1$  QED Bhabha scattering differential cross section*, *Nucl. Phys.*  
2295 **B701** (2004) 121 [[hep-ph/0405275](#)].
- 2296 [153] C. Anastasiou, S. Beerli, S. Bucherer, A. Daleo and Z. Kunszt, *Two-loop  
2297 amplitudes and master integrals for the production of a Higgs boson via a massive  
2298 quark and a scalar-quark loop*, *JHEP* **01** (2007) 082 [[hep-ph/0611236](#)].
- 2299 [154] G. Degrassi, P. P. Giardino and R. Gröber, *On the two-loop virtual QCD  
2300 corrections to Higgs boson pair production in the Standard Model*, *Eur. Phys. J.*  
2301 **C76** (2016) 411 [[1603.00385](#)].
- 2302 [155] R. Bonciani, V. Del Duca, H. Frellesvig, J. M. Henn, F. Moriello and V. A.  
2303 Smirnov, *Next-to-leading order QCD corrections to the decay width  $H \rightarrow Z$* , *JHEP*  
2304 **08** (2015) 108 [[1505.00567](#)].
- 2305 [156] T. Gehrmann, S. Guns and D. Kara, *The rare decay  $H \rightarrow Z\gamma$  in perturbative  
2306 QCD*, *JHEP* **09** (2015) 038 [[1505.00561](#)].
- 2307 [157] R. Gröber, A. Maier and T. Rauh, *Reconstruction of top-quark mass effects in  
2308 Higgs pair production and other gluon-fusion processes*, *JHEP* **03** (2018) 020  
2309 [[1709.07799](#)].
- 2310 [158] R. Bonciani, G. Degrassi, P. P. Giardino and R. Gröber, *Analytical Method for  
2311 Next-to-Leading-Order QCD Corrections to Double-Higgs Production*, *Phys. Rev.*  
2312 *Lett.* **121** (2018) 162003 [[1806.11564](#)].
- 2313 [159] G. Mishima, *High-Energy Expansion of Two-Loop Massive Four-Point Diagrams*,  
2314 *JHEP* **02** (2019) 080 [[1812.04373](#)].
- 2315 [160] J. Davies, G. Mishima, M. Steinhauser and D. Wellmann, *Double Higgs boson  
2316 production at NLO in the high-energy limit: complete analytic results*, *JHEP* **01**  
2317 (2019) 176 [[1811.05489](#)].
- 2318 [161] S. Borowka, N. Greiner, G. Heinrich, S. P. Jones, M. Kerner, J. Schlenk et al.,  
2319 *Full top quark mass dependence in Higgs boson pair production at NLO*, *JHEP*  
2320 **10** (2016) 107 [[1608.04798](#)].
- 2321 [162] A. von Manteuffel and C. Studerus, *Reduze 2 - Distributed Feynman Integral  
2322 Reduction*, [[1201.4330](#)].
- 2323 [163] J. Carter and G. Heinrich, *SecDec: A general program for sector decomposition*,  
2324 *Comput. Phys. Commun.* **182** (2011) 1566 [[1011.5493](#)].

- 2325 [164] S. Borowka, J. Carter and G. Heinrich, *Numerical Evaluation of Multi-Loop*  
 2326 *Integrals for Arbitrary Kinematics with SecDec 2.0*, *Comput. Phys. Commun.*  
 2327 **184** (2013) 396 [[1204.4152](#)].
- 2328 [165] S. Borowka, G. Heinrich, S. P. Jones, M. Kerner, J. Schlenk and T. Zirke,  
 2329 *SecDec-3.0: numerical evaluation of multi-scale integrals beyond one loop*,  
 2330 *Comput. Phys. Commun.* **196** (2015) 470 [[1502.06595](#)].
- 2331 [166] S. P. Jones, *Automation of 2-loop Amplitude Calculations*, *PoS LL2016* (2016)  
 2332 069 [[1608.03846](#)].
- 2333 [167] G. Buchalla, O. Catà and C. Krause, *Complete Electroweak Chiral Lagrangian*  
 2334 *with a Light Higgs at NLO*, *Nucl. Phys.* **B880** (2014) 552 [[1307.5017](#)].
- 2335 [168] G. Buchalla, O. Catá and C. Krause, *On the Power Counting in Effective Field*  
 2336 *Theories*, *Phys. Lett.* **B731** (2014) 80 [[1312.5624](#)].
- 2337 [169] G. Buchalla, M. Capozi, A. Celis, G. Heinrich and L. Scyboz, *Higgs boson pair*  
 2338 *production in non-linear Effective Field Theory with full  $m_t$ -dependence at NLO*  
 2339 *QCD*, *JHEP* **09** (2018) 057 [[1806.05162](#)].
- 2340 [170] A. Alloul, N. D. Christensen, C. Degrande, C. Duhr and B. Fuks, *FeynRules 2.0 -*  
 2341 *A complete toolbox for tree-level phenomenology*, *Comput. Phys. Commun.* **185**  
 2342 (2014) 2250 [[1310.1921](#)].
- 2343 [171] N. D. Christensen and C. Duhr, *FeynRules - Feynman rules made easy*, *Comput.*  
 2344 *Phys. Commun.* **180** (2009) 1614 [[0806.4194](#)].
- 2345 [172] A. Carvalho, M. Dall’Osso, T. Dorigo, F. Goertz, C. A. Gottardo and M. Tosi,  
 2346 *Higgs Pair Production: Choosing Benchmarks With Cluster Analysis*, *JHEP* **04**  
 2347 (2016) 126 [[1507.02245](#)].
- 2348 [173] A. Djouadi, M. Spira and P. Zerwas, *Production of Higgs bosons in proton*  
 2349 *colliders. QCD corrections*, *Physics Letters B* **264** (1991) 440 .
- 2350 [174] S. Dawson, *Radiative corrections to Higgs boson production*, *Nucl. Phys.* **B359**  
 2351 (1991) 283.
- 2352 [175] R. Grober, M. Muhlleitner, M. Spira and J. Streicher, *NLO QCD Corrections to*  
 2353 *Higgs Pair Production including Dimension-6 Operators*, *JHEP* **09** (2015) 092  
 2354 [[1504.06577](#)].
- 2355 [176] A. Azatov, R. Contino, G. Panico and M. Son, *Effective field theory analysis of*  
 2356 *double Higgs boson production via gluon fusion*, *Phys. Rev.* **D92** (2015) 035001  
 2357 [[1502.00539](#)].
- 2358 [177] G. Heinrich, S. P. Jones, M. Kerner, G. Luisoni and E. Vryonidou, *NLO*  
 2359 *predictions for Higgs boson pair production with full top quark mass dependence*  
 2360 *matched to parton showers*, *JHEP* **08** (2017) 088 [[1703.09252](#)].

## Bibliography

- 2361 [178] M. Cacciari, G. P. Salam and G. Soyez, *The Anti- $k(t)$  jet clustering algorithm*,  
2362 *JHEP* **04** (2008) 063 [[0802.1189](#)].
- 2363 [179] *Les Houches 2017: Physics at TeV Colliders Standard Model Working Group  
2364 Report*, 2018.
- 2365 [180] S. Ferrario Ravasio, T. Jezo, P. Nason and C. Oleari, *A Theoretical Study of  
2366 Top-Mass Measurements at the LHC Using NLO+PS Generators of Increasing  
2367 Accuracy*, [[1801.03944](#)].

# 2368 A Template fit results

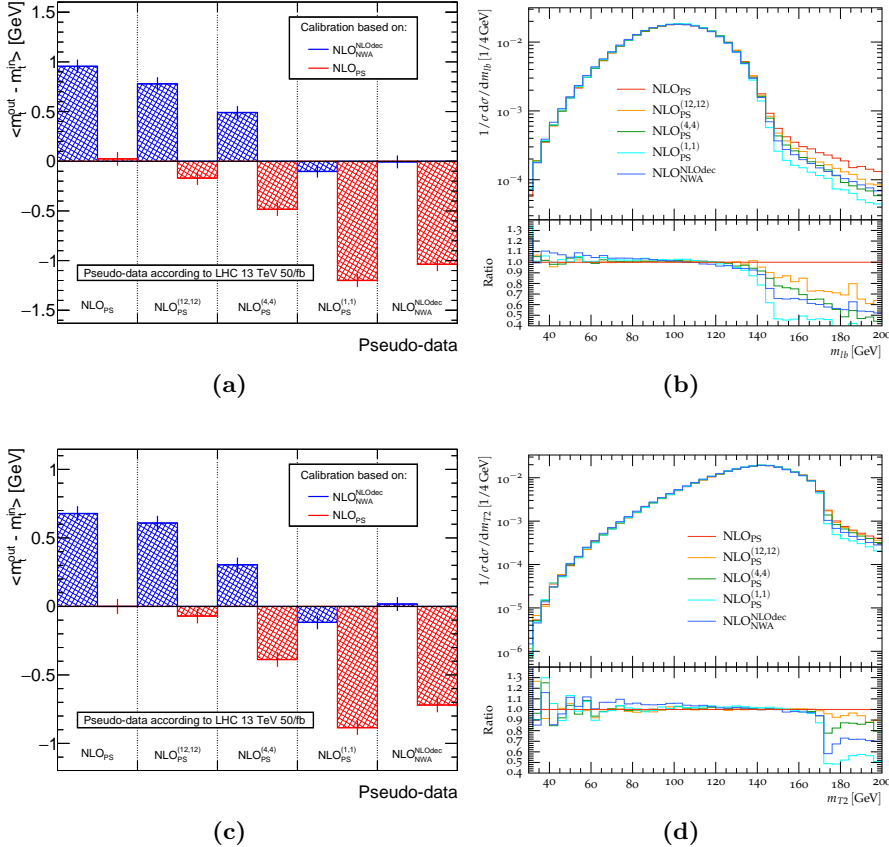
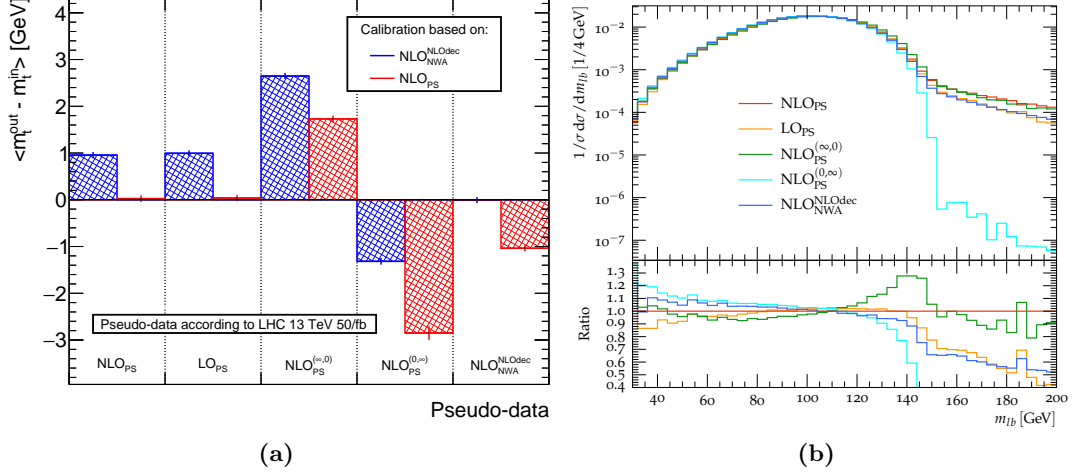


Figure A.1

**Figure A.2:** (a) The mass offsets  $\Delta m_t$  fitted from the  $m_{\ell b}$  distribution are shown for restricted-shower pseudo-data samples  $\text{NLO}_{\text{PS}}^{(n_{\text{max}}^{\text{prod}}, n_{\text{max}}^{\text{dec}})}$ , where the shower is terminated after a certain number of emissions  $n_{\text{max}}$  in the  $t\bar{t}$  production and decay showers. They are compared to the full parton-shower and the  $\text{NLO}_{\text{NWA}}^{\text{NLOdec}}$  pseudo-data prediction. For each of these pseudo-data sets, the bias in  $m_t$  is given as a colored bar (in blue for the  $\text{NLO}_{\text{NWA}}^{\text{NLOdec}}$  calibration function, respectively in red when using the  $\text{NLO}_{\text{PS}}$  calibration). (b) The corresponding normalized  $m_{\ell b}$  distribution is plotted for the mentioned predictions at  $m_t = 172.5$  GeV. (c-d) Same as (a-b) but for  $m_{T2}$ .

## A Template fit results



**Figure A.3:** Same as Fig. A.2, but for the NLO<sub>PS</sub> and LO<sub>PS</sub> cases, as well as for pseudo-data sets generated by predictions where the decay shower, respectively the production shower are entirely deactivated.

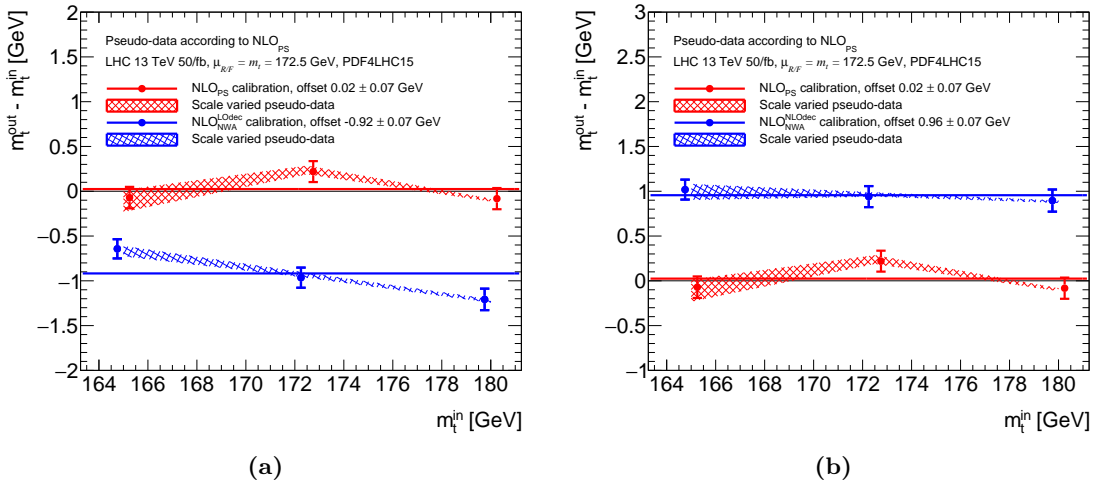


**Figure A.4:** Further band plots from  $m_{\ell b}$  fitted pseudo-data sets.

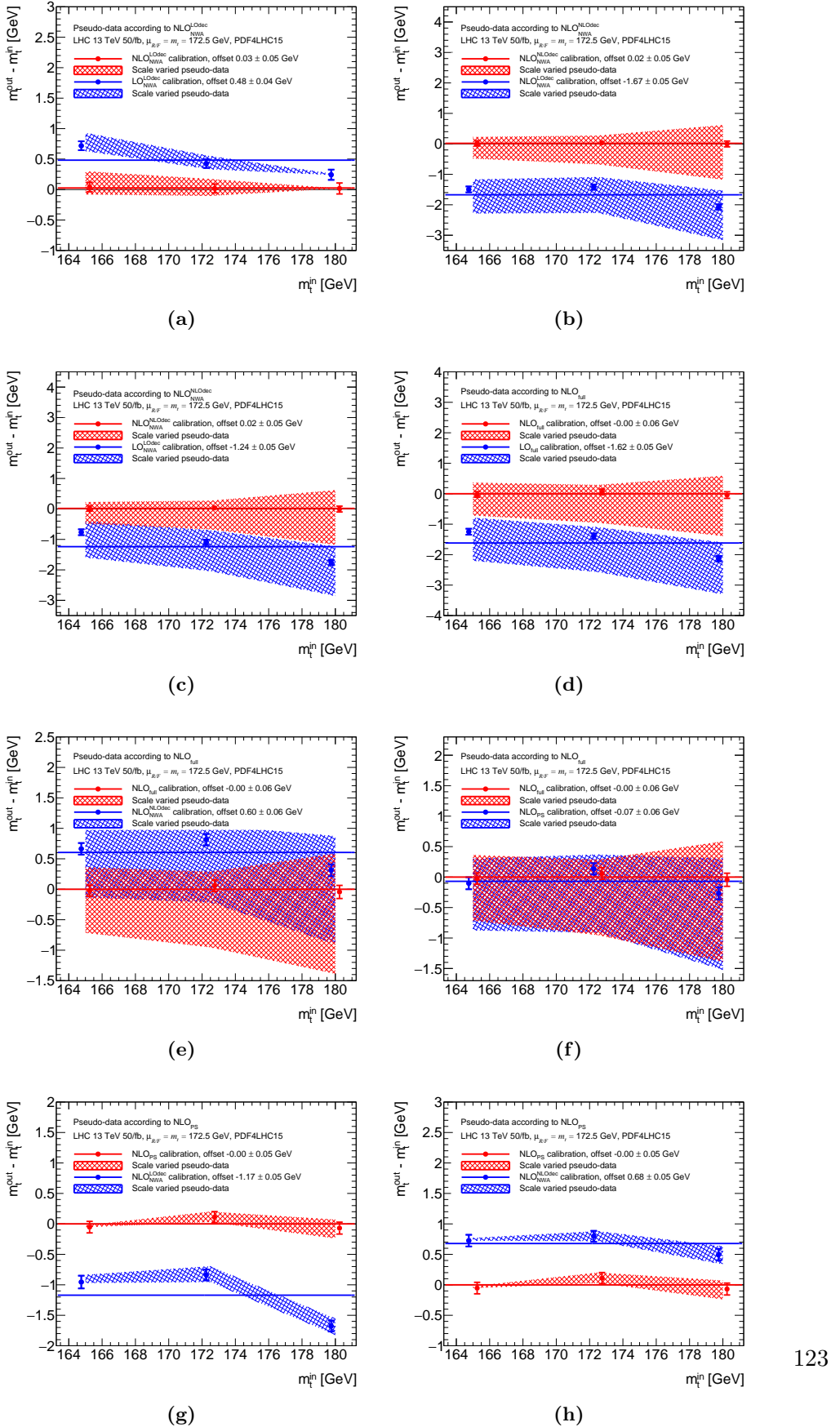


**Figure A.5:** Further band plots from  $m_{T2}$  fitted pseudo-data sets.

## A Template fit results

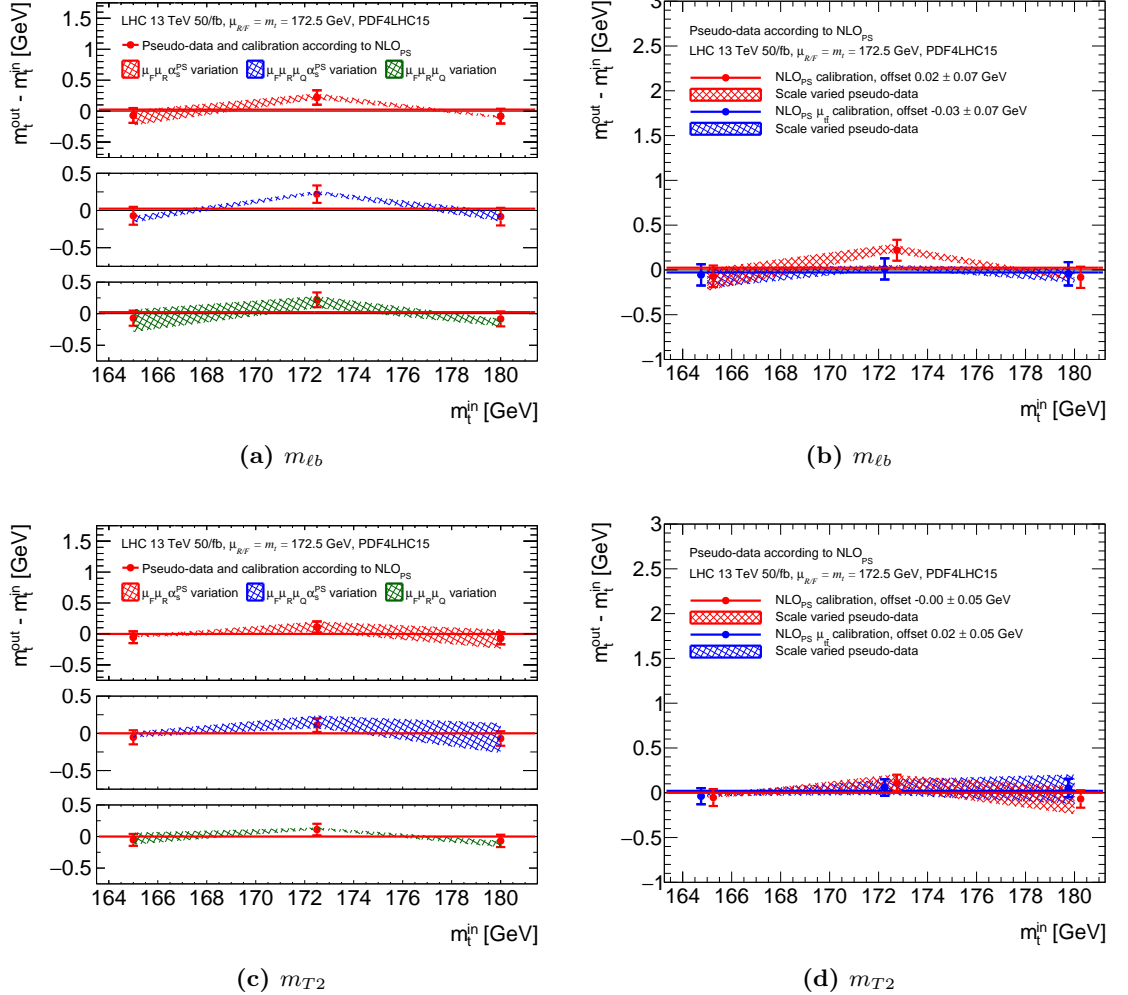


**Figure A.6:** Offsets from NLO<sub>PS</sub> predictions comparing (a) different prescriptions for evaluating the shower scale uncertainties and (b) the two different central scale choices described in the text.

## B Color-flow comparisons for Sherpa

## 2370 C BSM benchmark points in $hh$ production

2371 The coefficients  $A_i$ ,  $i = 1, \dots, 23$  (15) defined for the general expression of the NLO (LO)  
 2372 cross-section as a function of the anomalous Higgs couplings in Eq. (10.16) are shown  
 2373 in Table C.1, at 13 TeV at LHC. To compute these, the cross-section was calculated for  
 2374 different values of the couplings that were replaced in Eq. (10.16), thus giving a system  
 2375 of equations that one can project out to extract the values of the coefficients  $A_i$ .

2376 The LO and NLO coefficients for  $\sqrt{s} = 13, 14$  and  $27$  TeV are available on the ARXIV  
 2377 e-print of Ref. [169], as well as a Mathematica file explaining how to use them. These  
 2378 can also be derived differentially for a fixed bin width. The differential coefficients can  
 2379 also be downloaded for the  $m_{hh}$  distribution, with the binning shown in our histograms.

$A_i$	$A_i^{\text{LO}}$	$\Delta A_i^{\text{LO}}$	$A_i^{\text{NLO}}$	$\Delta A_i^{\text{NLO}}$
$A_1$	2.0806	0.0016	2.2339	0.0101
$A_2$	10.2011	0.0081	12.4598	0.0424
$A_3$	0.2781	0.0019	0.3422	0.0154
$A_4$	0.3140	0.0003	0.3468	0.0033
$A_5$	12.2731	0.0101	13.0087	0.0962
$A_6$	-8.4931	0.0089	-9.6455	0.0504
$A_7$	-1.3587	0.0015	-1.5755	0.0136
$A_8$	2.8025	0.0131	3.4385	0.0772
$A_9$	2.4802	0.0128	2.8669	0.0772
$A_{10}$	14.6908	0.0311	16.6912	0.1785
$A_{11}$	-1.1592	0.0031	-1.2529	0.0291
$A_{12}$	-5.5118	0.0131	-5.8122	0.1340
$A_{13}$	0.5605	0.0034	0.6497	0.0287
$A_{14}$	2.4798	0.0190	2.8593	0.1930
$A_{15}$	2.8943	0.0158	3.1448	0.1487
$A_{16}$			-0.008162	0.000225
$A_{17}$			0.020865	0.000399
$A_{18}$			0.016816	0.000783
$A_{19}$			0.029858	0.000829
$A_{20}$			-0.027025	0.000702
$A_{21}$			0.072692	0.001288
$A_{22}$			0.014523	0.000704
$A_{23}$			0.123291	0.006506

**Table C.1:** The coefficients defined in Eqs. (10.15), (10.16) are determined by computing cross-sections for a subset of parameters, and projecting out equations for the  $A_i$ 's. Statistical uncertainties are propagated from the cross-section level to the coefficient result, without correlations.

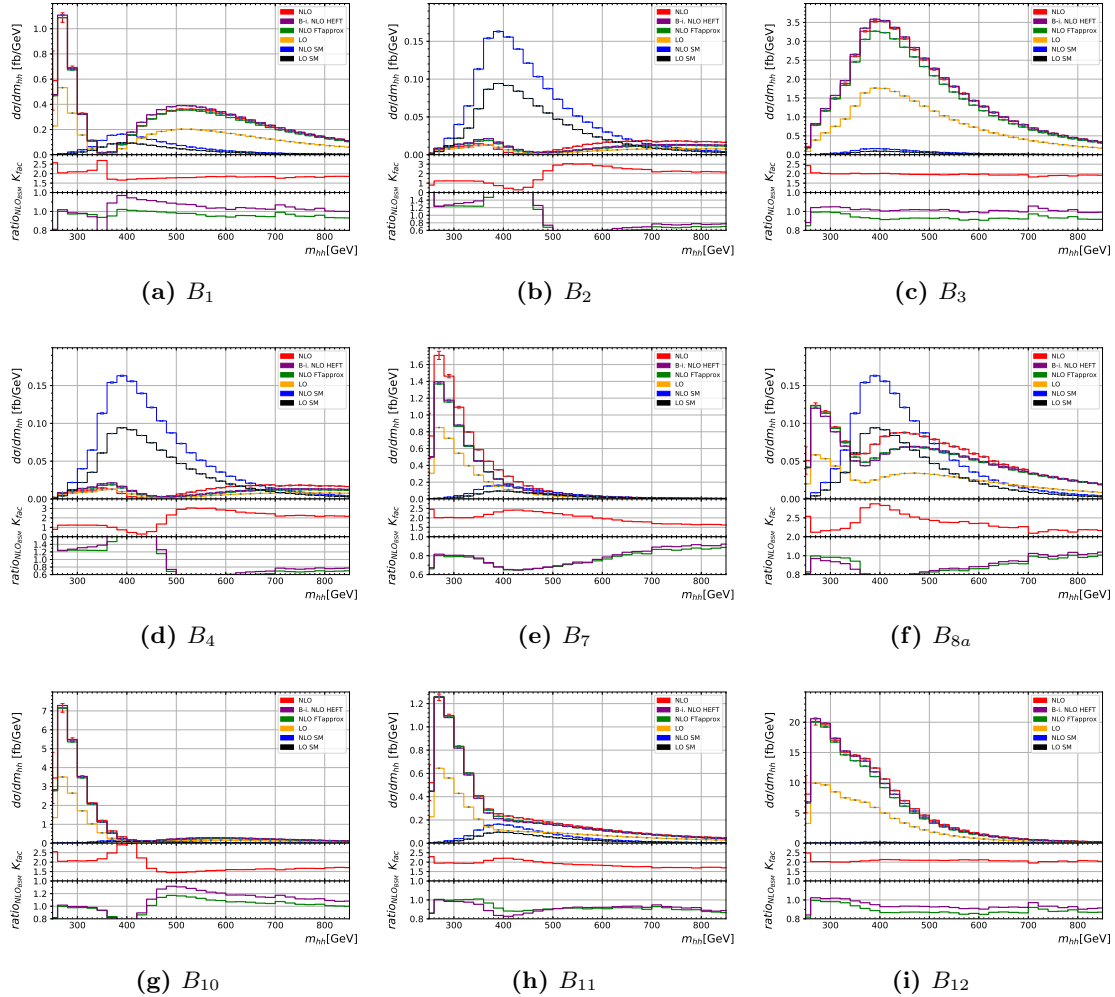


**Figure C.1:** The invariant mass of the Higgs boson pair  $m_{hh}$  is shown for the different benchmark points  $B_i$ ,  $i = 1, \dots, 12$  defined in Table 10.1 and not already shown in Chapter 10.

### C BSM benchmark points in $hh$ production

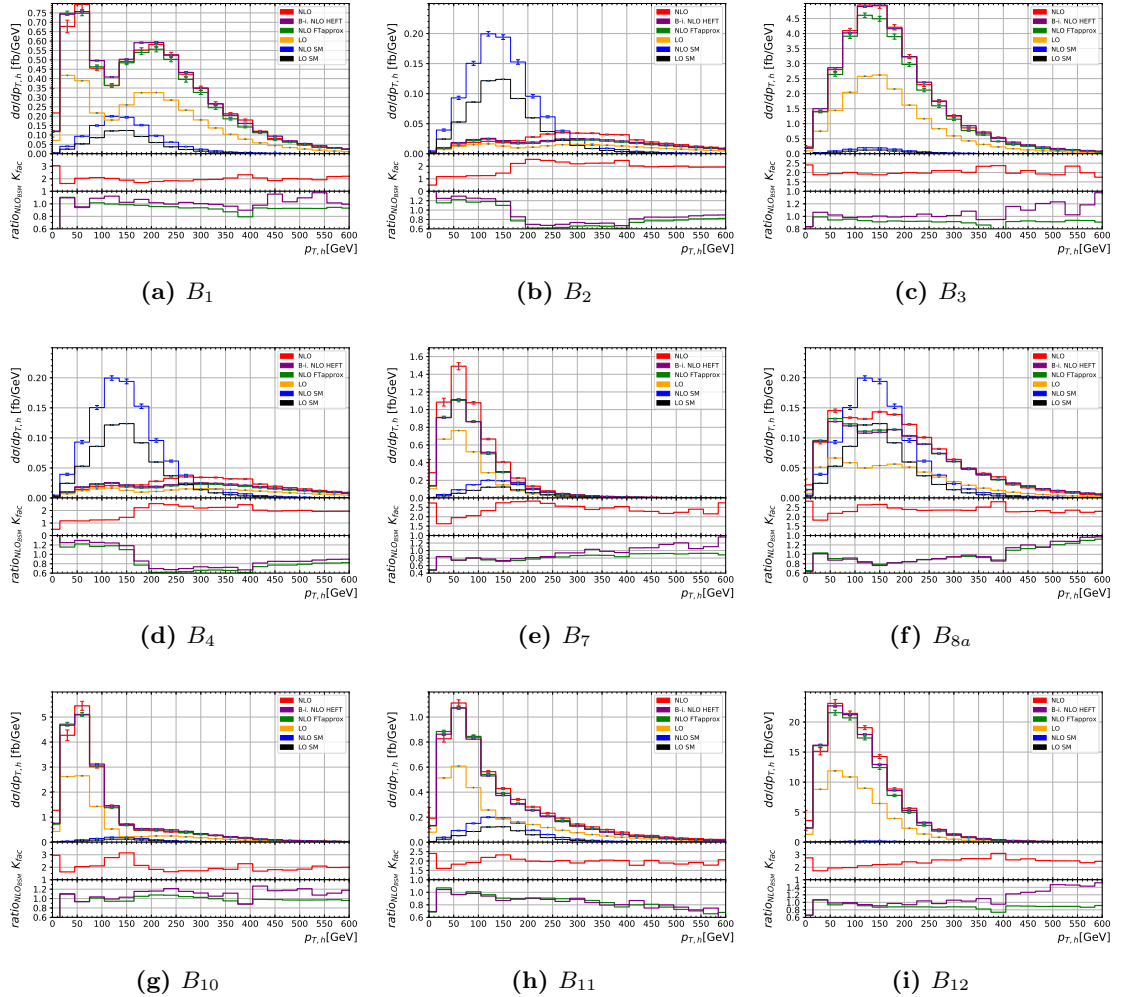


**Figure C.2:** The transverse momentum  $p_{T,h}$  of one (any) Higgs boson is shown for the different benchmark points  $B_i$ ,  $i = 1, \dots, 12$  defined in Table 10.1 and not already shown in Chapter 10.

## 2380 D Hardness definitions in Powheg to 2381 Pythia matching

2382 The technical parameters for matching the **Pythia** 8 parton-shower to LHE files pro-  
2383 duced by **POWHEG** are defined in a file called `main31.cmnd`, which bases on the LHE  
2384 showering example from **Pythia**. There, several definitions for the additional radia-  
2385 tion have to be set in order for the parton-shower to avoid double-counting regions of  
2386 phase-space already covered by **POWHEG**. We set:

- The number of final-state particles in the Born process  $gg \rightarrow hh$ .

2387       **POWHEG:nFinal = 2**

- 2388       • The parton-shower vetoes emissions that have a transverse momentum higher than  
2389       the hardest **POWHEG** emission, and checks the first three. A veto is applied if  
2390       **pTemt > pThard** (see below).

2392       **POWHEG:veto = 1**

2393       **POWHEG:vetoCount = 3**

- 2394       • The **pTemt** and **pThard** scale definition is set: **pTemt** is set to the transverse mo-  
2395       mentum of the radiated particle with respect to the emitting parton, and **pThard** is  
2396       set to the **SCALUP** value read in the LHE event, and set by **POWHEG**. The definition  
2397       of the emitted parton is chosen by **Pythia** for the final-state radiation.

2398       **POWHEG:pTemt = 0**

2399       **POWHEG:pThard = 0**

2400       **POWHEG:emitted = 0**

2401       **POWHEG:pTdef = 1**

2402 The hardness **pTdef** is defined by the transverse momentum  $p_T$  for initial-state  
2403 radiation, and with the distance between radiator and emitted partons  $d_{ij}$  for  
2404 final-state radiation corresponding to the **POWHEG** definition given by:

$$d_{ij} = \frac{m_{ij}^2 E_i E_j}{(E_i + E_j)^2} .$$